## University of Wisconsin Milwaukee
## UWM Digital Commons

August 2017

# Biomedical Applications of Mid-Infrared Spectroscopic Imaging and Multivariate Data Analysis: Contribution to the Understanding of Diabetes Pathogenesis

Ebrahim Aboualizadeh
*University of Wisconsin-Milwaukee*

# BIOMEDICAL APPLICATIONS OF MID-INFRARED SPECTROSCOPIC IMAGING AND MULTIVARIATE DATA ANALYSIS: CONTRIBUTION TO THE UNDERSTANDING OF DIABETES PATHOGENESIS

by

Ebrahim Aboualizadeh

A Dissertation Submitted in

Partial Fulfillment of the

Requirements for the Degree of

Doctor of Philosophy

in Physics

at

The University of Wisconsin-Milwaukee

August 2017

ABSTRACT

BIOMEDICAL APPLICATIONS OF MID-INFRARED SPECTROSCOPIC IMAGING
AND MULTIVARIATE DATA ANALYSIS: CONTRIBUTION TO THE
UNDERSTANDING OF DIABETES PATHOGENESIS


by

Ebrahim Aboualizadeh


The University of Wisconsin-Milwaukee, 2017
Under the Supervision of Professor Carol Hirschmugl


Diabetic retinopathy (DR) is a microvascular complication of diabetes and a leading cause of adult vision loss. Although a great deal of progress has been made in ophthalmological examinations and clinical approaches to detect the signs of retinopathy in patients with diabetes, there still remain outstanding questions regarding the molecular and biochemical changes involved. To discover the biochemical mechanisms underlying the development and progression of changes in the retina as a result of diabetes, a more comprehensive understanding of the bio-molecular processes, in individual retinal cells subjected to hyperglycemia, is required. Animal models provide a suitable resource for temporal detection of the underlying pathophysiological and biochemical changes associated with DR, which is not fully attainable in human studies. In the present study, I aimed to determine the nature of diabetes-induced, highly localized biochemical changes in the retinal tissue from Ins2$^{Akita/+}$ (Akita/+; a model of Type I diabetes) male mice with different duration of diabetes. Employing label-free, spatially resolved Fourier transform infrared (FT-IR) imaging engaged with chemometric tools enabled me to identify temporal-dependent reproducible biomarkers of the diabetic retinal tissue from mice with 6 or 12 weeks, and 6 or 10 months of diabetes. I report, for the first time, the origin of molecular changes

ii

in the biochemistry of individual retinal layers with different duration of diabetes. A robust classification between distinctive retinal layers - namely photoreceptor layer (PRL), outer plexiform layer (OPL), inner nuclear layer (INL), and inner plexiform layer (IPL) - and associated temporal-dependent spectral biomarkers, were delineated. Spatially-resolved super resolution chemical images revealed oxidative stress-induced structural and morphological alterations within the nucleus of the photoreceptors. Comparison among the PRL, OPL, INL, and IPL suggested that the photoreceptor layer is the most susceptible layer to the oxidative stress with short-duration of diabetes. Moreover, for the first time, we present the temporal-dependent molecular alterations for the PRL, OPL, INL, and IPL from Akita/+ mice, with progression of diabetes. These findings are potentially important and may be of particular benefit in understanding the molecular and biological activity of retinal cells during oxidative stress in diabetes. Our integrating paradigm provides a new conceptual framework and a significant rationale for a better understanding of the molecular and cellular mechanisms underlying the development and progression of DR. This approach may yield alternative and potentially complimentary methods for the assessment of diabetes changes. It is expected that the conclusions drawn from this work will bridge the gap in our knowledge regarding the biochemical mechanisms of the DR and address some critical needs in the biomedical community.

*To my father, who values education above all*

*and*

*To my mother, who taught me unconditional love*

# TABLE OF CONTENTS

# LIST OF FIGURES

# LIST OF TABLES

# ACKNOWLEDGMENTS

First and foremost, I would like to express my sincere appreciation to my advisor Prof. Carol Hirschmugl, for her unwavering and unending support throughout my graduate studies. Her guidance, thoughts, ideas, patience, and encouragement have been integral to both my professional and personal development. She has given me the opportunity to explore scientific problems and develop my own individual way of thinking. I am so grateful to her for teaching me the communication and collaboration skills by being a great example. Her enthusiasm in learning new scientific methods from a broad range of scientists, and the ability to convey novel ideas is something that I hope to emulate during my academic career. She has been my eyes when I could not see and my best friend during my PhD studies.

I would like to thank my committee member Prof. Nader Sheibani whose deep understanding of biological systems and his extensive experience in the field of ophthalmology have been an inspiration to me for the past five years of graduate school. I greatly benefited from his keen scientific insight, and without his efforts my thesis would have undoubtedly been more challenging. I appreciate the time he has spent in working with me and providing valuable feedback. I am so thankful to Dr. Christine Sorenson in the department of pediatrics at the University of Wisconsin-Madison for preparing animals and harvesting eyes from rodents for my studies. She generously provided me with samples and I sincerely appreciate her hard work.

I would also like to thank my committee members Professor Valerica Raicu, Dr. Mahsa Ranji, and Dr. Peter Schwander for their interest in my work, valuable feedback and advice. Their probing questions as PhD committee members were useful in consolidating my ideas. The Physics department has been wonderful to me over the past five years and I am glad to be a part

of it. I would like to especially thank Stephen Kennedy, Reba Sinha, Greg Baran, and Kathryn Valerius for their unconditional support. The students, postdocs, and faculty in the Physics department have been very kind to me and I would like to thank them all.

Special thanks to the members of my research group, Miriam Unger, Eric Mattson, Alex Schofield, Nicholas Walter, and the technical staff and members of the synchrotron radiation center (SRC). They stood by me and it was fantastic to have the opportunity to learn from them and listen to their ideas. I would like to thank my friends, Masoud, Omid, Ali, Samaneh, Farid, Mehdi, Megan, Ghoncheh, Peng, Nazanin, Asher, Reyhaneh, Russel, Aruna, Binod, Mike, Ahmad, and Prakash.

Finally, I would like to acknowledge my family who supported me during my time here. My wife Kirsten with her understanding, love, and support made this dissertation possible. She is my best friend, made my life better in so many ways, and stood by me through my graduate studies. Farzaneh, Amin, and Mohsen, my wonderful sister and brothers, who have been there for me every step of the way in the challenging graduate student life. They have been my close friends all my life and their advice and support have been greatly reassuring. I am thankful to my family members, Kirk, Cynthia, and Mark Midtbo, Lindsay and Mark Pronley for their supports. Most importantly, my parents, Sedigheh and Faramarz, receive my deepest gratitude for all the moral support and love for their dedication and the many years of support during my life. Without their support I would never have enjoyed so many opportunities.

**Chapter 1: Introduction**

**1.1. Introduction**

Fourier Transform Infrared (FTIR) spectroscopic widefield imaging provides specific spatially resolved information about the chemistry of materials. Chemical signatures of DNA, carbohydrates (i.e. glucose), proteins, and lipids are recorded as a function of position. Frequencies of IR light match frequency dependent vibrations of functional groups (based on the masses of the participating atoms) and are absorbed. A range of important chemical signatures associated with the biomarkers of disease progression has been detected in biological materials. Despite the dramatic development in diagnostic procedures and treatment of diseases, identifying biomarkers with temporal and spatial resolution at the cellular and molecular level is critical for early detection and a better understanding of the disease pathology. FT-IR spectroscopy has been applied to understand the biomolecular alteration in the variety of tissues including breast, prostate, skin, lung, brain, kidney, and colon as well as single cells and neurons. In this dissertation, I demonstrate the effectiveness of FTIR imaging in detecting the biomarkers of diabetic retinopathy at different stages of the disease. The central theme of this study is focused on spectroscopic imaging of retinal tissues and developing multivariate algorithms, which provide information regarding the molecular mechanism of diabetes that help pathologists for a better understanding of the diabetes histology. In this study, I aimed to determine a more detailed understanding of the natural history of diabetic retinopathy in Akita/+ (type 1 diabetes model) male mice with different duration of diabetes.

**1.2. Organization of the Dissertation**

The dissertation is organized as follows. In chapter 2, I present an overview of FTIR spectroscopy and widefield spectroscopic imaging. The history of FTIR instruments, recent

developments in detectors and sources, *in situ* IR spectromicroscopy of live cells, microscope optics, and the experimental techniques and details of the measurements used in this study are discussed. I also present the development of synchrotron infrared spectromicroscopy and applications in this chapter.

In chapter 3, a general framework of multivariate data analysis and a review of existing chemometric tools for clustering and classification of tissues and cells have been discussed. Pre-processing methods for data evaluations, unsupervised classification methods like principal component analysis (PCA), hierarchical clustering analysis (HCA), and k-means clustering, as well as supervised clustering methods including linear discriminant analysis (LDA), artificial neural network, and naïve Bayesian classifiers are detailed. The framework of a multivariate analysis termed PCA-LDA (i.e. principal component analysis followed by linear discriminant analysis) to identify the discriminatory features in each classification is explained. The series of examples for classification of tissues and cells are illustrated in this chapter. In this chapter, spectral distortions and artefacts in the mid-infrared spectrum, caused by sample geometry and the theory behind resonant Mie scattering are discussed. Interpretation of mid-IR spectra, especially when there is a complex sample is critical and spectral artefacts can lead to misunderstanding of the chemistry of samples due to the shifts in peak positions. I also demonstrate some examples from tissues and cells that show how correcting spectral distortions mitigate the data interpretation and a better understanding of chemical characteristics.

In chapter 4, I demonstrate the retinal anatomy and physiology and discuss the associated chemistry of the retinal layers and general framework of the light propagation into the retina. Basics of diabetic retinopathy; symptoms, causes and risk factors, and the complications during

diabetes at each stage of the disease are reviewed. Existing diagnostic modalities in treating diabetic retinopathy with their limitations are discussed.

Chapter 5 discusses the oxidative stress detected in short-term (6-week-old) diabetes in rodents determined by synchrotron-based FTIR imaging. FTIR widefield microscopy coupled with multivariate data analysis was employed to identify biomarkers with spatial resolution at the cellular and molecular level. In this chapter, I demonstrate the biomarkers of oxidative stress and lipid peroxidation at the early stages of diabetes and oxidative-stress induced alterations in the diabetic retina tissue morphology compared to the control retina. Distinctive layers of the retina, namely the photoreceptor retinal layer (PRL), the outer plexiform layer (OPL), the inner nuclear layer (INL) and the inner plexiform layer (IPL), are evaluated and the contribution of the photoreceptor layer to the oxidative stress in short-term diabetes is discussed.

Chapter 6 discusses temporal-dependent diabetes-induced biochemical alteration in the retinal tissue at different duration of diabetes in rodent models. Spatially resolved chemical images allow me to understand diabetes-induced alterations in biochemistry of distinct retinal layers. I demonstrate the alterations in the chemical images from both Akita/+ (diabetic) and non-diabetic retinal tissues, and the spectral biomarkers from the comparison of distinct retinal layers from diabetic and non-diabetic mice. Moreover, I present the molecular factors associated with the changes to the protein structure and cellular lipids of retinal layers induced by different duration of diabetes. My paradigm provides a new conceptual framework for a better understanding of the temporal cellular and biochemical changes underlying the progression of diabetic retinopathy. It is expected that our integrating paradigm provide a new conceptual framework for a better understanding of the mechanism underlying diabetic retinopathy. In this work, I demonstrate that high-resolution infrared spectrochemical imaging with multivariate

image analysis is a robust approach to differentiate between diabetic and non-diabetic tissues with the highest level of classification. Chapter 7 discusses the concluding remarks of this dissertation.

## Chapter 2: Fourier transform infrared (FTIR) spectroscopic imaging

### 2.1. Introduction

Fourier transform infrared (FTIR) spectroscopic imaging is a label-free and non-destructive imaging technique that detects the distribution of biologically relevant components in samples, concurrently revealing biochemical composition and morphology [1]. The goal of absorption spectroscopy is to determine how much light is absorbed by the sample. Absorption spectrum of a molecule provides structural insights about the functional groups that constitute the molecule. Since molecules have different chemical structures, each molecule produces unique spectral fingerprint that can be used in interpretation of the spectra of complex mixtures. Thanks to advances in focal plane array detectors [2], the field of IR spectromicroscopy, which is a combination of spectroscopy and microscopy, generated significant improvement in scientific study and applications in this field. FTIR imaging allows illuminating and measuring larger areas of samples, and detects heterogeneities in tissues, which provides thousands of spectra simultaneously in a few minutes. Nowadays, FTIR imaging has a wide range of applications in animal tissues [3,4], plant studies [5,6] restoring arts [7], cancer histopathology [8-12], neuroscience [13,14], polymers [15], and drug delivery [16,17]. The fundamentals of instruments, theory and background, and coupling of synchrotron radiation to FTIR microscope are discussed in this chapter.

### 2.2. Interferogram

In the prior infrared dispersive spectroscopy method, a monochrometer was used to separate the wavelengths in the source and a particular wavelength was passed through a sample and then the absorption spectrum was recorded [18]. The procedure was then repeated for every single frequency to achieve the full absorption spectrum for the sample. In this method, a grating was

placed before the sample and was used to select the frequencies of light. During 1950's, time domain spectrometers [19] were developed to collect IR spectra and still considered in widespread use as infrared spectrometers. IR spectrometers are designed based on typical Michelson interferometer, which split the beam through beam splitter [19]. Radiation from infrared source is passed through a beam splitter (identical beam splitter divides the beam into two equal beams), which one beam travels to the fixed mirror and the other to the moving mirror. The reflected beams from the fixed and moving mirrors are recombined and passed through the sample and finally to the detector. The schematic of the Michelson interferometer is shown in Figure 2.1. In FTIR spectrometers all the wavenumbers are impinged simultaneously to the sample, where in the dispersive spectrometers one observes wavenumbers sequentially. This is called Felleget (multiplex) advantage. The optical path difference (OPD) between the beams that travel to the fixed mirror and the moving mirror back to the beam splitter is called retardation ($\delta$). When the both distances of moving mirror and fixed mirror from the beam splitter are equal, this point is called zero path difference (ZPD) and the interference between the beams is constructive at ZPD. The intensity of the source recorded at the detector is called interferogram and written as a function of $\delta$ by:

$$I(\delta) = 0.5\, I(\nu_0)(1 + \cos 2\, \pi \nu_0 \delta)$$

Where $\nu_0$ is the wavenumber of radiation [19]. The first term is called DC term and there is no contribution from the DC term in spectrometry. Therefore the intensity can be written as:

$$I(\delta) = 0.5\, I(\nu_0) \cos 2\, \pi \nu_0 \delta$$

6
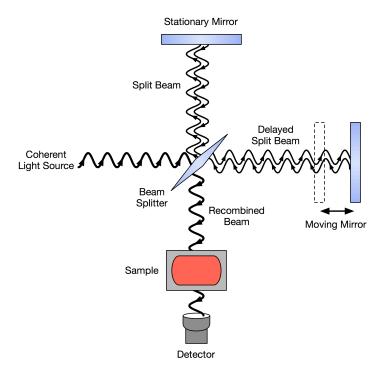
**Figure 2.1:** Schematic of a Michelson interferometer. Photo courtesy by Petergans [Public domain]. Reprinted from Wikimedia Commons.

In practice, there are several factors that affect the intensity recorded at the detector including beamsplitter efficacy, detector response, and amplifier characteristics. Thus, the constant $I(\nu_0)$ should be modified to $B(\nu_0)$ and the new parameter entails instrumental characteristics. The new equation that describes the interferogram is:

$$S(\delta) = B(\nu_0) \cos 2\pi\nu_0\delta$$

The second advantage of FTIR spectrometers to dispersive spectrometers is the Fast Fourier Transform (FFT) algorithm that is discovered by J.W. Cooley and J.W. Tukey in 1965 [20]. The conversion of interferogram in time domain into the spectra in frequency domain was now

possible. The interferogram is sampled using an analog to digital converter and then loaded into the computer to perform FFT and generate the spectrum as a function of frequency. Greater signal to noise ratio, speed in data acquisition, and a better resolving power for the instrument are some advantages of Fourier transform spectroscopy. The interferogram and the spectrum can be calculated from one another via Fourier cosine transform as shown below.

$$S(\delta) = \int_{-\infty}^{+\infty} B(\nu_0) \cos(2\pi\nu_0\delta)d\nu_0$$

$$B(\nu_0) = \int_{-\infty}^{+\infty} S(\delta) \cos(2\pi\nu_0\delta)d\delta$$

### 2.3. Spectral Resolution

Spectral resolution in a spectrometer is the ability to resolve two wavenumbers $\nu_1$ and $\nu_2$ that are closely spaced. The resolution of a spectrometer is limited by the maximum optical path difference between the beams that travel from the arms of interferometer. Thus, the minimum difference between two adjacent wavenumbers ($\Delta\nu = \nu_1 - \nu_2$) equals the maximum optical path difference in the interference pattern and has to be such that

$$\Delta\nu = \Delta x_{max}^{-1}$$

Therefore, the narrower the separation between two wavenumbers, the greater is the retardation. Lower or higher spectral resolution highly depends on the sample and the information I am seeking in the sample. For example, biological specimen requires higher spectral resolution due to the subtle spectral features (small peaks and shoulders) in the spectrum, although it takes longer time to scan at higher resolutions. Typical spectral resolutions for routine IR

8

measurements are 4 or 8 cm$^{-1}$. Mathematically speaking, to limit the maximum retardation of the interferogram to $\Delta$ centimeters, one can multiply the interferogram by a $D(\delta)$ function, which is unity between $-\Delta$ and $+\Delta$, and zero elsewhere. The $D(\delta)$ is a boxcar function and therefore the spectrum can be written as:

$$B(v) = \int_{-\infty}^{+\infty} S(\delta)\, D(\delta)\cos(2\,\pi v\delta)d\delta$$

Which is a convolution of the original spectrum and the Fourier transform of the boxcar function. Since the Fourier transform of a boxcar function is a *sinc* function, it creates side lobes (small oscillations from the center of a line shape) that possess negative values. These negative values will be eliminated in the calculated spectrum and therefore, to prevent losing information, apodization is used to control the effects of finite retardation and suppress the magnitude of these oscillations.

### 2.4. Signal to noise ratio

Signal to noise ratio (SNR) is one of the critical factors in data acquisition that largely affects the quality of the spectrum. SNR is proportional to the root square of the time as follows:

$$SNR \propto n^{1/2}$$

Since the noise component is uncorrelated to the source, signal averaging can increase the SNR in the acquired spectrum. The signal power increases by the factor of $N^2$, while the noise power goes up by the factor of $N$, therefore, signal averaging increases the SNR by the factor of $N$. Consider the signal x is constant for all observations z., then the n$^{th}$ observation is written as:

9

$$z_n = x + r_n$$

Where $r_n$ is the noise that changes for every observation. The SNR of $z_n$ is defined as:

$$\beta 1 = \frac{E(x^2)}{E(r_n^2)}$$

Where E is the expectation operator. If we average N observations of $z_n$, we get:

$$\hat{z} = \frac{1}{N}\sum\nolimits_{n=1}^{N}(x + r_n) = x + \frac{1}{N}\sum_{n=1}^{N}r_n$$

Now we calculate the SNR for the averaged observation $\hat{z}$:

$$\beta_2 = \frac{E(x^2)}{\frac{1}{N^2}E\left[\sum_{n=1}^{N}r_n^2\right]}$$

Since the noise component is uncorrelated to the source, we can simplify the expression in the denominator into:

$$E\left[\sum_{n=1}^{N}r_n\right]^2 = \sum_{n=1}^{N}E[r_n^2] = NE[r_n^2]$$

Inserting into the expression for $\beta_2$ yields:

$$\beta_2 = N\frac{E(x^2)}{E[r_n^2]}$$

Now, comparing the SNR $\beta_1$ for single observation and $\beta_2$ for averaged observation reveals that averaging increases the SNR by a factor of N. To repeat reproducible scans, there is an

embedded monochromatic laser source in the interferometer that creates its own interferogram at a separate detector and monitors the displacement of the moving mirror (OPD).

### 2.5. Detectors

There are three types of detectors that are routinely used in FTIR spectroscopy. The choice of detector depends on various experimental factors including spectral resolution, optical throughput of the IR beam, sampling geometry, and spectral range desired of the experiment. For static measurement (e.g. standard measurement of pure chemicals) deuterated triglycine sulfate (DTGS) detectors are suitable choice due to the high throughput (more than 20% of IR beam reaches the detector). The second type of detector is a mercury cadmium telluride (MCT) detector, which is a photoconductive detector. When an infrared photon has sufficient energy to move an electron from the valence band to the conduction band, the detection occurs. MCT detectors are $LN_2$ cooled detectors and is opaque to the infrared photons that have less energy than the energy gap. One of the limitations of MCT detectors is losing the responsivity and directivity at high throughput; therefore, one must limits the intensity of IR beam reaching the detector at high energies.
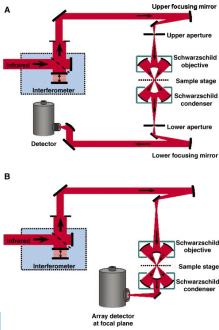
**Figure 2.2**: Schematic illustration of the beampath in (A) aperture-based FTIR single point spectroscopy and (B) FTIR imaging using focal point array detector. In both methods, the microscope and the detector are attached to the Michelson interferometer. Reprinted with permission from [21].

The third detector that is commonly used for FTIR chemical imaging is a multi-channel focal plane array (FPA) detector [22]. FPA operates in the spectral range 5400-850 cm$^{-1}$ and the pixel size at the detector (each element of the detector) is about $40 \times 40$ μm$^2$. FPA allows concurrent acquisition of n × n number of spatially resolved spectra (n=16, 32, 64 or 128) where each pixel represents and infrared spectrum. FPA has advantages over MCT detectors including larger field of view, more chemical information, speed in data acquisition, greater number of spectra per measurement (4096 spectra per measurement for 64×64 FPA size), and detection of morphology and heterogeneities of the specimen. Schematic diagram of the beam path in FT-IR single point spectroscopy and FT-IR widefield imaging with a multi-element focal plane array detector is shown in Figure 2.2 [21].

## 2.6. Infrared spectroscopy

Electromagnetic radiation, including IR light, drives the motion of electric charges in matter. If the natural time scale of any oscillations of the charges in a molecule is close to the period of the electromagnetic radiation shining on the system, a condition known as resonance occurs. Near resonance, IR light is efficiently absorbed by the system, allowing the identification of the frequencies of low-energy (1–500 meV) excitations found in the sample. These excitations may involve nuclear motion, such as vibrating molecules, ions, or radicals. For IR spectroscopy, the process of interest is absorption. IR photons are absorbed by vibrations that induce dynamic dipoles originated from oscillations in the density of electrons or electron charge due to atomic motion (the electrons follow the motion of the nuclei). The natural oscillating frequencies of

molecules are related to the masses of the displaced atoms and the strength of their respective chemical bonds. Thus, a "fingerprint" or series of absorption bands with specific vibrations associated with the functional groups for a specific macromolecule are identified, and an absorption spectrum is a plot that shows how well different frequencies of light couple to excitations for the macromolecule. An absorption spectrum (Figure 2.3) is commonly plotted as Absorbance (A) vs. frequency (v), which is related to the transmittance by A = −log T [It is conventional to convert the units for frequency v from Hz ($s^{-1}$) to wavenumbers ($cm^{-1}$) by dividing v by the speed of light c]. Absorbance curves exhibit peaks at energies where the sample has absorbed energy from the incident beam. Functional groups within molecules absorb IR light when they are in resonance with the incident radiation and lead to peaks in the absorption spectrum. The frequencies are dependent on the masses of the atomic constituents and the bonding strength and can therefore be used to identify the functional groups. The absorption strength can also be correlated with the concentration of the functional groups and ideally increases linearly for a wide range of concentrations. An example of a typical absorption spectrum from a biological specimen is demonstrated in Figure 2.3.



13
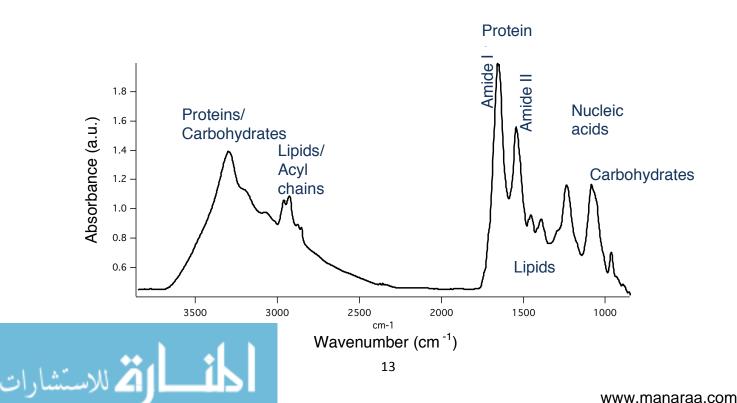
**Figure 2.3:** Schematic illustration of an absorption mid-infrared spectrum of a typical biological sample. The spectrum highlights the functional groups attributed to important macromolecules.

Obtaining concentrations from two-dimensional projection measurements relies upon having a controlled sample thickness or a precise knowledge of the sample thickness at the point being measured since absorption depends on both concentration and path length. Furthermore, for such parameters to be extracted, the sample must be of uniform thickness over the dimension sampled by a given measurement (e.g., 10 μm for a $10 \times 10$ μm$^2$ aperture size). Obtaining relative concentrations for a given sample or sampling area is reliable if the dynamic dipole strengths of a particular mode are known.

Infrared (IR) spectroscopy is a non-destructive and label-free tool for examining live cells [23,24] and allows one to identify the chemical species present within the sample under investigation. IR light detects distinct chemistry based on absorption "fingerprints" providing inherent contrast, without disturbing the sample even under adverse conditions, conferring access to vital, in vivo information. IR spectroscopy is a mature field, yet, more recent schemes coupling it with microscopy, implemented as raster scanning and widefield microspectroscopy measurement schemes provide chemically and spatially resolved 2D projections images of samples. These methods are poised to make significant contributions to the newer directions embraced by scientists in live cell imaging. Many of these state-of-the-art experiments have been facilitated by IR radiation extracted from storage rings or synchrotrons [25,26].

IR spectroscopy allows the determination of the energy of the excitations it probes, and thereby sheds light on the microscopic origin of the excitation. For example, identifying what functional groups exist within cells—based on their known vibrational excitations—can provide

14

insight into how fixation and arsenic induce changes in biomolecules, or to assess native cellular heterogeneity at the chemical level. Recent advances in instrumentation, including the design of spectrometers and detectors and the development of new sources provide the means to enhance significantly the capabilities of this mature field. As a practical matter, IR spectroscopy has found its widest application in identifying the chemical compounds present in an unknown sample by the virtue of frequencies of IR light the sample absorbs. Since the resonance condition occurs over a narrow range of frequencies, which differs for different compounds (i.e., lipid versus carbohydrate functional groups), the exact frequency of the absorbed light provides a characteristic signature of the molecules, ions, or radicals present in the sample. The analytical capabilities of IR spectroscopy are invaluable for identifying chemical composition within complex, often heterogeneous biological systems.

## 2.7. Infrared spectromicroscopy

IR spectromicroscopy, which is a combination of mid-IR spectroscopy and microscopy, is relatively a new term with the development of focal plane array detectors. It is a non-destructive spectrally-resolved modality for imaging biological tissues and allows to collect spectra from different regions of tissue concurrently. Every pixel within the field of view (FOV) entails a mid-IR spectrum and all the frequencies are retained by the phase modulation of the interferometer. IR spectromicroscopy has a wide range of applications from materials and polymers to biological cells and connective tissues at micrometer scale. The objectives that are used in conventional IR spectromicroscopy are Cassegrain or Schwarzschild-like objectives [27] as shown in Figure 2.4. The IR microscope is performing using a bottom Schwarzschild objective (aperture objective) to focus the IR beam to the sample and the upper objective collects the light and relays it on the detector. Schwarzschild objectives consist of a primary concave mirror with a center hole and a

15

secondary convex mirror. The primary concave mirror collects the incoming light through the hole and transmits the light to the secondary mirror. The light reflects and diverges from the secondary convex mirror to fill the concave mirror and the primary mirror then focus the beam to the focal point. The Schwarzschild objectives have zero spherical and chromatic aberrations. Infrared microscopes can perform in two ways depending on whether point illumination or widefield imaging is desired. For point illumination, single element detectors are used and two apertures before and after the sample are embedded to control the throughput of the IR beam impinging on the specimen. This configuration performs in confocal geometry and the apertures allow the illumination of the particular region of the sample area.
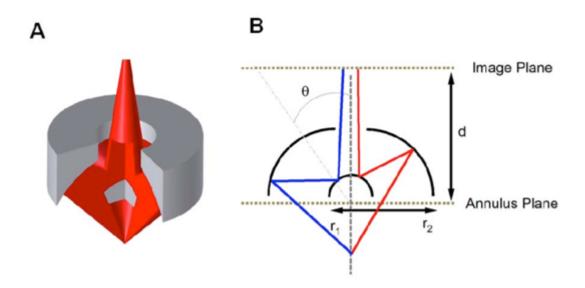


**Figure 2.4:** Illustration of the Schwarzschild optical arrangement. Two parabolic mirrors with radii $r_1$ and $r_2$ are arranged in the objective. The smaller mirror masks the opening of the primary mirror, forming an annular aperture toward the incoming light. "Reprinted with permission from [12]. Copyright (2012) American Chemical Society."

16

On the contrary, for FTIR imaging, the design is apertureless to allow the maximum illumination and widefield imaging within the FOV. There are still two objectives before and after the sample plane, where the bottom one focuses the illumination on the sample plane and the top objective collects the light and transmits to the detector. The beam paths for IR spectroscopy and IR widefield imaging are demonstrated in Figure 2.2. The spatial resolution of the infrared imaging setup is limited by the diffraction of light and depends on the wavelength of the infrared beam and the numerical aperture of the microscope optics.

## 2.8. Hyperspectral Imaging

Hyperspectral imaging or spectroscopic imaging is a combination of vibrational spectroscopy and chemical imaging. The hyperspectral image contains both spatial and spectral information about the sample. In this imaging technique, the sample is partitioned into small pixels and each pixel contains a mid-IR absorption spectrum. The hyperspectral images are plotted as a 3D cube of data (x, y, z), where x and y represent spatial dimensions of the pixel and the z-axis is the absorption of that particular pixel as a function of wavenumber. For example, for the FPA size of 64 × 64, every image contains 4096 mid-IR spectra for a single measurement. Concentration weights of image constituents are different from pixel to pixel and it depends on the pixel composition. However, pure spectra of the constituents from the whole image are identical. By means of bilinear model in multivariate image analysis, one can decompose a raw data into two matrices where the first matrix is associated with the pixel concentrations and the second matrix is attributed to the pure spectra. It is identical to the Beer-Lambert law in matrix form:

$$D = C \, S^T + E$$

Where D is the raw 3D cube of data, C is the concentration values of image constituents within each pixel, $S^T$ contains the pure spectra of image constituents and E is the experimental error. The structure of data is shown in Figure 2.5. It means that every row in matrix C is associated with the concentration weights and provides us information about the chemical composition of that pixel. The concentration variation from pixel to pixel is achievable by taking every column in matrix C. Then by re-dimensioning a column in matrix C into a 2D image, the distribution map of each image constituent can be obtained and it provides valuable spatial information. Taking advantage of this idea and using the analogy between chemometric tools and beer-lambert law in matrix form, the original two-dimensional chemical images and refolded principal component score images can be correlated.
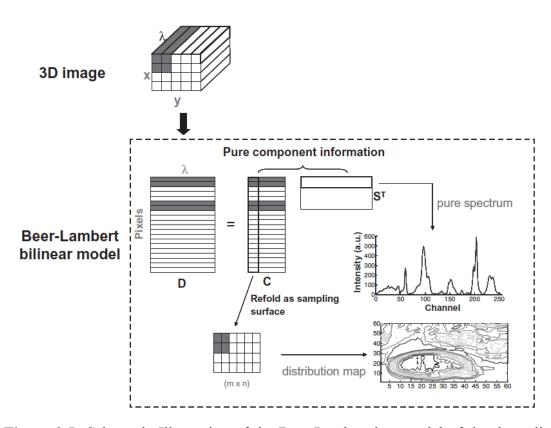
**Figure 2.5:** Schematic Illustration of the Beer-Lambert law model of the three-dimensional hyperspectral images. Reprinted with permission from [29].

## 2.9. Synchrotron FTIR widefield imaging

IR spectromicroscopy has recently evolved by several technological advances; first, coupling IR microscopes with synchrotron source [30] rather than the conventional thermal IR source yields higher signal-to-noise ratio (SNR) than that of the thermal source when using smaller apertures (in confocal experiments) and therefore higher spatial resolution. The tradeoff of this approach is that diffraction-limited imaging at the shortest wavelengths requires a small aperture that reduces the signal for the entire bandwidth, pushing the signal for the longest wavelengths below the detection limit. If a larger aperture is used, spatial resolution for the shorter wavelengths is degraded. Further, the confocal setup has the drawback that image acquisition time ranges from several hours to days, precluding time-resolved measurements such as biochemical kinetics of living cells. The second advance was to replace the single-element detector with a FPA detector (illuminated by a globar) to accelerate data acquisition. Some groups had efforts to illuminate FPA detectors with synchrotron IR beams [27,31]. They succeeded in illuminating a small portion of the FPA to obtain higher SNR in the illuminated area; however, these small illumination areas meant that only a small subset of the FPA corresponding to a relatively small sample area could be used.

Infrared Environmental Imaging (IRENI) beamline, located at the Synchrotron Radiation Center in Madison, WI, USA [28] is the first IR widefield imaging system that has been specifically designed and optimized to overcome the SNR-acquisition time-spatial resolution tradeoff by coupling multiple synchrotron beams with a large field of view FPA detector. The schematic of the IRENI beamline is shown in Figure 2.6.

This capability enabled spectrochemical imaging for challenging problems such biological and medical applications that require many samplings to collect statistically relevant data and/or

www.manaraa.com

high throughput, and analysis of heterogeneous materials at the micrometer scale. In particular, IR imaging of cells *in vivo* is a rapid, nondestructive tool to identify the chemical composition of biological samples for a wide range of physiological and biochemical applications, now realizable with IRENI [32-40].
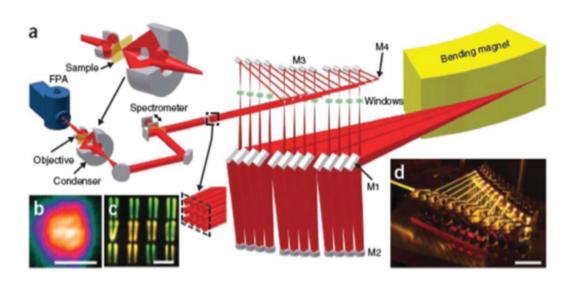


**Figure 2.6:** schematic of the IRENI beamline. a) Organization of the optics highlighting four sets of mirrors focusing the beam from the bending magnet to the spectrometer. The beam is focused through a condenser to the sample plane and through the second objective to the detector. b) Illustration of twelve defocused IR beams onto the FPA detector. c) Image of the visible portion of the synchrotron beams. Reprinted with permission from [28].

Because water is a strong IR absorber, benchtop chemical imaging with blackbody thermal sources is limited in attainable spatial resolution and/or SNR when imaging live cells that are immersed in water or require aqueous environments. In this way, use of the bright synchrotron source provides distinct advantages; as it overcomes the SNR problem for thin layers of water [41-43] and recent developments in flow cells [44-46] make these experiments feasible. Using multi-beam synchrotron source, reaching biologically relevant spatial and temporal scales, new

information on short length and time scales can be obtained in a simultaneous and rapid fashion in living cells or tissue. These developments have been critical steps forward for the field, as diffraction-limited chemical images can be collected for living cells *in vivo* in a matter of minutes, a critical aspect for the field of living cells which can evolve and move over short time-scales.

## 2.10. Applications

FTIR spectroscopic imaging has a wide range of applications in the study of biological specimen that can provide information on morphology and structure of cells and tissues. There are numerous applications in pathology, neurology, and cancer diagnosis shown in several studies. Here, I present some examples from various biological cells and tissues, performed during my PhD studies to provide an illustration of possibilities.

### 2.10.1. Dorsal root ganglion neurons

Based on both morphological and functional criteria, dorsal root ganglion (DRG) neurons isolated from adult mice can be classified into large-diameter (≥27 μm) and small-diameter (< 27 μm) somata. DRG neurons with large somata tend to have myelinated Aα and Aβ axons in vivo [47] and generally conduct proprioceptive or mechanical information from peripheral targets at high velocities. DRG neurons with small to medium-diameter somata tend to correspond in vivo to unmyelinated C fibers and Aδ fibers. Many of the small diameter DRG neurons are nociceptive, or pain-sensing [48-50] or thermosensors and conduct information from pain and thermal receptors at low velocities [51]. A further population of small neurons is low- threshold C fibers that convey gentle touch and skin stroke [52]. The organization of how the peripheral nervous system senses painful stimuli and the alterations that occur during chronic pain states has been a central topic in the research of acute and chronic peripheral pain. However, one of the

major complexities for determining the underlying mechanisms of pain is that dorsal root ganglia (DRG) neurons, which comprise sensory nerves, are exceptionally heterogeneous, in that there are many functionally distinct subpopulations, some of which respond to light touch, heat, cold or endogenous or exogenous chemical stimuli.

Fourier transform infrared (FTIR) widefield microscopy provides label-free imaging that detects the distribution of biologically relevant components in cells at subcellular level. The importance of sample preparation and cell cultures for infrared measurements, for DRG neurons placed on $CaF_2$, $BaF_2$, and glass substrates are discussed elsewhere [53].
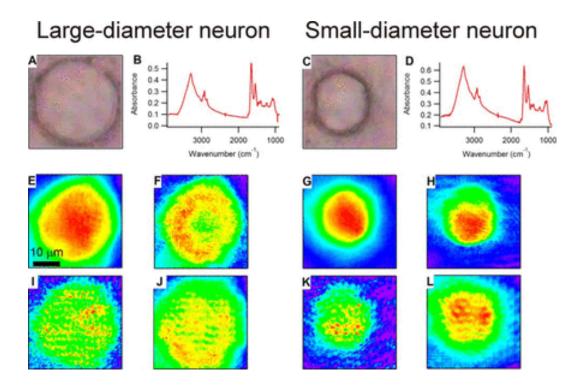
**Figure 2.7:** A,C) visible images of a representative large-diameter (A) and small-diameter (C) neuron. Average mid-infrared spectra of the respective neurons, generated by averaging the spectra from each pixel occupied by the somata, are shown in B and D. E–L show chemical images generated for amide (E and G), hydrocarbon (F and H), phosphate (I and K), and carbohydrate (J and L) for the large-diameter and small-diameter neurons, respectively. All of the visible and IR images represent a field of view that is the same size, so the scale bar in E represents 10 μm and applies to all images. Reprinted from [13].

Chemical images and IR absorption spectra from large diameter (LD) and small diameter (SD) neurons obtained from intact DRGs are displayed in Figure 2.7. Average spectra identify the infrared bands associated with the vibrations of the major functional groups of proteins, hydrocarbons, carbohydrates and phosphates. The following spectral regions as indicators of specific functional groups are used: 2800 –3000 $cm^{-1}$ (C–H stretching of hydrocarbons, primarily lipids), 1600 –1700 $cm^{-1}$ (C-O stretching of amide functional groups in protein), 1200 –1268 $cm^{-1}$ ($PO^{2-}$ asymmetric stretching of phosphates in lipids, sugars, and nucleic acids), and 1000–1135

cm$^{-1}$ (mixed C–O–H modes of carbohydrates). The region from 3000 to 3600 cm$^{-1}$ has contributions from N–H stretching modes from proteins as well as O–H stretching modes from water and carbohydrates. Integrating the area under the spectral regions with a corresponding baseline at each pixel generated chemical images. The chemical images were pseudocolored to illustrate relative abundance or density of the corresponding functional groups such that red delineates regions of high relative abundance, and blue indicates areas of low relative abundance (Fig. 2.7).

Relative lipid content in different subpopulations of DRG neurons, segregated by size (large- and small-diameter), treatment (naive and CFA inflammation), and genotype (wild type and TRPA1 KO) are calculated. The results from wild-type neurons and neurons from naive and CFA-injected TRPA1 KO mice are then compared. In small-diameter, wild-type neurons, I observed a significant (p 0.001) increase in relative lipid content following CFA inflammation as compared with naive control neurons. Interestingly, this effect was diminished in TRPA1 KO neurons, where following inflammation, the change in the relative lipid content failed to reach statistical significance (p 0.062). This difference in the effect of inflammation on TRPA1 KO versus wild- type neurons suggests that the increase in lipid content during inflammation is dependent in part on the expression TRPA1 [13]. I found that chemical morphology can define subpopulations of sensory neurons based on lipid and/or carbohydrate enrichment in chemical rings.
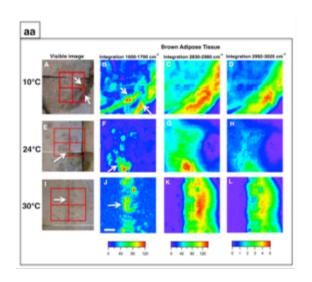
**2.10.2. Biochemical alterations in brown and subcutaneous white adipose tissues**
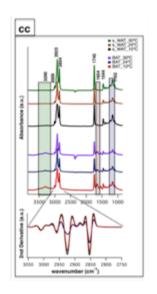
Numerous techniques have been used to determine the activity of adipose tissues and measure the whole body energy expenditure. Positron emission tomography (PET) with fluorodeoxyglucose (FDG) [54-56] is known as a primary method to detect BAT in humans. Despite outstanding clinical applications of PET-FDG, there are some limitations including ionizing radiation exposure, cost, procedure duration, and poor reproducibility of images [57,58]. Indirect calorimetry [59] is a non-invasive method that provides information on thermogenesis and metabolism; however, a lack of signal in inactive tissues, high-cost equipment, sensitivity to the measurement error, and sensitivity only to the steady state exercise condition, are some of the limitations. Computed tomography (CT) scanning [60] is another commonly used approach that provides the relationships between metabolic activity and body composition. Recently, PET-FDG/CT has been used to measure the activity of cold-induced BAT in a semi-quantitative manner. Infrared thermography [61] is also a thermal imaging technique that has been developed for predicting the presence of BAT. In addition, hyperpolarized $^{13}$C imaging [62], BOLD MRI [63], and hyperpolarized xenon MRI [64] have been used to detect BAT in rodents. Non-invasive near-infrared spectroscopy technique is also employed to detect human BAT [65]. Therefore, there is a necessity to develop alternative imaging methods to investigate the activity of BAT and s-WAT due to the significance of these tissues.
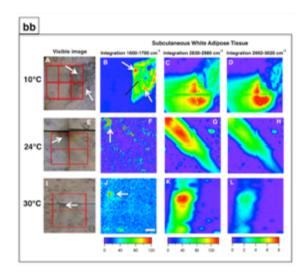
FTIR imaging permits detecting the inherent vibrational mid-infrared (IR) spectra of the biochemical constituents of the cells and characterization of the localized biochemical changes. Due to the sensitivity of IR spectra to the concentration of components in a sample, this method serves as a quantitative and qualitative technique. In this study, for the first time, I suggest that the combination of FTIR imaging and chemometric tools is a promising alternative approach to

detect the biomolecular changes attributed to cold acclimation in BAT and s-WAT excised from mice. FTIR microspectroscopy has been previously applied to obesity research including determination of fatty acids in human abdominal fat [66], obesity-induced alterations in BXD recombinant inbred mice [67], determination of fat content in liver tissue [68], and obesity-induced alterations in subcutaneous and visceral adipose tissues [69]. Other vibrational spectroscopic methods have also been applied to the field of obesity such as Raman spectroscopy [70] and coherent anti-stokes Raman microscopy [71].
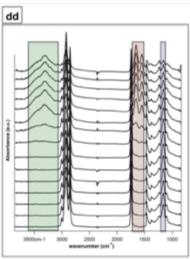
**Figure 2.8:** Chemical images derived from BAT (aa) and s-WAT (bb) at 10°C, 24°C and 30°C are shown. Panels A, E, I are visible images of adipose tissues. Each tissue covers the area of $280 \times 280$ μm$^2$ ($2 \times 2$ tiles; each tile = $64 \times 64$ pixels; each pixel = $2.2 \times 2.2$ μm$^2$). Chemical images from integrated area under 1600-1700 cm$^{-1}$ associated with proteins (Panels B, F, J), 2830-2980 cm$^{-1}$ associated with saturated lipids (Panels C, G, K), and 2992-3020 cm$^{-1}$ associated with unsaturated fatty acids (Panels D, H, L) are demonstrated. Colors indicate component gradients from low (blue) to high (red) and the values are demonstrated below each panel. The scale bar is 40 μm. cc) Average of nearly 1000 individual pixel spectra (3600-900 cm$^{-1}$) and a corresponding second derivative spectra (3050-2750 cm$^{-1}$) for BAT and s-WAT at 10°C, 24°C, and 30°C are demonstrated. dd) stack of spectra from the linescan drawn in Figure 2.8-bb/Panel B is shown. The starting pint is the green dot in the purple region of the image. The protein regions of the spectra are highlighted with purple, pink, and green rectangles in Panel dd to show the differences in protein absorbance. Reprinted from [72].

In the present study, BAT and s-WAT derived from thermoneutral (control, 30 °C), room temperature -maintained (24 °C) and cold-exposed (10 °C) mice were investigated. The potency of cold exposure in stimulating adipose tissues was evaluated by quantitative measurement of messenger RNA (mRNA) expression levels of UCP-1, Dio2 and Cidea. I present a novel chemometric-based method to detect the regions of interest within adipose tissue thin-sections. Individual pixel IR spectra (n=600) derived from 30 °C, 24 °C, and 10 °C BAT and s-WAT and used for measuring the ratio of several IR bands. Principal component analysis (PCA) and ANOVA model with post-hoc F-test were also used in this study to determine classification between the studied groups. Complementary $^{1}$H NMR measurements were performed on BAT and s-WAT and MR-based olefinic: lipid ratio was used as an additional proxy to correlate with IR-based results.

Visible images of BAT/s-WAT sections at 10°C (Figure 2.8-aa/bb - Panel A), 24°C (Figure 2.8-aa/bb – Panel E) and 30°C (Figure 2.8-aa/bb - Panel I) are demonstrated. Spectral maps were generated from integrating over different spectral regions including 1600-1700 cm$^{-1}$ (proteins-Amide I (Panels B, F, J)), 2830-2980 cm$^{-1}$ (Lipids - $CH_2$ and $CH_3$ stretching (Panels C, G, K)), and 2992-3020 cm$^{-1}$ (Olefinic - unsaturated fatty acids (Panels D, H, L)). Distribution maps were derived from four adjacent tiles (2×2 tiles), covering the area of about 280×280 μm$^2$ within the section of a tissue. Chemical images reveal the relative concentrations of each functional group on a rainbow color scale, (red (blue)/highest (lowest) intensity) to correspond to the absorption intensity and therefore concentration. The blue/purple background denotes the lack of biological material, while the green to red distributions shows elevated levels. The segments of the adipose tissues marked with white arrows in the visible images (Figure 2.8-aa/bb - Panel A, E, I) were detected by FTIR imaging (Figure 2.8-aa/bb - Panel B, F, J).

Figure 2.8-cc demonstrates IR average spectra from BAT and s-WAT (30°C, 24°C, 10°C) that highlight the IR bands attributable to carbohydrates, proteins and lipids. Lipids dominate the mid-IR spectral region 3050-2800 cm$^{-1}$. The band at 3009 cm$^{-1}$ attributed to olefin and unsaturated fatty acid was observed in both BAT and s-WAT. Similarly, the four lipid bands at 2854 ($v_s$ $CH_2$), 2873 (vs $CH_3$), 2923 ($v_{as}$ $CH_2$) and 2960 cm$^{-1}$ ($v_{as}$ $CH_3$) respectively, were observed in the spectra from both BAT and s-WAT. Clear differences in spectrum content, in particular in the heights of characteristic protein peaks in the spectral regions 3600-3100 cm$^{-1}$ attributed to N-H and O-H stretching, Amide I (1700-1600 cm$^{-1}$) and Amide II (1570-1500 cm$^{-1}$) peaks, between BAT and s-WAT were observed. The highlighted green, pink, and blue boxes represent the variations in the absorption strength of the bands between the tissues (Figure 2.8-cc). Absorption bands at 1163 cm$^{-1}$ attributed to C-O-C stretching of the ester functionalities and

1745 cm$^{-1}$ assigned to C=O stretching of the carbonyl group are also seen in the spectra from BAT and s-WAT. Figure 2.8-dd shows the stack of spectra along the linescan drawn in the Figure 2.8-bb/ Panel B. The first 8 spectra in Figure 2.8-dd show lack of protein absorptions (highlighted rectangles); however, the rest of the spectra show elevated absorption of the protein bands at 3290, 1654, and 1544 cm$^{-1}$. The stack of spectra clearly shows the differences in the protein profile in different segments of the tissue.

### 2.10.3. *In situ* IR microspectroscopy (Time lapse FTIR widefield microscopy)

In situ IR microspectroscopy is performed using a customized flow cell, allowing for measurements ranging from living cells in liquid media to gas adsorption on solid films. FTIR spectroscopic imaging of living cells is challenging due to the suspension of many cells in aqueous environments. Water is strongly absorbing in the mid-IR region, and optical path lengths of water greater than 25 μm result in total absorption over a considerable portion of the mid-IR region. Schematics of the microfluidic chamber used to maintain the diatoms (*Thalassiosira weissflogii*) alive and perform IR measurements are shown in Figure 2.9. Demountable flow chambers open [36,43,46] and closed [72] micro fluidic devices are used by several groups in live cell studies.

Time dependent macromolecule changes in *Thallasosira weissflogii* due to elevated carbon dioxide exposure were studied. Widefield spectromicroscopy was used to study changes in concentrations of carbon containing macromolecules due to environmental stresses by rapidly imaging single Thalassiosira weissflogii algal cells maintained in a microfluidic chamber. These data result in a series of temporally-resolved IR images, enabling chemically specific visualization that is unattainable with visible imaging, of on-going chemical processes and morphology in live cells.

Diatoms were diluted once a week, in order to have the population always in exponential growth (remove half of the culture and add the same volume of new medium) and then were exposed to high $CO_2$ medium (5000 ppm $CO_2$) prior to IR measurements, and then maintained within the microfluidic chamber at fixed temperature (20 °C) in 10 μL of $CO_2$ controlled medium fixed with a 15 μm spacer, and continually illuminated with photosynthetically active light. A background or reference spectrum is taken at the measurement position on the sample before the target gases are introduced to the cell. Then a controlled flow rate of the target gas is introduced using a mass flow controller connected to the input tube of the flow cell while differential transmission spectra are recorded.
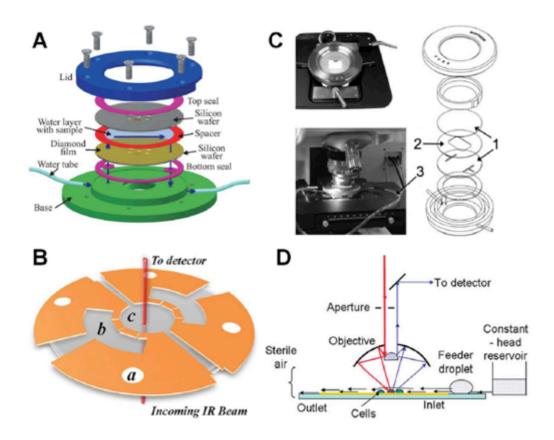
**Figure 2.9:** Different schemes of chambers for sustaining living cells. (A) Demountable liquid flow cell using submicrometer thick diamond windows (B) Fully-sealed microfluidic chamber employing 1 and 2 mm thick $CaF_2$ windows as the top and bottom windows, separated by an 8.5 μm photoresist layer. (C) Demountable liquid flow cell employing 2 mm thick CaF2 windows as the substrate and lid for the cell and (D) Open channel microfluidic design consisting of 10–15 μm deep microchannels embedded onto a Si chip with controlled inlet and outlet pressures. "Reprinted with permission from [36,43,46]. Copyright (2009) American Chemical Society."

Typically, these measurements are performed in transmission mode. The data sets were collected over a span of 8 hours. The most obvious changes in the spectral sequence and the IR images are seen in the carbohydrate/silica spectral band. Clearly, the intensity of this band changes from the beginning to the end of the experiment as is evident from the change in the color rendering of the images from the initial time point to the images generated from the time point taken at 8 h. Second, studying the spectral signatures show clear changes in the peak shapes, with the peak at 1040 $cm^{-1}$ getting smaller while there are minimal to no changes in the peak at 1080 $cm^{-1}$ (spectra not shown) [24]. The former peak is associated with carbohydrate functional groups, while the latter is associated with silica Si–O functional groups. Further changes are observed for the $CH_3$ and $CH_2$ functional groups, in both distribution and overall intensity. Time-lapse IR images are shown in Figure 2.10. This proof-of-principal experiment demonstrates the capability of following such changes in vivo with sufficient time resolution to capture the changes in real-time.
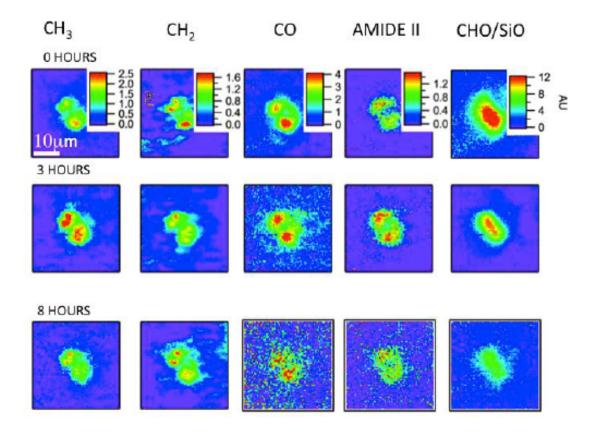
**Figure 2.10:** Temporally resolved series of IR images showing distributions of biochemically important functional groups and time dependent changes in the concentrations of several biochemical functional groups for a *Thalassiosira weissflogii* maintained in the flow cell. The images are obtained from data sets collected at 1, 3 and 8 h after exposure to medium containing a high concentration (5000 ppm) of $CO_2$. The images are displayed on a rainbow scale, with the red corresponding to the highest detected quantity of the functional group. Reprinted from [24].

## 2.11. References

1. Levin, I.W., and Bhargava, R. (2005). Fourier transform infrared vibrational spectroscopic imaging: Integrating microscopy and molecular recognition. Annual Review of Physical Chemistry 56, 429-474.

2. Hirschmugl, C.J., and Gough, K.M. (2012). Fourier Transform Infrared Spectrochemical Imaging: Review of Design and Applications with a Focal Plane Array and Multiple Beam Synchrotron Radiation Source. Applied Spectroscopy 66, 475-491.

3. Bambery, K.R., Schultke, E., Wood, B.R., MacDonald, S.T.R., Ataelmannan, K., Griebel, R.W., Juurlink, B.H.J., and McNaughton, D. (2006). A Fourier transform infrared micro spectroscopic imaging investigation into an animal model exhibiting glioblastoma multiforme. Biochimica Et Biophysica Acta-Biomembranes 1758, 900-907.

4. Krafft, C., Kirsch, M., Beleites, C., Schackert, G., and Salzer, R. (2007). Methodology for fiber-optic Raman mapping and FTIR imaging of metastases in mouse brains. Analytical and Bioanalytical Chemistry 389, 1133-1142.

5. McCann, M.C., Hammouri, M., Wilson, R., Belton, P., and Roberts, K. (1992). FOURIER-TRANSFORM INFRARED MICROSPECTROSCOPY IS A NEW WAY TO LOOK AT PLANT-CELL WALLS. Plant Physiology 100, 1940-1947.

6. Rhoads, C.A., Painter, P.C., and Given, P.H. (1987). FTIR STUDIES OF THE CONTRIBUTIONS OF PLANT POLYMERS TO COAL FORMATION. International Journal of Coal Geology 8, 69-83.

7. Mass, J., Sedlmair, J., Patterson, C.S., Carson, D., Buckley, B., and Hirschmugl, C. (2013). SR-FTIR imaging of the altered cadmium sulfide yellow paints in Henri Matisse's Le Bonheur de vivre (1905-6) - examination of visually distinct degradation regions. Analyst 19, 19.

8. Baker, M.J., Gazi, E., Brown, M.D., Shanks, J.H., Gardner, P., and Clarke, N.W. (2008). FTIR-based spectroscopic analysis in the identification of clinically aggressive prostate cancer. British Journal of Cancer 99, 1859-1866.

9. Bellisola, G., and Sorio, C. (2012). Infrared spectroscopy and microscopy in cancer research and diagnosis. American Journal of Cancer Research 2, 1-21.

10. Gasper, R., Mijatovic, T., Benard, A., Derenne, A., Kiss, R., and Goormaghtigh, E. (2010). FTIR spectral signature of the effect of cardiotonic steroids with antitumoral properties on a prostate cancer cell line. Biochimica Et Biophysica Acta-Molecular Basis of Disease 1802, 1087-1094.

11. Gazi, E., Dwyer, J., Gardner, P., Ghanbari-Siahkali, A., Wade, A.P., Miyan, J., Lockyer, N.P., Vickerman, J.C., Clarke, N.W., Shanks, J.H.*, et al.* (2003). Applications of Fourier transform infrared microspectroscopy in studies of benign prostate and prostate cancer. A pilot study. Journal of Pathology 201, 99-108.

12. Mattson, E. C., Nasse, M. J., Rak, M., Gough, K. M., & Hirschmugl, C. J. (2012). Restoration and spectral recovery of mid-infrared chemical images. Analytical chemistry, 84(14), 6173-6180.

13. Barabas, M.E., Mattson, E.C., Aboualizadeh, E., Hirschmugl, C.J., and Stucky, C.L. (2014). Chemical Structure and Morphology of Dorsal Root Ganglion Neurons from Naive and Inflamed Mice. Journal of Biological Chemistry 289, 34241-34249.

14. Hackett, M.J., Borondics, F., Brown, D., Hirschmugl, C., Smith, S.E., Paterson, P.G., Nichol, H., Pickering, I.J., and George, G.N. (2013). Subcellular Biochemical Investigation of Purkinje Neurons Using Synchrotron Radiation Fourier Transform Infrared Spectroscopic Imaging with a Focal Plane Array Detector. Acs Chemical Neuroscience 4, 1071-1080.

15. Tobin, M.J., Puskar, L., Hasan, J., Webb, H.K., Hirschmugl, C.J., Nasse, M.J., Gervinskas, G., Juodkazis, S., Watson, G.S., Watson, J.A.*, et al.* (2013). High-spatial-resolution mapping of superhydro-phobic cicada wing surface chemistry using infrared microspectroscopy and infrared imaging at two synchrotron beamlines. Journal of Synchrotron Radiation 20, 482-489.

16. Mansur, H.S., Sadahira, C.M., Souza, A.N., and Mansur, A.A.P. (2008). FTIR spectroscopy characterization of poly (vinyl alcohol) hydrogel with different hydrolysis degree and chemically crosslinked with glutaraldehyde. Materials Science & Engineering C-Biomimetic and Supramolecular Systems 28, 539-548.

17. Mignolet, A., Derenne, A., Smolina, M., Wood, B.R., and Goormaghtigh, E. (2016). FTIR spectral signature of anticancer drugs. Can drug mode of action be identified? Biochimica Et Biophysica Acta-Proteins and Proteomics 1864, 85-101.

18. Saptari, V., and Youcef-Toumi, K. (2004). Design of a mechanical-tunable filter spectrometer for noninvasive glucose measurement. Applied Optics 43, 2680-2688.

19. Griffiths, P. and Haseth, J. (2007). Fourier Transform Infrared Spectrometry. John Wiley and Sons.

20. Cooley, J.W. (1987). THE REDISCOVERY OF THE FAST FOURIER-TRANSFORM ALGORITHM. Mikrochimica Acta 3, 33-45.

21. Miller, L.M., and Dumas, P. (2006). Chemical imaging of biological tissue with synchrotron infrared light. Biochimica Et Biophysica Acta-Biomembranes 1758, 846-857.

22. Bhargava, R., and Levin, I.W. (2001). Fourier transform infrared imaging: Theory and practice. Analytical Chemistry 73, 5157-5167.

23. Holman, H.Y.N., Bechtel, H.A., Hao, Z., and Martin, M.C. (2010). Synchrotron IR Spectromicroscopy: Chemistry of Living Cells. Analytical Chemistry 82, 8757-8765.

24. Mattson, E.C., Aboualizadeh, E., Barabas, M.E., Stucky, C.L., and Hirschmugl, C.J. (2013a). Opportunities for Live Cell FT-Infrared Imaging: Macromolecule Identification with 2D and 3D Localization. International Journal of Molecular Sciences 14, 22753-22781.

25. Hirschmugl, C. (1992). INFRARED SYNCHROTRON RADIATIO INSTRUMENTATION AND APPLICATIONS. Nuclear Instruments & Methods in Physics Research Section a-Accelerators Spectrometers Detectors and Associated Equipment 319, 245-249.

26. Martin, M.C., Schade, U., Lerch, P., and Dumas, P. (2010). Recent applications and current trends in analytical chemistry using synchrotron-based Fourier-transform infrared microspectroscopy. Trac-Trends in Analytical Chemistry 29, 453-463.

27. Carr, G.L., Chubar, O., and Dumas, P. (2005). Multichannel Detection with a Synchrotron Light Source: Design and Potential in Spectrochemical Analysis using Multichannel Infrared Detectors. pp. 56-84.

28. Nasse, M.J., Walsh, M.J., Mattson, E.C., Reininger, R., Kajdacsy-Balla, A., Macias, V., Bhargava, R., and Hirschmugl, C.J. (2011). High-resolution Fourier-transform infrared chemical imaging with multiple synchrotron beams. Nature Methods 8, 413-U458.

29. De Juan, A., Maeder, M., Hancewicz, T., Duponchel, L., and Tauler, R. (2009). Chemometric tools for image analysis. Infrared and Raman spectroscopic imaging, 65–109.

30. Reffner, J.A., Martoglio, P.A., and Williams, G.P. (1995). FOURIER-TRANSFORM INFRARED MICROSCOPIC ANALYSIS WITH SYNCHROTRON-RADIATION - THE MICROSCOPE OPTICS AND SYSTEM PERFORMANCE. Review of Scientific Instruments 66, 1298-1302.

31. Carter, M.R., Bennet, C.L., Fields, D.J., and Hernandez, J. (1995). Livermore Imaging Fourier Transform Spectrometer (LIFTIRS) in Imaging Spectrometry. Proc SPIE, 380-386.

32. Moss, D., Gasharova, B., and Mathis, Y.L. (2006). Practical tests of a focal plane array detector microscope at the ANKA-IR beamline. Infrared Physics & Technology 49, 53-56.

33. Clemons, C., Sedlmair, J., Illman, B., Ibach, R., and Hirschmugl, C. (2013). Chemically imaging the effects of the addition of nanofibrillated cellulose on the distribution of poly(acrylic acid) in poly(vinyl alcohol). Polymer 54, 2058-2061.

34. Kastyak-Ibrahim, M.Z., Nasse, M.J., Rak, M., Hirschmugl, C., Del Bigio, M.R., Albensi, B.C., and Gough, K.M. (2012). Biochemical label-free tissue imaging with subcellular-resolution synchrotron FTIR with focal plane array detector. Neuroimage 60, 376-383.

35. Liao, C.R., Rak, M., Lund, J., Unger, M., Platt, E., Albensi, B.C., Hirschmugl, C.J., and Gough, K.M. (2013). Synchrotron FTIR reveals lipid around and within amyloid plaques in transgenic mice and Alzheimer's disease brain. Analyst 138, 3991-3997.

36. Tobin, M.J., Puskar, L., Barber, R.L., Harvey, E.C., Heraud, P., Wood, B.R., Bambery, K.R., Dillon, C.T., and Munro, K.L. (2010). FTIR spectroscopy of single live cells in aqueous

media by synchrotron IR microscopy using microfabricated sample holders. Vibrational Spectroscopy 53, 34-38.

37. Unger, M., Mattson, E., Patterson, C.S., Alavi, Z., Carson, D., and Hirschmugl, C.J. (2013). Synchrotron-based multiple-beam FTIR chemical imaging of a multi-layered polymer in transmission and reflection: towards cultural heritage applications. Applied Physics a-Materials Science & Processing 111, 135-145.

38. Mattson, E.C., Pande, K., Unger, M., Cui, S., Lu, G., Gajdardziska-Josifovska, M., Weinert, M., Chen, J., and Hirschmugl, C.J. (2013b). Exploring Adsorption and Reactivity of NH3 on Reduced Graphene Oxide. Journal of Physical Chemistry C 117, 10698-10707.

39. Mattson, E.C., Unger, M., Clede, S., Lambert, F., Policar, C., Imtiaz, A., D'Souza, R., and Hirschmugl, C.J. (2013d). Toward optimal spatial and spectral quality in widefield infrared spectromicroscopy of IR labelled single cells. Analyst 138, 5610-5618.

40. Riding, M.J., Trevisan, J., Hirschmugl, C.J., Jones, K.C., Semple, K.T., and Martin, F.L. (2012). Mechanistic insights into nanotoxicity determined by synchrotron radiation-based Fourier-transform infrared imaging and multivariate analysis. Environment International 50, 56-65.

41. Heraud, P., Stojkovic, S., Beardall, J., McNaughton, D., and Wood, B.R. (2008). INTERCOLONIAL VARIABILITY IN MACROMOLECULAR COMPOSITION INP-STARVED AND P-REPLETE SCENEDESMUS POPULATIONS REVEALED BY INFRARED MICROSPECTROSCOPY. Journal of Phycology 44, 1335-1339.

42. Heraud, P., Wood, B.R., Tobin, M.J., Beardall, J., and McNaughton, D. (2005). Mapping of nutrient-induced biochemical changes in living algal cells using synchrotron infrared microspectroscopy. Fems Microbiology Letters 249, 219-225.

43. Nasse, M.J., Ratti, S., Giordano, M., and Hirschmugl, C.J. (2009). Demountable Liquid/Flow Cell for in Vivo Infrared Microspectroscopy of Biological Specimens. Applied Spectroscopy 63, 1181-1186.

44. Birarda, G., Grenci, G., Businaro, L., Marmiroli, B., Pacor, S., Piccirilli, F., and Vaccari, L. (2010a). Infrared microspectroscopy of biochemical response of living cells in microfabricated devices. Vibrational Spectroscopy 53, 6-11.

45. Birarda, G., Grenci, G., Businaro, L., Marmiroli, B., Pacor, S., and Vaccari, L. (2010b). Fabrication of a microfluidic platform for investigating dynamic biochemical processes in living samples by FTIR microspectroscopy. Microelectronic Engineering 87, 806-809.

46. Holman, H.-Y.N., Miles, R., Hao, Z., Wozei, E., Anderson, L.M., and Yang, H. (2009). Real-Time Chemical Imaging of Bacterial Activity in Biofilms Using Open-Channel Microfluidics and Synchrotron FTIR Spectromicroscopy. Analytical Chemistry 81, 8564-8570.

47. Gavva, N.R., Bannon, A.W., Surapaneni, S., Hovland, D.N., Lehto, S.G., Gore, A., Juan, T., Deng, H., Han, B.R., Klionsky, L., *et al.* (2007). The vanilloid receptor TRPV1 is tonically activated in vivo and involved in body temperature regulation. Journal of Neuroscience 27, 3366-3374.

48. Lawson, S.N., and Waddell, P.J. (1991). SOMA NEUROFILAMENT IMMUNOREACTIVITY IS RELATED TO CELL-SIZE AND FIBER CONDUCTION-VELOCITY IN RAT PRIMARY SENSORY NEURONS. Journal of Physiology-London 435, 41-63.

49. Ritter, A.M., and Mendell, L.M. (1992). SOMAL MEMBRANE-PROPERTIES OF PHYSIOLOGICALLY IDENTIFIED SENSORY NEURONS IN THE RAT - EFFECTS OF NERVE GROWTH-FACTOR. Journal of Neurophysiology 68, 2033-2041.

50. Stucky, C.L., Dubin, A.E., Jeske, N.A., Malin, S.A., McKemy, D.D., and Story, G.M. (2009). Roles of transient receptor potential channels in pain. Brain Research Reviews 60, 2-23.

51. Lawson, S.N., Perry, M.J., Prabhakar, E., and McCarthy, P.W. (1993). PRIMARY SENSORY NEURONS - NEUROFILAMENT, NEUROPEPTIDES, AND CONDUCTION-VELOCITY. Brain Research Bulletin 30, 239-243.

52. Reichling, D.B., and Levine, J.D. (2009). Critical role of nociceptor plasticity in chronic pain. Trends in Neurosciences 32, 611-618.

53. Aboualizadeh, E., Mattson, E.C., O'Hara, C.L., Smith, A.K., Stucky, C.L., and Hirschmugl, C.J. (2015). Cold shock induces apoptosis of dorsal root ganglion neurons plated on infrared windows. Analyst 140, 4046-4056.

54. Cypess, A.M., Lehman, S., Williams, G., Tal, I., Rodman, D., Goldfine, A.B., Kuo, F.C., Palmer, E.L., Tseng, Y., Doria, A.*, et al.* (2009). Identification and Importance of Brown Adipose Tissue in Adult Humans. New England Journal of Medicine 360, 1509-1517.

55. Hany, T.F., Gharehpapagh, E., Kamel, E.M., Buck, A., Himms-Hagen, J., and von Schulthess, G.K. (2002). Brown adipose tissue: a factor to consider in symmetrical tracer uptake in the neck and upper chest region. European Journal of Nuclear Medicine and Molecular Imaging 29, 1393-1398.

56. Virtanen, K.A., Lidell, M.E., Orava, J., Heglind, M., Westergren, R., Niemi, T., Taittonen, M., Laine, J., Savisto, N.J., Enerback, S., and Nuutila, P. (2009). Functional Brown Adipose Tissue in Healthy Adults (vol 360, pg 1518, 2009). New England Journal of Medicine 361, 1123-1123.

57. Lee, P., Swarbrick, M.M., and Ho, K.K.Y. (2013). Brown Adipose Tissue in Adult Humans: A Metabolic Renaissance. Endocrine Reviews 34, 413-438.

58. Nedergaard, J., and Cannon, B. (2010). The Changed Metabolic World with Human Brown Adipose Tissue: Therapeutic Visions. Cell Metabolism 11, 268-272.

59. Simonson, D.C., and Defronzo, R.A. (1990). INDIRECT CALORIMETRY - METHODOLOGICAL AND INTERPRETATIVE PROBLEMS. American Journal of Physiology 258, E399-E412.

60. Lubura, M., Hesse, D., Neumann, N., Scherneck, S., Wiedmer, P., and Schurmann, A. (2012). Non-Invasive Quantification of White and Brown Adipose Tissues and Liver Fat Content by Computed Tomography in Mice. Plos One 7.

61. Jang, C., Jalapu, S., Thuzar, M., Law, P. W., Jeavons, S., Barclay, J. L., & Ho, K. K. Y. (2014). Infrared thermography in the detection of brown adipose tissue in humans. *Physiological Reports*, *2*(11), e12167.

62. Lau, A.Z., Chen, A.P., Gu, Y., Ladouceur-Wodzak, M., Nayak, K.S., and Cunningham, C.H. (2014). Noninvasive identification and assessment of functional brown adipose tissue in rodents using hyperpolarized C-13 imaging. International Journal of Obesity 38, 126-131.

63. Khanna, A., and Branca, R.T. (2012). Detecting brown adipose tissue activity with BOLD MRI in mice. Magnetic Resonance in Medicine 68, 1285-1290.

64. Branca, R.T., He, T., Zhang, L., Floyd, C.S., Freeman, M., White, C., and Burant, A. (2014). Detection of brown adipose tissue and thermogenic activity in mice by hyperpolarized xenon MRI. Proceedings of the National Academy of Sciences of the United States of America 111, 18001-18006.

65. Nirengi, S., Yoneshiro, T., Sugie, H., Saito, M., and Hamaoka, T. (2015). Human Brown Adipose Tissue Assessed by Simple, Noninvasive Near-Infrared Time-Resolved Spectroscopy. Obesity 23, 973-980.

66. Bortolotto, J.W., Reis, C., Ferreira, A., Costa, S., Mottin, C.C., Souto, A.A., and Guaragna, R.M. (2005). Higher content of trans fatty acids in abdominal visceral fat of morbidly obese individuals undergoing bariatric surgery compared to non-obese subjects. Obesity Surgery 15, 1265-1270.

67. Dogan, A., Lasch, P., Neuschl, C., Millrose, M.K., Alberts, R., Schughart, K., Naumann, D., and Brockmann, G.A. (2013). ATR-FTIR spectroscopy reveals genomic loci regulating the tissue response in high fat diet fed BXD recombinant inbred mouse strains. Bmc Genomics 14.

68. Kochan, K., Maslak, E., Chlopicki, S., and Baranska, M. (2015). FT-IR imaging for quantitative determination of liver fat content in non-alcoholic fatty liver. Analyst 140, 4997-5002.

69. Baloglu, F.K., Garip, S., Heise, S., Brockmann, G., and Severcan, F. (2015). FTIR imaging of structural changes in visceral and subcutaneous adiposity and brown to white adipocyte transdifferentiation. Analyst 140, 2205-2214.

70. Haka, A.S., Sue, E., Zhang, C., Bhardwaj, P., Sterling, J., Carpenter, C., Leonard, M., Manzoor, M., Walker, J., Aleman, J.O., *et al.* (2016). Noninvasive Detection of Inflammatory Changes in White Adipose Tissue by Label-Free Raman Spectroscopy. Analytical Chemistry 88, 2140-2148.

71. Nan, X.L., Cheng, J.X., and Xie, X.S. (2003). Vibrational imaging of lipid droplets in live fibroblast cells with coherent anti-Stokes Raman scattering microscopy. Journal of Lipid Research 44, 2202-2208.

72. Aboualizadeh, E., Carmichael, O.T., He, P., Albarado, D.C., Morrison, C.D., Hirschmugl C.J. (2017). Quantifying Biochemical Alterations in Brown and Subcutaneous White

Adipose Tissues of Mice Using Fourier Transform Infrared Widefield Imaging. Front. Endocrinol. 8:121.

73. Vaccari, L., Birarda, G., Businaro, L., Pacor, S., and Grenci, G. (2012). Infrared Microspectroscopy of Live Cells in Microfluidic Devices (MD-IRMS): Toward a Powerful Label-Free Cell-Based Assay. Analytical Chemistry 84, 4768-4775.

**Chapter 3: Chemometric tools and tissue classification**

Hyperspectral images from IR spectroscopic imaging provide massive dataset (spectral outputs from images), which include chemical information. Prior to image analysis, understanding of the chemical and mathematical properties of the measurement is crucial due to the specificity of each algorithm in providing outcome. Chemometric tools are critical in image analysis, especially in heterogeneous samples and complex tissues (e.g. diabetic tissue, cancerous tissue or tissue engineering) and detecting various species (e.g. bacterial species, impurities). Therefore, it is important to select the right algorithm among existing and in-progress methodologies in extracting structural information related to biomedical context. The main aim of chemometric tools are exploring the differentiation between image constituents based on their specific spectral fingerprints. In this chapter, I will discuss data pre-processing and noise reduction methods that are critical steps in obtaining robust and reproducible tissue classification. Then, I survey principles of some supervised and unsupervised methods that are highly used in spectroscopic studies with focus on merits, applications, and the drawbacks of each method. Finally, I will provide with some examples of my work in applying the chemometric tools and statistical analysis in classifying tissues and strains of bacteria.

**3.1. Introduction**

Spectroscopic data has been broadly used to understand the structure and biomolecular dynamics, consisting of hundreds of thousands of variables measured from number of samples [1]. Multivariate data analysis involves the analysis of large-scale data to determine all the spectral and spatial information and reveals the classes based on the similarities and differences in the spectral features (image segmentation). Chemometric tools [2] convert the original

variables into the latent variables to find the relationship between variables and number of samples. In both qualitative and quantitative analytical methods, chemometric tools are crucial in determining image constituents based on clustering the chemical composition of the pixels within an image. Employment of chemometric methods in biomedical spectroscopy is highly sought after, due to the richness and availability of myriad data. The main goal of this chapter is discussing general methods that a vibrational biospectroscopist may use in classification and pattern recognition of samples that leads to pathology. Chemometric tools in vibrational spectroscopic measurements (e.g. Raman, FTIR) include three major approaches. Enhancing the quality of data by improving signal to noise ratio, clustering between different classes by either supervised or unsupervised methods, and visualizing the data (new variables) to discern the differences in the dataset. The basic idea of classical multivariate image analysis is built on the bilinear model that decomposes the original dataset into pure spectra of the image constituents and the concentration values of these constituents. Therefore, one can segment the image into the pixels with similar chemical composition and generate spectral information attributed to each cluster. The rationale behind decomposing the dataset into smaller matrices is that the recorded data are repeated measurements of a small set of sample characteristics and that small set can represent the whole dataset as well as the spectral features. Although regression models [3] are helpful in identifying molecular structures of complex mixtures, there is a need for more accurate algorithms to help determine biochemical markers [4-6]. In biomedical spectroscopy, detecting alterations in tissue morphology (pixel to pixel variations in large areas) is crucial and therefore, pattern recognition techniques are more advantageous in this context. Experimental artefacts in spectroscopic data (raw data) can largely influence the chemometric analysis. There are some typical issues including the noticeable level of noise in the data, baseline effects, and bad pixels

43

(low absorbance) that have great impact on the image analysis and leads to misunderstanding of the classification. Thus, appropriate pre-processing methods can significantly improve the quality of the spectra [7]. In this chapter, I present some methods that are mainly used in signal processing for decreasing the artifacts in the dataset.

## 3.2. Pre-processing methods

### 3.2.1 Baseline correction

Baseline correction is generally required when there is the presence of background effects in the signal [8,9]. Baseline removal is necessary prior to subsequent quantitative spectral analysis to successfully interpret the FTIR spectral features (e.g. peak positions, band areas, peak heights), or else it is easy to be misled. Baseline offset can vary from pixel to pixel on the detector and it can be aroused from either how the detector output voltage is mapped to the analogue-to-digital converter input voltage range or the generation of electron-hole pairs referred as dark current. The appearance of baseline effect is that of a sloping baseline that decreases towards longer wavelength (lower wavenumbers) and a spectral manipulation technique is needed to correct spectra with sloped or varying baselines. One can simply draw a low-order polynomial parallel to the baseline, and then this function is subtracted from the intensity values, if the baseline is independent of wavenumber. If the baseline has spectral shape, a more sophisticated approach is required to remove the baseline effect in the spectra [10,11]. There are different categories of chemometric methods for removing baselines (or "backgrounds") from data, including multiplicative signal correction (MSC) method, derivatization of spectra, or polynomial fitting [12-16]. It is critical to apply the most amenable method to the data; therefore, understanding the characteristic of baseline effect is a need. MSC and similar full-matrix methods require the full dataset (all spectra along with the concentrations for all samples) to be

44

loaded and the procedure is faster. However, it is not a suitable method for correcting individual spectra upon acquisition and also this method highly depends on the quality of the raw spectra since an outlier can impede the correction.

Derivatizing the spectra is one of the most common and heavily used preprocessing methods in vibrational spectroscopy. The first derivative spectrum removes the constant offset from the spectrum, while the second derivative removes both constant offset and linear drifts in the spectrum. However, the second derivative spectrum retains all subtle spectral bands attributed to the chemistry of the sample. Although derivative preprocessing in removing the baseline effects is widely used, adding the noise structure to the spectra is one of the major drawbacks in this method.

Another method to remove baselines from data in more complicated forms is by including a baseline function (polynomial function) when fitting a sum of functions to the data and then subtracts it from the original spectrum [17]. This can be done by dividing the spectrum into N ranges and determine the lowest points in every range. The first baseline is built out of these initial points. Then, the spectrum is brought down by the difference between the lowest point in the current range and the lowest point on the baseline. Lieber and Mahadevan-Jansen proposed an automated straightforward method for removing baseline effects by fitting polynomials in iterative mode to the spectra [18]. In this method, the shape of original spectrum is retained and allows spectroscopist to evaluate the corrected spectrum, while interpreting the spectra in derivative preprocessing is challenging. There are additional methods to remove the baseline modulations either by performing FFT (Fast Fourier Transform) and filter out the lowest wavenumbers or using cosine functions with multiple long wavelengths and perform a linear fit to the data. In the latter, one can filter out the spectra by weighting the data points with their

intensity.

### 3.2.2. De-noising

Signal to noise ratio (SNR) is a quantity that has been used to measure signal strength and detectability relative to the noise. It is critical to perform quality test on spectroscopic data prior to multivariate image analysis and eliminate the pixels with low SNR, since the presence of poor SNR spectra can lead to misunderstanding of the chemistry and pathology. The process of noise removal in the data requires understanding the characteristic property of noise, which is distinct from that of the signal. Recently, new methodologies are developed to de-noise spectroscopic data and most of the methods are amenable to hyperspectral images [10]. Some methods are based on smoothing spectra (e.g. Least-squares polynomial smoothing) that can be done by fitting a polynomial function to a set of input samples. Mathematical signal filtering methods including wavelet transform, statistical reconstruction, and FFT-based filters [19] are some techniques to improve SNR in the chemical spectrum. In FTIR imaging, it is vital that the noise removal method reduces noise while maintaining the shape and the height of the spectral peaks. Other methods, such as multivariate covariance method, are gaining interest in the field of vibrational spectroscopy, especially where large numbers of spectra have to be recorded [20]. Briefly, This approach, for example, a principal component analysis (PCA), decomposes the original data matrix into a set of eigenvalue images via forward transformation. Only selected number of eigenvalue images represents chemical distribution in the data and the rest are attributed to the noise. After selecting the eigenvalue images with sufficient SNR, an inverse transform is performed to reconstruct the data with lower noise content and higher SNR. An example of raw spectroscopic data, baseline corrected, and de-noised via PCA are shown in Figure 3.1.
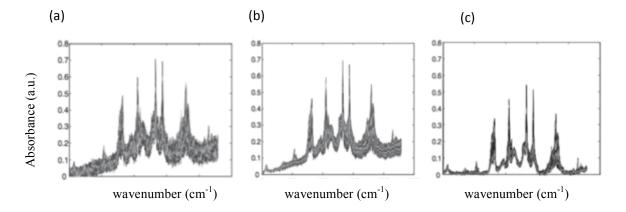
**Figure 3.1:** Raw spectra of an emulsion layer image (a) after de-noising (b) and after de-noising along with baseline correction (c) by least squares. Reprinted with permission from [5].

### 3.2.3. Spike Removal

In hyperspectral images, some pixels present either abnormal spectral readings or spectrum that is mostly dominated by noise (dead pixel) due to some instrumental artefacts. Detecting these artefacts that are known as "spike noise" is another step in pre-processing spectroscopic data prior to tissue classification. It is known that spike noise is generated from α-rays or γ-rays emitted from the materials around the detector chip. Another reason that spikes are seen in FTIR imaging data are employing larger detectors with increased integration times for imaging biological tissues [21]. The most common method to remove spikes from the data is local interpolation, which is using median values from regions of interest that can be used as a reference. In this method, neighboring pixels with acceptable SNR are used to smooth data, i.e. spikes and bad pixels can be replaced by interpolated spectra, taking as reference [22]. Another method to remove spikes in the FTIR spectra is defining both upper and lower threshold on absorbance values at certain wavenumbers. The threshold approach can be used to detect outliers in the spectra, as well [23]. For typical spectrum from biological specimen, one can consider amide I band (1690-1620 cm$^{-1}$) as signal and the absorption-free spectral region (1900-1800 cm$^{-}$

[1]) as noise content in the data. A threshold can also be applied to the area underneath the bands to find the outliers.

### 3.2.4. Normalization

In spectroscopic applications, different spectra that are recorded from the same material at different times and under different instrument conditions experience differences in intensity levels. These scaling differences can arise from scattering effects, alignments, pathlength effects, and variations in source or detector. Normalization is a pre-processing step that corrects the disparity in the intensity levels of the spectra recorded from the same sample under identical experimental parameters. Normalization helps spectroscopist to evaluate all the samples with an equal impact on the model, especially if the variance in the data is desirable. In discriminant analysis such as PLS-DA or PCA methods, classification results are significantly different with or without normalization. Normalization is typically performed after baseline correction and offset removal in FTIR spectral analysis [24]. There are four typical normalization techniques that are summarized below.

Let's assume the spectrum to be normalized is 'A' and the normalized spectrum is defined as '$A_N$', where N is the number of wavenumbers (data points) in the recorded spectrum.

$$A = (a_1, a_2, a_3, \ldots\ldots, a_N)$$

$$A_N = (a_{n1}, a_{n2}, a_{n3}, \ldots\ldots, a_{nN})$$

Each element of 'A' and '$A_N$' represents the intensity of the spectrum at a given wavenumber.

(1) Vector normalization

Vector normalization, is dividing each absorption intensity attributed to a wavenumber by the "norm" of the spectrum. Norm is defined as the square root of the sum of the squared spectral elements.

$$\text{norm} = \sqrt{(a_1^2 + a_2^2 + \cdots + a_N^2)}$$

$$a_{ni} = {a_i}/{\text{norm}} \; ; i = 1,2,\ldots,N$$

(2) Peak normalization

In peak normalization, the entire FTIR spectrum is normalized to the intensity of a particular wavenumber. Let's define the reference intensity as 'A', then the normalized spectrum is defined as:

$$a_{ni} = {a_i}/{A} \; ; i = 1,2,3,\ldots,N$$

This method is not recommended if there is a possibility of variations in peak position and peak height in the spectrum. In most cases, Amide I or Amide II bands are used as references for peak normalization, therefore this normalization is not an appropriate method if protein denaturation or alterations in protein structure are the points of the comparison.

(3) Min-Max normalization

First, the minimum and maximum values of all the intensities of the FTIR spectrum is calculated. Then, each intensity value corresponding to each wavenumber is replaced by a new

intensity value. The normalized spectrum in this method is calculated as follows:

$$a_{max} = \max(a_1, a_2, ..., a_N)$$

$$a_{min} = \min(a_1, a_2, ..., a_N)$$

$$a_{ni} = \left.(a_i\text{-}a_{min})\middle/(a_{max}\text{-}a_{min})\right. ; i = 1,2, ..., N$$

(4) Standard Normal Variate (SNV) normalization

This method is very similar to min-max normalization method with slight changes. The mean value for the intensity values are calculated and then divided by the standard deviation (S.D.).

$$Mean = \left.(a_1 + a_2 + \cdots + a_N)\middle/N\right.$$

$$S.D. = \sqrt{\left.((a_1\text{-}Mean)^2 + (a_2\text{-}Mean)^2 + \cdots + (a_N\text{-}Mean)^2)\middle/(N\text{-}1)\right.}$$

$$a_{ni} = \left.[a_i\text{-}Mean]\middle/(S.D.)\right. ; i = 1,2, ..., N$$

### 3.2.5. Scattering correction

The primary complication in the analysis of the FTIR spectrum of cells comes from scattering effects in the data. It is well known that scattering particles similar to the wavelength of incident IR radiation (3-10 μm) cause Mie-Type scattering [14,15]. Typical human cells are

50

mostly about 8-30 micron and the cell organelles ranges from 1-10 micron, which is very close to that of the IR radiation. This effect usually appears as a derivative-shape line in the high wavenumber side of Amide I band in the spectrum. Although it appears in the spectral region close to amide I, this phenomenon has influence on other peaks in the mid-IR fingerprint region, which leads to misrepresentation of the peak positions and the chemistry of cells.

In the presence of scattering features in the data, peak shapes, positioning, and intensities are not reliable to evaluate biochemistry of cellular features. Extended multiplicative signal correction (EMSC) is known as one of the most powerful methods in correcting scattering features and dispersion artefacts in mid-IR spectra, especially in the case of moderate Mie scattering where the amide I band (~1650 cm$^{-1}$) is not heavily distorted. EMSC is a multivariate data pre-processing method that is based on linear regression model to handle multiplicative effects and artefacts in the spectral data. EMSC has been widely used in spectroscopic data to correct the baseline effects and transform the distorted spectrum to the original spectrum and therefore, the chemical interpretation is more accessible. This method has been used in non-linear problems such as Mie scattering to remove offsets and baseline slopes as well as correcting optical pathlength differences in the spectra by means of multiplicative part of the model. In EMSC model, a second order polynomial function is used to correct the baseline effects. Assume $A^1$, $A^2$, ......, $A^M$ are the FTIR spectra and A is the average spectrum. Each spectrum can be written as:

$$A = (a_1, a_2, ..., a_N)$$

where N is the number of data points. Let's assume that $A_\nu^i$ is an intensity value of the spectrum at particular wavenumber $\nu$ for a given spectrum $A^i$. Then, EMSC transforms each spectrum in

terms of the average spectrum and a polynomial using the following equation:

$$A_\nu^i = \alpha^i + \left(\beta^i * A_\nu^\mu\right) + \left(\gamma^i * \nu\right) + \left(\delta^i * \nu^2\right) + \epsilon_\nu^i \; ; i = 1,2, \dots, M; \; \nu = 1, \dots, N$$

Once the parameters $\alpha^i$, $\beta^i$, $\delta^i$, and $\gamma^i$ are calculated, then the corrected spectrum is given by:

$$A\_EMSC^i = \left(E^i\big/_{b^i}\right) + A^\mu; i = 1, 2, \dots, L$$

Where $E^i = (\; \varepsilon_1^i, \varepsilon_2^i, \dots, \varepsilon_N^i \;)$ is the residual spectrum.
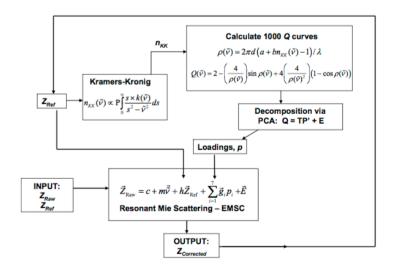


**Figure 3.2:** Flowchart demonstrating the iterative process for performing scattering correction using reference spectrum. Reprinted with permission from [16].

Van de Hulst initiated the first calculations of the Mie scattering efficiency, Q [25]. In this model, known as non-resonant Mie scattering EMSC model, Q is defined as a function of parameters such as the real refractive indices of particle, surrounding medium, and the diameter of scattering particles. Then, due to the non-linearity of Q and the complexity of implementing this non-linear function into pre-processing, this function is replaced by a multivariate bi-linear

model and incorporated into the linear EMSC model. Thus, one can estimate the parameters by the multivariate linear regressions and the resulting curves are loaded into PCA, to manipulate data in smaller dimensions. The described algorithm is successful at removing the smooth oscillations due to Mie scattering; however, the dispersion artefact often remains. These artefacts should be removed through resonant Mie scattering EMSC method, which is scattering when there is concurrent absorption [26].
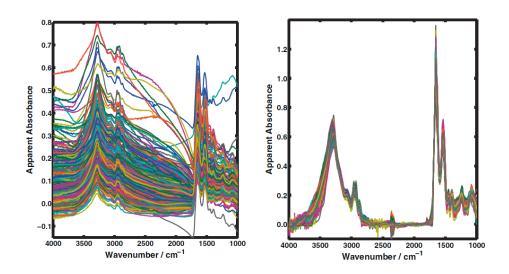


**Figure 3.3:** The mid-IR spectra before and after scattering correction using GPU-based algorithm. Reprinted with permission from [16].

The model, which has been used to correct both baseline effect and dispersion artefacts in the data, is based on generating Mie scattering curves (scattering efficiency) that are dependent on wavenumber and scatter diameter. It has been modeled that the size of scatters has an impact on the period of oscillation in the Mie scattering curves and the variations in the refractive index as a function of wavenumber is obtained by means of Kramers-Kronig transformations.

The procedure removes Mie scattering spectral features, and recovers pure absorption

spectra. The flowchart demonstrating the iterative procedure to correct scattering features in the FTIR data are shown in Figure 3.2. Scattering correction in our work was implemented using Graphics Processing Units (GPUs) for fast hyperspectral processing [16,27]. An overall procedure to perform scattering correction implementation on 800 images of 128 ×128 pixels takes about 12 seconds. The algorithm proposed by Bassan, et al. is used to implement the GPU-based scattering correction with some modifications [16]. The mid-IR spectra before and after scattering effect using GPU-based algorithm is shown in Figure 3.3.

## 3.3. Multivariate data analysis

The most critical step in practicing statistical analyses is to understand the logical structure of data, which provide insights to substantive chemical information conveyed by the data. Hyperspectral data are typically presented in the form of hypercube where two spatial dimensions represent the pixel coordinates and the spectral axis is the third dimension. One of the most important objectives of multivariate analysis is to extract the maximum variance in the data, where in the most cases this variation entails the morphological and chemical information of the data. The choice of appropriate multivariate analysis among existing methods highly depends on the goal of the analysis. There are three main objectives in multivariate image analysis namely, descriptive information of data structure, classification and discrimination between classes and groups of measurements in the data, and prediction and regression.

The multivariate analyses are generally split into "unsupervised" and "supervised" methods. Unsupervised methods do not rely on *a priori* information and are suitable to find subtle structural information in the unlabeled data. Unsupervised algorithm (e.g. PCA) performs classification based on the similarities of the spectra. Recently, unsupervised methods are used to

reduce the dimensionality of big data and also as a precursor to supervised methods. Clustering analyses such as K-means clustering and Hierarchical Clustering Analysis (HCA) are considered unsupervised methods.

On the other hand, supervised methods use previous knowledge and label the classes that need to be classified. The "training phase" and the "prediction phase" are two main phases of modeling stage in supervised algorithms. In the training phase, the dataset that is labeled (training dataset) is used to find the patterns in the data and the parameters that are obtained in this phase are used to validate the data (the data that are not included in the training dataset) in the prediction phase. Linear discriminant analysis (LDA), support vector machines (SVM), and partial least squares (PLS) are some examples of supervised methods. One of the major drawbacks of supervised algorithms is that they rely on labeling and it is burdensome to label every observation, especially in handling big data. Using supervised methods along with unsupervised methods has solved the issue. Initially all of the data are loaded into an unsupervised method and based on the obtained clusters, each observation is labeled. Moreover, this procedure enables us to handle the data in a lower dimensional space and filter out the spectral artefacts and noise in the data. PCA is the most common dimensionality reduction algorithm. Then, the labeled data are fed into supervised algorithm for further classification and to maximize the separation between classes.

### 3.3.1 Eigenvector based multivariate analysis

Multivariate image analysis provides simple ways to visualize image constituents by using information in both spectral and spatial directions, while preserving the relevant original information. Hypercube of data contains hundreds of thousands of spectral channels, although

55

the spectral data are highly redundant and affected by artefacts. Therefore, understanding the structure of data is vital prior to chemometric evaluation. Eigenvector based algorithm and in particular principal component analysis (PCA) is very common to determine the chemical composition of the image. PCA is a linear transformation of the original data that decomposes a dataset into bilinear latent variables called principal components (PCs) and reduces the dimensionality of the data while retaining most of the information in the data set. In PCA, Data are typically mean centered and the mean spectrum is used as comparator. Thus, PCA can be considered as a method that aims to explain the standard deviations from an average spectral property. The first component ($1^{st}$ PC) is accredited to an average intensity observed at every spectral data point and the second component represents the variations from the first component and subtle differences between groups of samples can be identified with standard statistics. PCA can be used for compressed representation of an image that retains most of the information based on the expression:

$$Y = V^T X$$

Where Y is the new data matrix after rotation, X is the original data matrix and $V^T$ is the vector of weights (termed as loadings). The weights attributed to different axes are illustrative of distinct spectral features assigned to sub-classes in the data that are classified based on variance. PCA is calculated based on the maximum variance contained in the dataset in descending order of importance and there is a null correlation between components.

However, the number of components in PC representation is equal to the number of spectral wavenumbers in the data, only the first few numbers of PCs can be used since the rest of the components do not account for the chemical information. Comparatively speaking, PCA is

identical to beer-lambert law in a matrix form and the number of components that describe an image can be interpreted as the number of constituents of an image. It means that taking every column in the scores matrix and refolds it into a two-dimensional image can be analogous to the distribution map. The PCA model and chemical images for FTIR images of retinal tissue are shown in Figure 3.4.

The advantage of working with scores and loadings representation is the reduced size of the big data and the efficacy to highlight and visualize the variations and heterogeneities in the biological tissue. Similar values in the scores matrix are attributed to different pixels but with the identical chemical composition in the original data. There is also a typical visualization of PC scores to detect pixel clusters by creating scatterplots without need of extra calculation and re-dimension process. The first three PCs typically account for 99% of the total variability of data and therefore used to create 2D scatter plots. The scatter plots from scores are helpful to visualize whether the score values are clustered or dispersed along each component. The second piece of information originated from PCA is the "loading spectra" that can be used to find relevant spectral features in the real spectra. The principal component loadings are used to infer the components and strength of components that correspond to the discriminatory features responsible for the classification. Further, by the comparison between the location of the clusters of points in the 2D score scatterplots and the variations seen in the PC loadings, one can correlate the clusters with positive (negative) scores to the loadings with peaks (troughs).
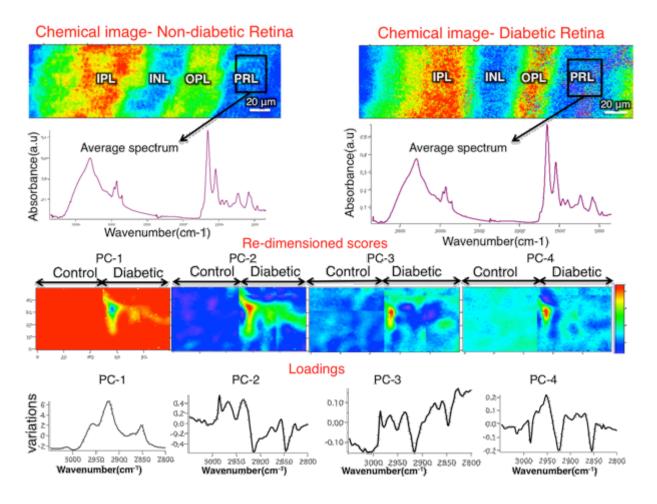
**Figure 3.4:** Chemical images of non-diabetic and diabetic retinal tissue processed at lipid band at 2850 cm$^{-1}$. Average absorption spectrum from the region of interest within the photoreceptor retinal layer is shown. Results from PCA including re-dimensioned scores for PC-1 to PC-4 and associated loadings plot for the lipid region 3050-2800 cm$^{-1}$ is shown.

The largest peaks or troughs in the loading plots are associated with the largest variances in the score plots. The difference between the real spectra and the loading spectra is the existence of some negative bands in the loading plot, which comes from the fact that loading spectra are completely uncorrelated and principal components are calculated under the condition that there is a null correlation between components. However, PCA is very well designed to reduce the dimensionality of the original data and meanwhile maintain most of the relevant information in

the original data. 2D scores distribution map highlights the regions with the highest variations within original data and can be used to correlate with the biggest variations observed in the loading spectra. Therefore, pixels with identical chemical composition have the same PC score value and this idea has been used in some image segmentation algorithms.

I am less interested in using PCA for the purpose of tissue classification and spectral pathology. Failure of this method in identifying instrumental artefacts or correlated noise in classification and the inability of using *a priori* information about the samples are two major drawbacks in using pure PCA in classification. However, there are several classification studies with limited number of image constituents where PCA provides robust and accurate classification and identification [28-34]. In my case study, PCA has been used as an initial pre-processing step to provide a priori information for further sophisticated classification techniques that will be discussed later in this chapter. PCA-based algorithms have advantages of noise reduction property [35] that is implicit in PCA and the orthogonality of the components, which make the classifications robust, accurate, and comparable to non-linear methods [36].

### 3.3.2 Hierarchical Clustering Analysis

Hierarchical clustering analysis (HCA) [37] involves partitioning the dataset to multiple steps such that a single cluster of the entire dataset is successively formed into separate clusters. HCA is a chemometric tool to classify dataset by evaluating distances between spectra/clusters. Amongst various existing methods, Ward's algorithm together with Euclidean distance is known as the most efficient method. Hierarchical clustering could be divided into agglomerative and divisive methods. In agglomerative clustering method, the algorithm starts with n clusters of size 1 and then forms the first cluster of size 2 and n–1 clusters of size 1. In the next step, one has either 1 cluster of size 3 and n-1 clusters of size 1 or 2 clusters of size 2 and n-2 clusters of size

59

1. This procedure continues until all data are combined into a single cluster of size n. In divisive method, the algorithm starts from a single group of N objects and ends when each cluster contains a single object. Agglomerative method is more common in spectroscopic data and the results are typically demonstrated as tree of connections termed as dendrograms. An example of dendrogram is shown in Figure 3.5. In agglomerative clustering, two spectra with the smallest spectral distance (highest similarity) form a new cluster and then the distance between other spectra and the formed cluster is calculated. Again the two clusters/spectra with the highest similarity form another cluster and the software repeats this procedure until one big cluster is left. This method tries to minimize the sum of squares of two clusters that are formed during the whole procedure. The distance between cluster i and cluster j with a new cluster k is calculated based on the following equation:

$$d_{k,ij} = \frac{[(c_k + c_i)d_{ki} + (c_j + c_k)d_{kj} - c_k d_{ij}]}{c_i + c_j + c_k}$$

Where $d_{ki}$ is the Euclidean distance between clusters k and i calculated in the first step, $d_{kj}$ is the distance between clusters k and j and $d_{ij}$ is the distance between clusters i and j. $c_{i,j,k}$ is the number of units in clusters i, j and k.

**Cluster dendrogram with AU/BP values (%)**



Distance: euclidean
Cluster method: ward.D2
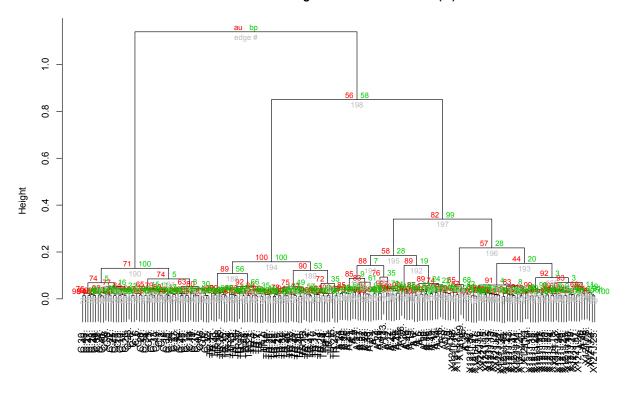
**Figure 3.5:** Schematic illustration of a dendrogram. The x-axis shows the number of samples and the y-axis shows the distance between clusters.

There are some major benefits of hierarchical clustering in spectral analysis. Since hierarchical clustering is an unsupervised method, no prior information of classes in the data is needed. In addition, the organization of clustering can be visualized at every single step of the analysis and provides the estimate of heterogeneity, and the chemical information (spectral features) regarding each class can be obtained. Hierarchical clustering has been widely used in spectral analysis and visualizing the data including classification of microbial species [38-41], pathology of tissues [42], and drugs [43]. Results drawn from hierarchical clustering could also be linked to clinical application via two parameters namely sensitivity and specificity. The

61

sensitivity refers to the number of diseased samples that are clustered in a disease group (true positive) and specificity refers to the number of control samples that are clustered in a control group (true negative). These parameters help to quantify false positive and false negatives in tissue classification. Owing to this knowledge, one can infer the progress of disease based on the sensitivity factor of tissues at different stages of the disease and compare the biological variations.

### 3.3.3 K-means clustering

K-means clustering [44-46] is an unsupervised learning algorithm that works iteratively to assign each data point to one of K clusters based on the number of clusters that are fixed a priori. The aim of k-means clustering is finding the positions of the clusters that minimize the distance from the data points to the cluster. The main idea is defining a centroid for each cluster that can be used to label the new data. The centroids are placed far from each other at the first step and then associate each data point to a centroid. When no point is pending, the first group is formed. At this step, one has to re-calculate K new centroids as bary-center of the clusters resulting from previous step. After defining k new centroids, the same data points should be assigned to the nearest centroids and the loop is generated. Therefore, when the loop starts running, the centroids change from step to step and the loop stops until there is no further change in the centroids. The algorithmic steps to perform k-means clustering are listed below.

1) Assume that X= {$x_1$, $x_2$, $x_3$, …… , $x_n$}be the set of data points and Y= { $y_1$, $y_2$, $y_3$, …… , $y_n$} be the set of centroids.

2) Select "m" cluster centers randomly.

3) Calculate the Euclidean distance between every data point and cluster centers.

www.manaraa.com

4) Associate each data point to the cluster center whole distance is minimum from the cluster center (among all cluster centers).

5) Recalculate the new cluster center using the following equation:

$$y_i = \left(\frac{1}{m_i}\right) \sum_{j=1}^{m_i} x_i$$

Where $m_i$ represents the number of data points in the $i^{th}$ cluster.

6) Recalculate the distance between data points and the new cluster center.

7) If no data point is pending, then algorithm stops, otherwise repeat from step 4.
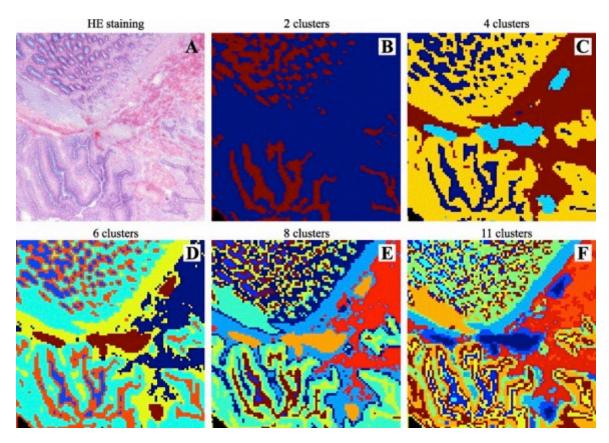


**Figure 3.6:** Spectral maps of colorectal adenocarcinoma derived form K-means clustering. A) H&E-stained specimen. Re-assembled spectral maps after 2 points (B), 4 points (C), 6 points (D), 8 points (E), and 11 points (F) clustering. Reprinted with permission from [51].

K-means is an efficient and robust clustering method, especially when the number of clusters is known and the data forms natural classes. However, the choice of the number of clusters is challenging and requires *a priori* specification of the clusters in the data. The data requires extensive pre-processing due to an inability of algorithm in handling outliers and noisy data. Each centroid of a cluster is a collection of feature values, which define the resulting groups. The centroid feature weights can be used for qualitative interpretation of the classes obtained from k-means clustering. An example of tissue classification and segmentation using k-means clustering is demonstrated in Figure 3.6.

### 3.3.4 Bayes Classifier

The Bayesian classification [47] is a supervised learning method based on Bayes' theorem, which predicts a class value given a set of attributes for each known class value. This method enables us to capture uncertainty about the model by calculating probabilities of the outcomes. Naïve Bayes classifier model assumes that there is no correlation between one specific feature in a class to the rest of the features in that class. A decision rule is based on probabilities to assign instance $\vec{D}$ to class $C_j$, which is the most probable class. Bayes theorem calculates probability of the observed $\vec{D}$ (posterior probability) using the following equation:

$$p\left(C_i \middle| \vec{D}\right) = \frac{p\left(\{\vec{D}\middle| C_i\}\right) p(C_i)}{p(\vec{D})}$$

Where $p\left(C_i\middle|\vec{D}\right)$ is the probability of an instance $\vec{D}$ being in class $C_i$ (what we are trying to compute), $p\left(\{\vec{D}\middle|C_i\}\right)$ represents the probability of having feature $\vec{D}$ with some probability (likelihood), $p(C_i)$ represents the frequency of the class $C_i$ in our data (class prior probability), and $p(\vec{D})$ is the predictor prior probability that is the same for all classes. In case of having

64

multiple features, Bayesian classifier assume independent distributions for each attribute; therefore, the probability of class $C_i$ generating instance $\vec{D}$ is calculated using the following equation:

$$p(\vec{D}|C_i) = p(D_1|C_i)*p(D_2|C_i)* \dots . p(D_n|C_i)$$

Bayes classifier method works well in multi class predictions, handles real and discrete data, and it is not sensitive to irrelevant features. However, one of the major drawbacks of this method is that in real life, getting a set of predictors that are entirely independent is almost impossible. Bayes classifier method can be applied to every pixel in a hyperspectral cube of data to determine the probability of an unknown spectral pattern originated from a particular class. This method classifies the individual pixel spectra within an entire imaging data, regardless of the spatial position of that pixel. This method permits probabilities of occurrence of different classes, which could be critical in evaluating the risk of misclassification.

### 3.3.5. Artificial Neural Network

Neural networks [48] are among the most well known classification methods, and are typically made of number of layers. Artificial neural network (ANN) algorithm consists of input layer or input "nodes" and an output layer along with some hidden layers (called neurons) that link input nodes to an output layer in a non-linear fashion. The processing in hidden layers in done via a combination of weighted connections. The patterns from input layer enters the processing element and are multiplied by weighting factors, then the modified inputs are loaded into a summing function that sums the input products.

65
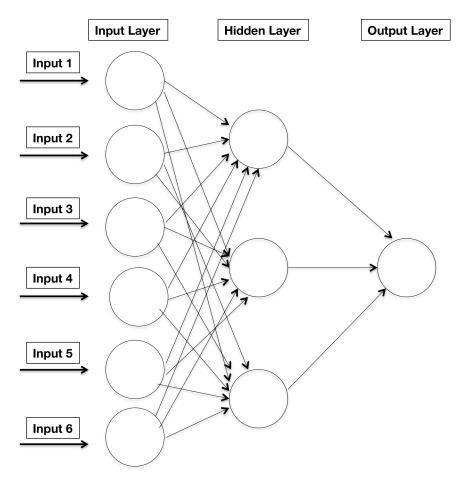
**Figure 3.7:** Schematic illustration of neural network architecture. The inputs are the features attributed to different classes and selected through training process the known object class for each training object is forced to be the result of the output layer. Then, the hidden and output layers perform non-linear operations on their inputs. The connecting lines are weights that are computed in training procedure and propagate the features from an input layer to the output layer via hidden layer.

ANN requires a learning rule, which modifies the connections between the neurons based on the patterns in the input layer. Most of the developments that have been applied to ANN method are by modifying the learning rules and connection formulas. While the connection units are optimized and the prediction errors are minimized, the network is trained and ready to be given new inputs. ANN has a broad range of applications such as pattern recognition, classification, and prediction. The main advantage of ANN is the ability to handle very large

datasets with large number of parameters, even when distribution of parameters is complex.

ANN has been widely used in Raman and FTIR spectroscopic data to determine the concentration of biological substances such as identifying bacterial species [49,50], determination of blood glucose [52], diesel analysis [53], assessment of brain tumors [54], detection of food products [55], and biochemical changes in melanoma tissues [56]. Schematic diagram of neural network architecture is demonstrated in Figure 3.7.

ANN like any other machine learning algorithm has some limitations. A major criticism arises from the learning rule that works in a sense of "black box". The user has no role over the procedure, which makes it impossible to determine which spectral features is used for classification and which are discarded. Therefore, the results are highly dependent on the choice of initial parameters. Another common problem is the amount of time that takes to visualize data and extract input features and also train a dataset on a standard computer, especially when handling complex dataset. On the other hand, insufficient training of dataset leads to errors in classification; however, there is no general rule for choosing the amount of required training. ANN often overfit the dataset i.e. if training continues for a long time, there is a risk of including noise and artefacts as part of the pattern. Additionally, ANN converges on local minima rather than global minima, meaning that losing important information (big picture) for small features. There are some non-linear classification algorithms that are very similar to neural networks, including Support Vector Machines (SVM) that does not suffer from the above limitations. SVM separates the dataset into classes by building a high-dimensional hyperplane and the accuracy of classification highly depends on the parameters that describe hyperplane. SVM is a powerful classification tool and superior to ANN, especially if the size of the dataset is small.

67

### 3.3.6. Linear Discriminant Analysis (LDA)

Linear discriminant analysis (LDA) is a supervised method, which is also a probabilistic classifier; however, can be combined with regression model and PCA. In general, LDA is very similar to PCA and can be used as dimensionality reduction step, pattern recognition, and machine learning applications. The main goal of LDA is to project a k-dimensional original dataset on to a smaller n-dimensional subset (**n ≤ k−1**), while preserving the discriminatory information between classes in the dataset. The main difference between PCA and LDA is that LDA computes linear discriminants (the axes) that maximize the classification between multiple classes and the class labels are known. LDA generates the components from the original dataset in the form of two sets of matrices, namely, inter-class scatter matrix and intra-class scatter matrix. Each of these matrices has an eigenvalue, which indicates the significance and the magnitude of the variance in that component. The eigenvectors are sorted in a decreasing order and k eigenvectors with the most chemical information are chosen to form a $k \times d$ dimensional matrix **W**. Every column in a new matrix represents an eigenvector. Therefore, the transformed matrix **X** in the new subspace can be derived from matrix multiplication **X = W × Z**, where **Z** is an $n \times d$-dimensional matrix (representing **n** samples). Here, I provide the mathematical background of the Fisher's linear discriminant method applied to a two-class system. Assume that I have a set of K-dimensional samples $X = \{x^1, x^2, \ldots, x^m\}$. Then, the mean vector of two classes in X- space can be written as:

$$u_k = \frac{1}{N_k} \sum_{i \in C_k} x^i \ \text{ where } k = 1,2$$

and in the subspace y can be written as:

68

$$\widehat{u_k} = \frac{1}{N_k} \sum_{i \in C_k} y^i = \frac{1}{N_k} \sum_{i \in C_k} \theta^T x^i = \theta^T u_k \quad \text{where } k = 1,2$$

One can define the between-class variance by measuring the distance between the means in a projected space, as follows:

$$\hat{u}_2 - \hat{u}_1 = \theta^T (u_2 - u_1) \quad \text{where } k = 1,2$$

And within-class variance can be defined as:

$$\hat{s}_k^2 = \sum_{i \in C_k} \left( y^i - \hat{u}_k \right)^2 \quad \text{where } k = 1,2$$

To find the maximum between-class variance with regards to within-class variance, one can define an objective function as:

$$J(\theta) = \frac{(\hat{u}_2 - \hat{u}_1)^2}{\widehat{s_1}^2 + \widehat{s_2}^2}$$

Let's define the projection y as a function of the scatter matrix in x space:

$$\hat{s}_k^2 = \sum_{i \in C_k} \left( y^i - \hat{u}_k \right)^2$$

$$= \sum_{i \in C_k} \left( \theta^T x^i - \theta^T u_k \right)^2$$

$$= \sum_{i \in C_k} \theta^T \left( x^i - u_k \right) \left( x^i - u_k \right)^T \theta$$

$$= \theta^T S_k \theta$$

69

Where $S_k$ is the scatter in x space. Now, $J(\theta)$ can be re-written in terms of scatter matrices.

$$(\widehat{u_2}-\widehat{u_1})^2 = (\theta^T u_2 - \theta^T u_1)^2$$

$$= \theta^T (u_2 - u_1)(u_2 - u_1)^T \theta$$

$$= \theta^T S_B \theta$$

and

$$\widehat{s_1}^2 + \widehat{s_2}^2 = \theta^T S_1 \theta + \theta^T S_2 \theta$$

$$= \theta^T S_W \theta$$

Where $S_B$ represents between-class scatter matrix and $S_W$ represents within-class scatter matrix. Objective function that expresses the Fisher criterion can be expressed as:

$$J(\theta) = \frac{\theta^T S_B \theta}{\theta^T S_W \theta}$$

By maximizing the objective function $J(\theta)$ and finding an optimum $\theta$, one can derive the direction of $\theta$ for the projection of the data down to one dimension. This calculation can be extended to multiclass problem and instead of one projection; one can seek for (C-1) projections. Discriminant analysis has been widely used in vibrational spectroscopic methods including Raman and infrared applied to classification of various tissue types [57-60], cellular activity [61], microbial species [62], and food products [63,64]. Although discriminant analysis is a promising approach for robust classification of tissues and cells, an extensive pre-processing, which is mainly dimensionality reduction (often PCA, PLS regression models) is required. Some

70

groups have developed LDA-based algorithms [65] and the applications of these methods are gaining interest in spectroscopic data with the goal of classification between stages of disease.

### 3.3.7. Identifying the discriminatory features responsible for classification

Infrared spectrochemical imaging of biological samples involve spectral analysis and classify the spectra into separate classes and categories [66]. The interpretation of data typically involves two sets of information: clustering and the identification of variables that are responsible for the observed classification. PCA is a well-known technique for decomposing the original dataset into a linear combination of principal components, which is based on the assumption that variations imply information. One of the main drawbacks of performing PCA alone is that in most cases, it does not give the optimum classification between groups of samples. Additionally, using only one loadings vector to determine the chemistry attributed to the clustering, leads to losing chemical information. PCA followed by LDA is a combination method in which the original dataset first transforms via PCA and projects into a new subspace. Then, the transformed dataset in PC space are projected into a new subspace via LDA.

In this method, PCA is used as a pre-processing method to reduce the dimensionality of data and provides a priori information to load into LDA algorithm. Linear discriminants are found such that the ratio of between-class variance to within-class variance is maximized, and thus the maximum separation between classes is achievable. The second piece of information originated from PCA-LDA analysis is the "cluster vector plot" that can be used for biomarker extraction. The cluster vector plots are used to infer the components and the strength of components that correspond to the observed biomarkers of the disease. The largest peaks or troughs in vector

plots were associated with the most contributing feature to the separation between classes. Here, I present the matrix manipulations to derive the LDA scores matrix and cluster loadings matrix.

Consider $N$ samples that separate into $h$ clusters and the number of wavenumbers (variables) being $m$. The number of principal components that are preserved is $g$ and the number of LD coefficients from LDA analysis is denoted by $d$. For simplicity, let's assume 100 samples, 5 clusters, 650 wavenumbers, 8 PCs, and 4 LDs. The notations $i, j, k,$ and $w$ are used for individual samples, PCs, LD coefficients, and variables. PCA provides a $100 \times 8$ scores matrix $S_{Ng}$ and a $650 \times 8$ loadings matrix $L_{mg}$ and a vector with 1 column represents 5 classes in the sample $c_N$. LDA gives a $4 \times 8$ linear discriminant coefficient matrix $D_{dg}$ that can be used as weighting factors for the scores matrix from PCA. The $100 \times 4$ LDA scores matrix can be computed by the following matrix multiplication: $SD_{ikh} = \sum D_{kj} S_{ji}$.

Since LDA allows labeling the classes (types of tissues and cells); therefore, I can generate cluster loadings plot for each class. For each of the $h$ clusters, from $SD_{ikh}$ that is calculated from the previous step, a $4 \times 5$ mean cluster scores matrix $mD_{kh}$ is calculated. Then the $650 \times 4$ loadings matrix $LD_{wk} = \sum_j (D_{kj} L_{jw})$, and finally the $650 \times 5$ cluster loadings matrix is computed via $F_{mh} = \Sigma_h \sum_k (LD_{wk} mD_{kh})$. Every column in matrix $F_{mh}$ provides the loadings plot for each cluster. PCA-LDA results are likely to be more accurate when applied to two groups, since there is less contributing factors that play role in the spectral variations between different classes. Figure 3.8 demonstrates the classification between retinal tissues from non-diabetic and diabetic mice and an associated cluster vector plot, from PCA-LDA.
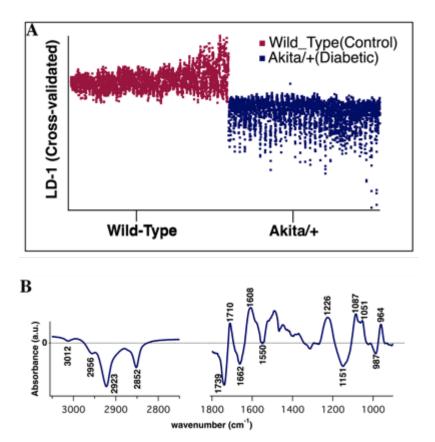
**Figure 3.8:** one-dimensional scores plot (A) and associated cluster vector plot (B) from PCA-LDA from the comparison between wild-type and diabetic retinal tissues.

## 3.4. Case Study: Classification of bacterial species

In this section I present the application of PCA-LDA in monitoring the photoreactivity of methicillin-resistant *Staphylococcus aureus* (MRSA) [67], a Gram-positive antibiotic resistant bacterium that leads to fatal infections, from infrared spectrochemical imaging data. In this example of the described method in section 3.4, to uncover the mechanism underlying the bactericidal effect of blue light, a combination of Fourier transform infrared (FTIR) spectroscopy and chemometric tools is employed to detect distinctive pathway of MRSA toward apoptosis after treatment. In this study, individual pixel spectra derived from hyperspectral cube of data, were generated and preprocessed as follows. $CO_2$ peak at 2350 cm$^{-1}$ was flattened between 2500

73

and 2200 cm$^{-1}$ and then baseline was corrected by finding a least squares linear line between all spectral points in 2692-1920 cm$^{-1}$ spectral region and subtracted from every spectrum. Then, signal to noise ratio (S/N) in every spectrum was systematically assessed by defining the noise content as the standard deviation in the 2000-1900 cm$^{-1}$ spectral region, and the signal as the maximum of the curve between 1700 and 1600 cm$^{-1}$ (Amide I band).

It is critical to ensure that all spectra are subjected to the same procedure for pre-processing such as baseline correction and de-noising. In classification algorithms based on supervised methods, the entire dataset is consisted of two independent subsets, namely, the training dataset and the test dataset. The training dataset is attributed to pre-defined classes and is used to learn the features and spectral characteristics. The test dataset is used to estimate how well the classifier has been trained and assists to validate the classification achieved from training dataset. Among the existing classification techniques that could be used in this study, PCA-LDA is chosen due to the fact that maximum potential separation and spectral features associated with each treatment could be achieved, which indicates the mechanism underlying each treatment applied to the bacterial cells.

Five different experimental groups of samples are evaluated using FTIR spectroscopy. Group I: Control I, comprised of untreated MRSA incubated at 37 °C for 24 h (N = 3); Group II: Control II, comprised of untreated MRSA incubated in ambient air for 24 h (N = 3); Group III: Irradiation with 262 J/cm$^2$ of blue 470 nm light, incubated at 37 °C for 24 h (N = 5); Group IV: UV light- irradiated (253.5 nm) MRSA, incubated at 37 °C for 24 h (N = 5); Group V: Vancomycin-treated MRSA, incubated at 37 °C for 24 h (N = 3). The rationale for control II is to determine if there would be a difference between bacteria left to die through a natural process (devoid of adequate growth environment) as opposed to treatment with chemicals and

74

irradiation. The designated selection of the three treatment groups is based on their effectiveness to inactivate MRSA, and to identify how they affect the biomarkers evaluated through FTIR.
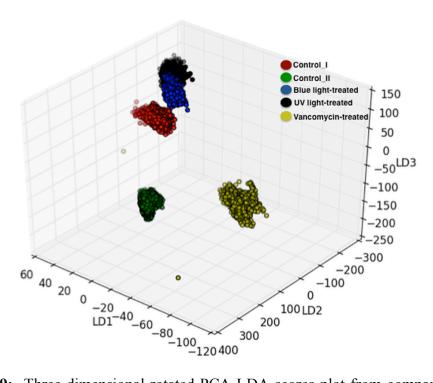


**Figure 3.9:** Three-dimensional rotated PCA-LDA scores plot from comparison of control I (red circles), control II (green circles), blue light irradiated (blue circles), UV light-irradiated (black circles) and vancomycin-treated spectra (yellow circles). Reprinted from [67].

Figure 3.9 shows rotated three-dimensional scores plot generated from PCA-LDA model, performed on the spectra from control and treated MRSA cells. Scores plot demonstrates that vancomycin-treated spectra are clearly separated along LD1 from the rest of the groups. Clustering and separation between control I, control II, blue light-irradiated, UV light-irradiated, and vancomycin-treated groups are achieved. Scores plot reveals that blue light- irradiated and UV light-irradiated spectra are the closest adjacent clusters and there is a small degree of overlap between the two groups. The UV light-irradiated spectra are the most biochemically similar to the blue light-irradiated spectra. In addition, the comparison between four groups (control groups

and light-irradiated (UV/blue light spectra) is performed to confirm that the separation is not due to the vancomycin-treated spectra and clear clustering between control groups and light-irradiated spectra (UV/blue-light) is achieved.

PCA-LDA analysis yields wavelength dependent loadings that describe the major wavenumbers responsible for classification between the classes. Since the goal of this analysis is to understand the mode of action of each treatment, the most informative loadings are those that are generated from the comparison between control groups and individual treatments. Nearly 70,000 spectra (4096 spectra per measurement; 6 measurement per sample and at least 3 replicates per sample) are pre-processed (baseline-corrected, de-noised, S/N tested, and vector-normalized) between 1800 and 900 cm$^{-1}$ for each group of samples prior to computational analysis.

Figure 3.10 shows the loading plot and two-dimensional scores plot from the comparison between control and vancomycin-treated spectra and highlight the important functional groups that are responsible for the clustering. Clear clusters of control I, control II and vancomycin-treated spectra are achieved. Significant wavenumbers responsible for this separation are observed at 1677 cm$^{-1}$ (amide I), 1652 cm$^{-1}$ (amide I), 1598 cm$^{-1}$ (amide II), 1230 cm$^{-1}$ ($v_{asym}$ $PO^{2-}$) and 1062 cm$^{-1}$ ($v$ C-O). The loading plot highlights additional wavenumbers that lie in the lipid region (1488 and 1409 cm$^{-1}$), and carbohydrate region (1155, 1027, 1014 cm$^{-1}$).
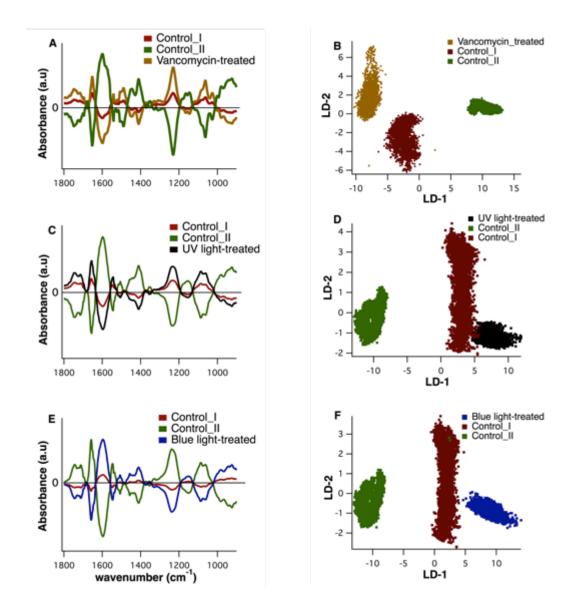
**Figure 3.10:** Cluster vector plots and corresponding 2D scores plot (LD2 vs. LD1) from PCA-LDA analysis. A,B) Comparison between control groups and vancomycin-treated spectra, C,D) Comparison between control groups and UV-light irradiated spectra, and E,F) Comparison between control groups and blue light-irradiated spectra. In PCA-LDA plots, red (control I), green (control II), blue (blue light irradiated), black (UV-light irradiated), and yellow (vancomycin- treated) colors are used. Reprinted from [67].

Figures 3.11 shows the loading plot and the corresponding scores plot from the comparison of control I, control II and light-irradiated (Blue light and UV light) spectra. Scores plot demonstrate a very good degree of clustering between control and light-irradiated spectra,

although, a small degree of overlap between UV light-irradiated and control I spectra is observed. Figure 3.11- Panels E and F show the loading plots derived from analyses where the spectra from UV light- irradiated and blue light- irradiated are compared with control I/II spectra. The loading plot for UV light and blue light irradiated MRSA are very similar overall; however, the frequencies of some absorbance bands between 1800 and 900 cm$^{-1}$ experience shifts. The common discriminating wavenumbers that are identified in blue light and UV light-irradiated loading plots are 1683, 1656, 1596, and 1542 cm$^{-1}$ (amide I and II), 1743 cm$^{-1}$ (C-O stretching, ester functional group in lipids and phospholipids), 1060 cm$^{-1}$ ($v$ C-O) and 1087 cm$^{-1}$ ($v_{sym}$ PO$_2^-$). The frequencies of some of the absorbance bands between 1800 and 900 cm$^{-1}$ are shifted, when the loadings for UV light and blue light irradiated spectra are compared. The distinct shifts are the basis of our interpretation of the differences among the interactions between UV and MRSA versus blue light and MRSA.

The most intense differentiating band between light-irradiated (blue light and UV light) and control spectra, in the DNA/RNA spectral region (1425–900 cm$^{-1}$), is the asymmetric stretching of phosphate moieties ($v_{asym}$ PO$_2^-$). $v_{asym}$ PO$_2^-$ band, a broad band from overlapping of two bands at 1225 cm$^{-1}$ (B-helical form of DNA) [38] and 1240 cm$^{-1}$ (A-helical form of nucleic acids) [68], clearly exhibits distinctive characteristics of UV light-irradiated (1228 cm$^{-1}$) and blue light-irradiated MRSA (1238 cm$^{-1}$). Moreover, the FTIR biomarkers at 970 cm$^{-1}$ (C-C stretching of DNA backbone) [68] and 1717 cm$^{-1}$ (base pair vibrations) [68] that are seen in the UV-irradiated loading plot, are observed at 965 cm$^{-1}$ and 1712 cm$^{-1}$ in the blue light-irradiated loading plot.
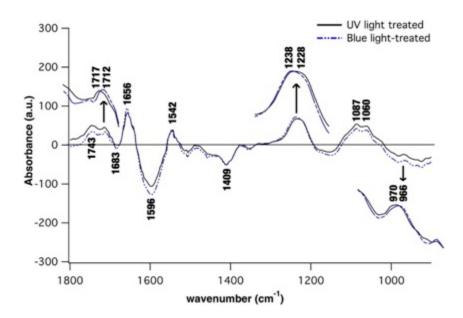
**Figure 3.11:** Cluster vector plots derived from the comparison of control groups *vs*. blue-light irradiated spectra (blue dashed line) and control groups *vs*. UV light-irradiated (black solid line) spectra are overlaid. The FTIR bands that are indicative of blue-light and UV light-induced damage to MRSA are highlighted. Clear shifts in the loadings plot from 966, 1238, 1712 cm$^{-1}$ (blue light-irradiated) to 970, 1228, 1717 cm$^{-1}$ (UV light-irradiated) are shown. Reprinted from [67].

I demonstrated that a combination of FTIR measurements and PCA-LDA detects the photoreactivity of MRSA and distinctive mechanism of action toward apoptosis per treatment. The distinct biomarkers of blue light irradiated, UV light-irradiated and vancomycin-treated samples are discussed. The observations suggest, for the first time, that irradiation with blue light targets A-DNA in MRSA cells, and the bacterial response is distinct from UV irradiation response that is known to target B-DNA. From the well-understood UV light response of MRSA I conclude that blue light irradiation of MRSA induces A-DNA cleavage and that the B-DNA is more resistant to damage. In sum, UV light and blue light use different stratagems to modify DNA, and the light treatments are complementary and distinct from the known antimicrobial effect of vancomycin against MRSA.

79

## 3.5. References

1. Pelletier, M.J. (2003). Quantitative analysis using Raman spectrometry. Applied Spectroscopy 57, 1, 20A-42A.

2. Kramer R. (1988) Chemometric Techniques for Quantitative Analysis, 1st ed. CRC Press.

3. Haaland, D.M., and Thomas, E.V. (1988). Partial least-squares methods for spectral analyses .1. relation to other quantitative calibration methods and the extraction of qualitative information. Analytical Chemistry 60, 1193-1202.

4. Andrew, J.J., and Hancewicz, T.M. (1998). Rapid analysis of Raman image data using two-way multivariate curve resolution. Applied Spectroscopy 52, 797-807.

5. De Juan, A., Maeder, M., Hancewicz, T., Duponchel, L., and Tauler, R. (2009). Chemometric tools for image analysis. Infrared and Raman spectroscopic imaging, 65–109.

6. Geladi, P. (2003). Chemometrics in spectroscopy. Part 1. Classical chemometrics. Spectrochimica Acta Part B-Atomic Spectroscopy 58, 767-782.

7. Byrne, H.J., Knief, P., Keating, M.E., and Bonnier, F. (2016). Spectral pre and post processing for infrared and Raman spectroscopy of biological tissues and cells. Chemical Society Reviews 45, 1865-1878.

8. Jirasek, A., Schulze, G., Yu, M.M.L., Blades, M.W., and Turner, R.F.B. (2004). Accuracy and precision of manual baseline determination. Applied Spectroscopy 58, 1488-1499.

9. Leger, M.N., and Ryder, A.G. (2006). Comparison of derivative preprocessing and automated polynomial baseline correction method for classification and quantification of narcotics in solid mixtures. Applied Spectroscopy 60, 182-193.

10.  Naes, T., Isaksson, T. , Fearn, T., Davies, T. ( 2002 ). A user Friendly guide to Multivariate Calibration and Classification. NIR Publications , Chichester, UK.

11. Eriksson, L., Hagberg, P., Johansson, E., Rannar, S., Whelehan O., Astrom, A., Lindgren, T. (2001). Multivariate process monitoring of a newsprint mill. Application to modeling and predicting cod load resulting from deinking of recycled paper. J. Chemometr 15, 337–352.

12. Trevisan, J., Angelov, P.P., Patel, II, Najand, G.M., Cheung, K.T., Llabjani, V., Pollock, H.M., Bruce, S.W., Pant, K., Carmichael, P.L.*, et al.* (2010). Syrian hamster embryo (SHE) assay (pH 6.7) coupled with infrared spectroscopy and chemometrics towards toxicological assessment. Analyst 135, 3266-3272.

13. Tahtouh, M., Despland, P., Shimmon, R., Kalman, J.R., and Reedy, B.J. (2007). The application of infrared chemical imaging to the detection and enhancement of latent fingerprints: Method optimization and further findings. Journal of Forensic Sciences 52, 1089-1096.

14.Bassan, P., Byrne, H.J., Bonnier, F., Lee, J., Dumas, P., and Gardner, P. (2009). Resonant Mie scattering in infrared spectroscopy of biological materials - understanding the 'dispersion artefact'. Analyst 134, 1586-1593.

15. Bassan, P., Kohler, A., Martens, H., Lee, J., Byrne, H.J., Dumas, P., Gazi, E., Brown, M., Clarke, N., and Gardner, P. (2010). Resonant Mie Scattering (RMieS) correction of infrared spectra from highly scattering biological samples. Analyst 135, 268-277.

16. Bassan, P., Kohler, A., Martens, H., Lee, J., Jackson, E., Lockyer, N., Dumas, P., Brown, M., Clarke, N., and Gardner, P. (2010). RMieS-EMSC correction for infrared spectra of biological cells: Extension using full Mie theory and GPU computing. Journal of Biophotonics 3, 609-620.

17. Eilers, P.H.C. (2004). Parametric time warping. Analytical Chemistry 76, 404-411.

18. Lieber, C. and Mahadevan-Jansen, A. (2003). Automated Method for Subtraction of Fluorescence from Biological Raman Spectra. Appl. Spectrosc 57, 1363-1367.

19. Ehrentreich, F. and Sümmchen, L. (2001). Spike Removal and Denoising of Raman Spectra by Wavelet Transform Methods. Analytical Chemistry 73 (17), 4364-4373.

20. Wold , S. (1975 ) Soft -modeling by latent variables: the non - linear iterative partial least squares (NIPALS) algorithm , in Perspectives in Probability and Statistics (ed. J. Garni), Academic Press , London , 117 – 42.

21. Hill, W and Rogalla, D. (1992). Spike-correction of weak signals from chargecoupled devices and its application to raman spectroscopy," Analytical Chemistry, 64 (21), 2575-2581.

22. Behrend, C.J., Tarnowski, C.P., and Morris, M.D. (2002). Identification of outliers in hyperspectral Raman image data by nearest neighbor comparison. Applied Spectroscopy 56, 1458-1461.

23. Katsumoto, Y., and Ozaki, Y. (2003). Practical algorithm for reducing convex spike noises on a spectrum. Applied Spectroscopy 57, 317-322.

24. Baker, M.J., Trevisan, J., Bassan, P., Bhargava, R., Butler, H.J., Dorling, K.M., Fielden, P.R., Fogarty, S.W., Fullwood, N.J., Heys, K.A*., et al.* (2014). Using Fourier transform IR spectroscopy to analyze biological materials. Nature Protocols 9, 1771-1791.

25. Van de Hulst, H.C. (1981). Light scattering by small particles, Dover Publications, Mineola, NY.

26. Kohler, A., Sul e-Suso, J., Sockalingum, G.D., Tobin, M., Bahrami, F., Yang, Y., et al. (2008). Estimating and correcting Mie scattering in synchrotron-based microscopic Fourier transform infrared spectra by extended multiplicative signal correction. Applied Spectroscopy. 62, 259–266.

27. Mattson, E.C., Unger, M., Clede, S., Lambert, F., Policar, C., Imtiaz, A., D'Souza, R., and Hirschmugl, C.J. (2013b). Toward optimal spatial and spectral quality in widefield infrared spectromicroscopy of IR labelled single cells. Analyst 138
, 5610-5618.

28. Deinum, G., Rodriguez, D., Romer, T.J., Fitzmaurice, M., Kramer, J.R., and Feld, M.S. (1999). Histological classification of Raman spectra of human coronary artery atherosclerosis using principal component analysis. Applied Spectroscopy 53, 938-942.

29. Shimoyama, M., Maeda, H., Matsukawa, K., Inoue, H., Ninomiya, T., and Ozaki, Y. (1997). Discrimination of ethylene vinyl acetate copolymers with different composition and prediction of the vinyl acetate content in the copolymers using Fourier-transform Raman spectroscopy and multivariate data analysis. Vibrational Spectroscopy 14, 253-259.

30. Keen, I.P., White, G.W., and Fredericks, P.M. (1998). Characterization of fibers by Raman microprobe spectroscopy. Journal of Forensic Sciences 43, 82-89.

31. Ryder, A.G. (2002). Classification of narcotics in solid mixtures using Principal Component Analysis and Raman spectroscopy. Journal of Forensic Sciences 47, 275-284.

32. Krafft, C., Knetschke, T., Siegner, A., Funk, R.H.W., and Salzer, R. (2003). Mapping of single cells by near infrared Raman microspectroscopy. Vibrational Spectroscopy 32, 75-83.

33. Krishna, C.M., Sockalingum, G.D., Bhat, R.A., Venteo, L., Kushtagi, P., Pluot, M., and Manfait, M. (2007). FTIR and Raman microspectroscopy of normal, benign, and malignant formalin-fixed ovarian tissues. Analytical and Bioanalytical Chemistry 387, 1649-1656.

34. Notingher, L., Jell, G., Notingher, P.L., Bisson, I., Tsigkou, O., Polak, J.M., Stevens, M.M., and Hench, L.L. (2005). Multivariate analysis of Raman spectra for in vitro non-invasive studies of living cells. Journal of Molecular Structure 744, 179-185.

35. Shih, W.C., Bechtel, K.L., and Feld, M.S. (2007). Constrained regularization: Hybrid method for multivariate calibration. Analytical Chemistry 79, 234-239.

36. Alsberg, B.K., Woodward, A.M., Kell, D.B. (1997). An introduction to wavelet transforms for chemometricians: A time frequency approach. Chemometrics and Intelligent Laboratory Systems 37, 2, 215-239.

37. Xu, R and Wunsch, D. (2008). Clustering. Wiley-IEEE Press, ISBN: 978-0-470-27680-8.

38. Heise, H.M. (2008). Biomedical Vibrational Spectroscopy – Technical Advances, in: Lasch, P. and Kneipp, J. (eds.), Biomedical Vibrational Spectroscopy (Wiley, Hoboken), 9 – 37.

39. Maquelin, K., Kirschner, C., Choo-Smith, L.P., Van den Braak, N., Endtz, H.P., Naumann, D., Puppels, G.J. (2002). Identification of medically relevant microorganisms by vibrational spectroscopy, Journal of Microbiological Methods 51, 3, 255-271.

40. Daniel, P., Picart, P., Bendriaa, L., Sockalingum, G. D., Adt, I., Charrier, T., Durand, M. J., Ergan, F., Manfait, M., and Thouand, G. (2008). Effect of toxic organotin compounds on bacteria investigated by micro-Raman spectroscopy. Spectrosc. Lett. 41:19-28.

41. Shanmukh, S., Jones, L., Driskell, J., Zhao, Y. P., Dluhy, R., Tripp, R. A. (2006). Rapid and sensitive detection of respiratory virus molecular signatures using a silver nanorod array SERS substrate. Nano Lett. 6, 2630–2636.

42. Peeters, J.P., and Martinelli, J.A. (1989). Hierarchical cluster-analysis as a tool to manage variation in germplasm collections. Theoretical and Applied Genetics 78, 42-48.

43 De Veij, M., Deneckere, A., Vandenabeele, P., De Kaste, D., Moens, L. (2008). Detection of counterfeit Viagra1 with Raman spectroscopy. Journal of Pharmaceutical and Biomedical Analysis 46 (2), 303–309.

44. Selim, S.Z. and Ismail, M.A. (1984). K-Means-Type Algorithms: A Generalized Convergence Theorem and Characterization of Local Optimality. IEEE Transactions on Pattern Analysis and Machine Intelligence PAMI-6, 1, 81-87.

45. Jain, A.K. and Dubes, R.C. (1988). Algorithms for Clustering Data, first printing ed. Prentice Hall.

46. Jain, A.K. (2010). Data clustering: 50 years beyond K-means. Pattern Recognition Letters 31, 651-666.

47. Berger, J.O. (1985). Statistical decision theory and Bayesian analysis, 2nd ed. New York: Springer-Verlag.

48. Duda, R.O, Stork, D.G., Hart, P.E. (2001). Pattern classification. New York; Chichester: Wiley.

49. Goodacre, R., Timmins, E.M., Burton, R., Kaderbhai, N., Woodward, A.M., Kell, D.B., and Rooney, P.J. (1998). Rapid identification of urinary tract infection bacteria using hyperspectral whole-organism fingerprinting and artificial neural networks. Microbiology-Uk 144, 1157-1170.

50. Maquelin, K., Kirschner, C., Choo-Smith, L.P., et al. (2003). Prospective study of the performance of vibrational spectroscopies for rapid identification of bacterial and fungal pathogens recovered from blood cultures. J Clin Microbiol 41, 324–29.

51. Lasch, P., Haensch, W., Naumann, D., & Diem, M. (2004). Imaging of colorectal adenocarcinoma using FT-IR microspectroscopy and cluster analysis. *Biochimica Et Biophysica Acta-Molecular Basis of Disease, 1688*(2), 176-186.

52. Khalil, O.S. (1999). Spectroscopic and clinical aspects of noninvasive glucose measurements. Clinical Chemistry 45, 165-177.

53. Santos, V.O., Oliveira, F.C.C., Lima, D.G., Petry, A.C., Garcia, E., Suarez, P.A.Z., and Rubim, J.C. (2005). A comparative study of diesel analysis by FTIR, FTNIR and FT-Raman spectroscopy using PLS and artificial neural network analysis. Analytica Chimica Acta 547, 188-196.

54. Usenius, J.P., Tuohimetsa, S., Vainio, P., AlaKorpela, M., Hiltunen, Y., and Kauppinen, R.A. (1996). Automated classification of human brain tumours by neural network analysis using in vivo H-1 magnetic resonance spectroscopic metabolite phenotypes. Neuroreport 7, 1597-1600.

55. Duarte, I.F., Barros, A., Almeida, C., Spraul, M., and Gil, A.M. (2004). Multivariate analysis of NMR and FTIR data as a potential tool for the quality control of beer. Journal of Agricultural and Food Chemistry 52, 1031-1038.

56. Gniadecka, M., Philipsen, P.A., Sigurdsson, S., Wessel, S., Nielsen, O.F., Christensen, D.H., Hercogova, J., Rossen, K., Thomsen, H.K., Gniadecki, R., *et al.* (2004). Melanoma diagnosis by Raman spectroscopy and neural networks: Structure alterations in proteins and lipids in intact cancer tissue. Journal of Investigative Dermatology 122, 443-449.

57. Crow, P., Barrass, B., Kendall, C., Hart-Prieto, M., Wright, M., Persad, R., and Stone, N. (2005). The use of Raman spectroscopy to differentiate between different prostatic adenocarcinoma cell lines. British Journal of Cancer 92, 2166-2170.

58. Stone, N., Kendall, C., Shepherd, N., Crow, P., and Barr, H. (2002). Near-infrared Raman spectroscopy for the classification of epithelial pre-cancers and cancers. Journal of Raman Spectroscopy 33, 564-573.

59. Gazi, E., Baker, M., Dwyer, J., Lockyer, N.P., Gardner, P., Shanks, J.H., Reeve, R.S., Hart, C.A., Clarke, N.W., and Brown, M.D. (2006). A correlation of FTIR spectra derived from prostate cancer biopsies with Gleason grade and tumour stage. European Urology 50, 750-761.
60. Koljenovic, S., Choo-Smith, L.P., Schut, T.C.B., Kros, J.M., van den Berge, H.J., and Puppels, G.J. (2002). Discriminating vital tumor from necrotic tissue in human glioblastoma tissue samples by Raman spectroscopy. Laboratory Investigation 82, 1265-1277.

61. Chen, L., Carpita, N. C., Reiter, W.-D., Wilson, R. H., Jeffries, C. and McCann, M. C. (1998), A rapid method to screen for cell-wall mutants using discriminant analysis of Fourier transform infrared spectra. The Plant Journal, 16: 385–392.

62. Kim, S., Kim, H., Reuhs, B.L., and Mauer, L.J. (2006). Differentiation of outer membrane proteins from Salmonella enterica serotypes using Fourier transform infrared spectroscopy and chemometrics. Letters in Applied Microbiology 42, 229-234.

63. Chen, Q.S., Zhao, J.W., Fang, C.H., and Wang, D.M. (2007). Feasibility study on identification of green, black and Oolong teas using near-infrared reflectance spectroscopy based on support vector machine (SVM). Spectrochimica Acta Part a-Molecular and Biomolecular Spectroscopy 66, 568-574.

64. Zagonel, G.F., Peralta-Zamora, P., and Ramos, L.P. (2004). Multivariate monitoring of soybean oil ethanolysis by FTIR. Talanta 63, 1021-1025.

65. Walsh, M.J., Singh, M.N., Stringfellow, H.F., Pollock, H.M., Hammiche, A., Grude, O., Fullwood, N.J., Pitt, M.A., Martin-Hirsch, P.L., and Martin, F.L. (2007b). FTIR microspectroscopy coupled with two-class discrimination segregates markers responsible for inter- and intra-category variance in exfoliative cervical cytology. Mutagenesis 22, 453-453.

66. Walsh, M.J., Singh, M.N., Pollock, H.M., Cooper, L.J., German, M.J., Stringfellow, H.F., Fullwood, N.J., Paraskevaidis, E., Martin-Hirsch, P.L., and Martin, F.L. (2007a). ATR microspectroscopy with multivariate analysis segregates grades of exfoliative cervical cytology. Biochemical and Biophysical Research Communications 352, 213-219.

67. Bumah, V.V., Aboualizadeh, E., Masson-Meyers, D.S., Eells, J.T., Enwemeka, C.S., and Hirschmugl, C.J. (2017). Spectrally resolved infrared microscopy and chemometric tools to reveal the interaction between blue light (470 nm) and methicillin-resistant Staphylococcus aureus. Journal of Photochemistry and Photobiology B-Biology 167, 150-157.

68. Whelan, D.R., Bambery, K.R., Heraud, P., Tobin, M.J., Diem, M., McNaughton, D., and Wood, B.R. (2011). Monitoring the reversible B to A-like transition of DNA in eukaryotic cells using Fourier transform infrared spectroscopy. Nucleic Acids Research 39, 5439-5448.

**Chapter 4: Diabetic Retinopathy**

**4.1 Introduction**

Diabetic retinopathy (DR) is a microvascular retinal dysfunction, known as a major vision threatening complication of diabetes in the working age population in the developed world [1,2]. Almost half of this group will go on to develop some degrees of diabetic retinopathy in their lifetime. In the West, DR, a progressive disease affecting the integrity and function of retinal circulation, is the leading cause of blindness in adults aged 20-74 years. It affects over 5.3 million people in the U.S., making up to 8% of all cases of legal blindness and 12% of newly diagnosed blindness [3]. It is increasing as a major cause of blindness in other parts of the world, especially developing countries. It is known that diabetes damages the blood vessels in the retina, which leads to blood and fluid leakage into the retina. Accumulation of fluids in the eye causes the change in the curvature of the lens; therefore, exacerbate the focusing and eventually leads to blurred vision over time. DR has multiple stages and each stage develop ophthalmic complications. In the initial stage of DR, which is known as background retinopathy, patients are more asymptomatic, and microaneurysms that are tiny black swellings appear in the blood vessels in the retina, which leads to blood leakage. The next state is non-proliferative retinopathy that includes the presence of serious histopathological symptoms such as bleeding into the retina. The final stage is proliferative retinopathy in which abnormal blood vessels develop scar tissues that could lead to retina detachment and loss of vision.

To date, vitrectomy, which is a surgical procedure to remove scar tissue and abnormal blood vessels, is a common practice for DR and in the most advanced proliferative DR, retinotomies and retinectomies will be applied that are extreme surgical procedures. The reason for cutting the retina (retinotomy) and remove peripheral retinal tissue and nonessential areas (retinotomies) is

87

to have access to sub-retinal tissue and treat retinal incarceration. However, these methods are invasive methods with serious consequences and only recommended when all less invasive methods failed. In some other cases, vitreous tissue is the preferred tissue to sample when there is a suspicious case of intraocular malignancy or when infection is suspected. Maintaining the level of HbA1c and glucose in the normal range can substantially reduce the risks of severe DR and still known as one of the most important aspects in the management of DR.

## 4.2 Retinal anatomy

Retina is the innermost layer of the eye, which is approximately 300-400 micrometer thick and lines the back of the eye. The practical constituents of retina are arranged in form of the layers [4] and vertically oriented from the outside to inside as follows: (1) Retinal Pigment Epithelium (RPE) (2) inner segment of photoreceptor, (3) The outer segment of photoreceptor (4) The nucleus segment of photoreceptor (outer nucleus layer) (5) outer plexiform layer (6) inner nucleus layer (7) inner plexiform layer (8) ganglion cell layer. There are three major types of neurons distributed across the retina from the front of the eye (ganglion cells) to the middle section (amacrine horizontal cells) and the innermost in the retina (photoreceptors) [5]. Ganglion cell axons that are present in the optic nerve transmit signals to the brain. The ganglion cell layer is the innermost layer in the retina and entails displaced cells and ganglion cells. Photoreceptor layer is the outermost layer in the retina and contains rods and cones. Photoreceptor cells are responsible for converting the absorbed light into an electric signal and ultimately to the brain through optic nerve. Rods are more sensitive to light and allows for night vision, while cones adapts for daylight vision and responsible for seeing visual details and colors [6].
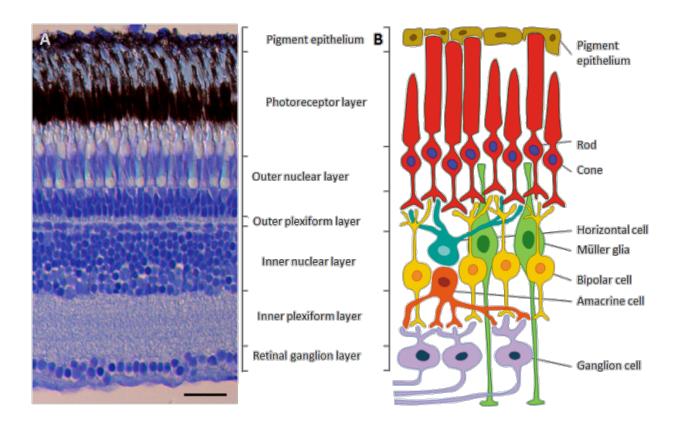
**Figure 4.1:** A) A histologic cross-section of retina highlighting the microstructure of retina. B) Schematic illustration of retinal layers and the cells attributed to each layer. Reprinted with permission from [7].

The inner segment of photoreceptor system is rich in poly-unsaturated fatty acid (PUFA) that is the main target for oxidative attack during diabetes [8]. Inner plexiform layer and outer plexiform layer are two neuropils in the retina that are not occupied by cell bodies but contain intricate dendrites and synapsis. The outer plexiform layer is an adjacent layer to the outer nuclear layer in photoreceptor system and the inner plexiform layer is attached to the inner nuclear layer and ganglion cell layer. The outer plexiform layer bridges the connection between rods and cones, bipolar cells, and horizontal cells; however, the inner plexiform layer connects the bipolar cells to the ganglion cells. A cross-section diagram of retinal structure is demonstrated in Figure 4.1.

### 4.3 Diagnostic modalities in Diabetic Retinopathy

Comprehensive eye exam is still the highly recommended way to monitor the progression of DR. There are several exams that help ophthalmologists to evaluate different parts of the eye including eye chart exam to determine visual acuity, slit-lamp exam that examines the front parts of the eye  (cornea, lens, sclera), and dilated exam that widen or dilate the pupil to examine the retina and optic nerve. Another factor is the consistent monitoring of blood glucose levels. Excessive blood glucose could lead to an elevated eye's focusing power and eventually blurred vision. In this section, some routine modalities to assess DR, including Optical Coherence Tomography (O.C.T), Fluorescein Angiography (FA), and Ultrasonography will be discussed.

### 4.3.1. Optical Coherence Tomography (O.C.T)

Optical Coherence Tomography (OCT) [9,10] is an emerging technology and non-invasive method that permits cross-sectional imaging of tissues on the micron scale. OCT unlike histopathological diagnostic methods that requires removal of tissues can provide real time images of tissues. OCT was initially used in imaging of the eye [11-15] and has had the largest impact in the field of ophthalmology. OCT provides the high-resolution images of cross section of retina that is typically used for evaluating the thickness of retina. The principals of imaging by means of OCT technology relies on measuring the echo time delay of the reflected light using interferometry. Low coherence interferometry has been initially used in ophthalmology to measure the corneal thickness [16,17]. Low coherence interferometry is based on a Michelson type interferometer and measures the echo time delay by comparing the backscattered light to a light with known reference path and time delay. The beam of light from a source is guided onto a beam splitter, where one of the beams is directed onto the sample and the other beam travels in the direction of a reference path with a variable time delay and path length. The backscattered

90

light from the sample and the reflected light from the reference path are combined and detected by the detector outside the interferometer. In the presence of a coherent source of light, the interference patterns occur as the pathlength of light varies; however, the interference patterns from short-pulse or low-coherence light sources only occur when the pathlength difference matches the coherence length of light. The optical beam is incident on the sample, and then the echo time delay and the backscattering intensity are measured and used to generate an axial backscattering profile. Next, the incident beam is focused into the sample in the transverse direction and the axial backscattering intensity is measured at different spots to generate a two-dimensional image. Therefore, the resultant image represents the optical backscattering through the cross-section of a sample. Schematics of the two-dimensional image from OCT and backscattering intensity as a function of depth are shown in Figure 4.2. The axial resolution in OCT imaging is dependent on the coherence length of the source and is inversely proportional to the bandwidth of the source. The axial resolution in OCT is defined as follows:

$$\Delta z = (2\ln2/\pi)(\lambda^2/\Delta\lambda)$$

Where $\Delta\lambda$ is the full width at half maximum (FWHM) of the bandwidth of the source.
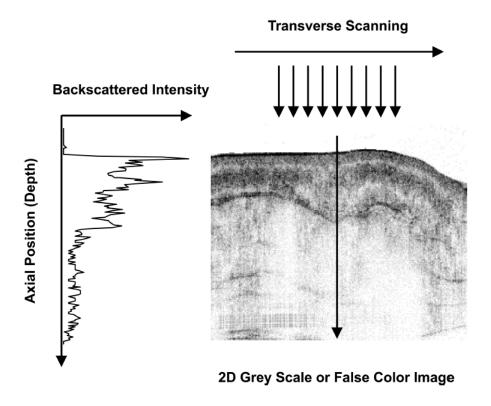
**Figure 4.2:** Cross-sectional images from measurements of echo time delay of light at multiple transverse positions are reconstructed. Backscattered intensity associated with cross-sectional plane of the tissue is shown. The image can be displayed in either gray scale or false color scale. Reprinted with permission from [10].

The spatial resolution in OCT imaging is defined very similar to conventional microscopy systems depending on the numerical aperture of the objective lens and the focused spot size and it is given as follows:

$$\Delta x = (4\lambda/\pi)(f/d)$$

Where $f$ is the focal length of the objective and $d$ is the spot size on the objective lens. By using high numerical aperture objectives and focusing on a small area, one can achieve high spatial resolution. Additionally, the spatial resolution depends on the depth of focus, which is given by:

$$b = \pi \, \Delta x^2 / 2\lambda$$

In practice, Forsterite laser and short pulse lasers have been used that permits high-resolution imaging and high-speed data acquisition, due to the high-energy throughput of the lasers. Short pulse laser sources at wavelengths near 1300 nm (power ranges between 10 and 15 mW) provide $\approx 15$ μm axial resolution [18].
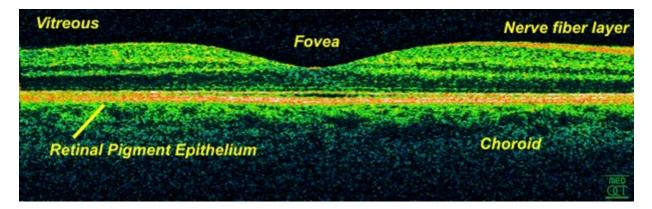


**Figure 4.3:** OCT image of the human retina from in vivo measurements, highlighting the structural morphology of the retinal tissue. The highly backscattering retinal layers (Retinal pigment epithelium and Nerve fiber layer) appear red in the false-color images. Reprinted with permission from [10].

OCT has had the largest impact in the field of visual science and in particular, in retinal-related studies. Figure 4.3 demonstrates a human retina imaged with OCT and provides a cross-sectional view of the retina tissue with detailed structures. This image highlights different layers of the retina including the retinal pigment epithelium and choroid layer as well as photoreceptor layer; however, because OCT measure absolute positions at a resolution of $\approx 10$μm, the motion of the eye in the measurement time interval (1-2 seconds) can influence the images. OCT has been widely used in detecting retinal-related diseases including glaucoma, macular edema,

macular degeneration and choroidal tumors [19-24]. OCT is a promising diagnostic tool to determine the progress of diabetic retinopathy by providing quantitative information such as the thickness of the retina and dynamic responses of the retina.

### 4.3.2. Fluorescein Angiography

Fluorescein Angiography (FA) [25] is an eye examination tool that involves imaging the choroidal and retinal circulations using dye-tracing method. It is a diagnostic procedure that helps to understand the pathological processes in the retina and diagnose an assembly of retinal diseases. The dye that has been used in this technique is a sodium fluorescein (a yellow-red dye) that has absorption in the range of blue light (460-490 nm) and excitation in the range of yellow-green (520-530 nm). In the normal angiogram, the appearance of the dye helps ophthalmologists to examine the abnormalities of the eye because the retinal pigment epithelium and blood vessels in the retina act as barriers to the fluorescein leakage in a normal retina. Fluorescein dye is injected intravenously (antecubital vein of the arm) and after 8-12 seconds dye appears in the optic nerve and choroid and a couple of seconds later, the retinal circulation appear. Monitoring the transition of the dye and sequence of photographs captured by a fundus camera, which is equipped with excitation and barrier filters, yields an angiogram. Fundus camera permits illumination of retina with white light that has been passed through the blue excitation filter and then the fluorescein molecules absorb blue light, emitting light with a longer wavelength (yellow-green). The barrier filter blocks any reflections from light that allows camera to produce high contrast images.

To interpret the angiogram, it is critical to understand multiple phases of FA starting from the first appearance of dye in the choroid, which occurs 10 seconds after injection. This process is called choroidal flush and the capillaries within choroid leaks fluorescein dye into the

www.manaraa.com

extravascular space. The next phase is the filling phase of retinal capillaries with dye, which starts from filling the walls of the larger veins and becomes wider until the maximum vessel fluorescence occurring. The last phase is the gradual reduction of dye intensity and elimination of dye from retina and choroid, which occurs approximately 15 minutes after injection. Despite the valuable diagnostic role of FA in retinal and choroidal complication including diabetic retinopathy, macular degeneration, and choroidal tumors, it is an invasive method that can lead to complications and adverse reactions [26]. Some adverse reactions have been reported in 10-15 % of patients such as nausea, urticarial, hypotension, seizures, and pruritis. However, the characteristic features of FA in identifying neovascularization and elevated vascular permeability make it a promising technique to diagnose vascular complications during diabetic retinopathy.

### 4.3.3. Ultrasonography

Ultrasonography [27] is a technique that has been initially used in ocular diagnosis and it is based on propagation, reflection, and attenuation of sound waves. At the interface of two acoustic media, the difference between velocities yields an echo. The sound echoes from the tissue are recorded and displayed as an image. To create an image via ultrasonography, the ultrasound scanner determines the strength of the echoes and the time lapse that takes for the echo to be received. The strength of the echo determined the brightness of an image. The frequency of ultrasound is positively correlated with resolution of ultrasound imaging and negatively correlated with depth of penetration. Higher frequency sound waves are able of scattering or reflecting from tiny structures; however, these waves are limited in penetrating deep tissues due to a larger attenuation coefficient. This technique is available in two forms. A-scan (time-amplitude) permits rapid examination and differentiation of intraocular and orbital lesions

95

and B-scan (based on amplitude of a two-dimensional cross section of a tissue) allows anatomical visualization similar to an eye section, which is critical for interpretation.

Ultrasonography is an important non-invasive diagnostic tool in detecting severe retinal complications including tumors, retinal detachments, and hemorrhages. The main drawbacks of sonography-based techniques are the limitation in penetrating deep tissues, bones, and environments when gas is present between transducer and organ (e.g. gastrointestinal tract). This technique is highly dependent on the quality of the expertise of an operator in order to produce high quality images.

## 4.4. Diabetic Retinopathy

Diabetic retinopathy (DR) is a complication of diabetes that affects retinal blood vessels and bleeding of the blood vessels. In the early stages, DR has no direct impact on vision but the sight will be affected as disease progresses. There are two major stages of DR, namely non-proliferative diabetic retinopathy (NPDR) and proliferative diabetic retinopathy (PDR). The classification is based on morphological changes observed in the retina, retinal abnormalities, blurred vision, and progressive visual loss.

### 4.4.1. Non-proliferative Diabetic Retinopathy

Non-proliferative diabetic retinopathy (NDPR) or background retinopathy is the early stage of retinopathy and is characterized by blood vessels that develop swellings (balloon-like) called microaneurysms, basement membrane thickening, and altered retinal vascular permeability [28]. Microaneurysms can be located only on one side of the vessel wall or both sides and its size ranges between 25 and 100 micrometer. Sometimes in the early stages of NPDR, no

www.manaraa.com

histopathological symptoms exist; however, advances in fluorescein angiography enabled a better detection of microaneurysms. NPDR is categorized into three different levels of severity namely, mild, moderate, and severe. One of the factors to determine the severity of NPDR is the presence of intraretinal hemorrhages that are caused by ruptured microaneurysms. These hemorrhages are typically located in the inner nuclear layer, and the plexiform layers in the retina [29]. Another microscopic findings of NPDR are hard exudates (intraretinal lipids), cotton wools (accumulation of cytoplasmic debris and damage to nerve fiber layer), and venous beading (fluctuation of the venous caliber). Based on the American Academy of Ophthalmology, classification between different stages of NPDR and associated findings in each stage has been documented. Mild NPDR is defined based on the presence of only one microaneurysm. Moderate stage is defined by the presence of cotton wools, hard exudates, and mild hemorrhages. Severe stage is defined by the presence of more than 20 hemorrhages, venous beading in two or more spots in the retina, and at least one microvascular abnormalities [30]; however, there is no symptom of proliferative diabetic retinopathy. This classification is an invaluable standard in determining the severity of DR and prevents the progress of the disease into more hostile stages; however, the mechanism behind the damage within the retina and the progress of diabetic retinopathy remains unclear.

### 4.4.2. Proliferative Diabetic Retinopathy

Proliferative diabetic retinopathy (PDR) is an abnormal growth of blood vessels on the surface of retina and the main cause of blindness. PDR is a progressed form of retinopathy that occurs when blood vessels leak in the large area inside the retina and make visual acuity worse [30,31]. During this process, retina develops new blood vessels (neovascularization); however, the new blood vessels are abnormal (leaking) i.e. accompanied by scar tissue and not capable of

providing enough blood into the retina [31]. The growth of abnormal vessels in the retina is caused by vascular endothelial growth factor (VEGF), which is a proangiogenic signal for formation of new blood vessels to restore oxygen supply to tissues when the blood circulation is not sufficient. However, overproduction of VEGF [32] contributes to the disease and cause vascular complications in the retina. These abnormal blood vessels sometimes cause displacing retina from its normal position and eventually retinal detachment. In severe cases when major parts of retina are detached, vision loss occurs. Another vision effect of PDR is called vitreous hemorrhage, which is bleeding of new blood vessels into the vitreous (central part of the eye) and blocks the rays of lights reaching the retina [33]. The main symptom of vitreous hemorrhage is the appearance of tiny dots floating in the field of vision. The severe case of PDR may lead to neovascular glaucoma [34], which is the case when the front segment neovascularization (involving iris -the colored part of the eye) is presented along with a formation of a fibrovascular membrane. Consequently, the new blood vessels blocks the flow of fluids out of the eye that leads to accumulation of pressure in the eye and eventually damage to the optic nerve.

## 4.5. Oxidative Stress pathway in diabetic retinopathy

Oxidative stress contributes the most into the pathogenesis of diabetic retinopathy and the structural, and biochemical alterations in the retina are highly related to oxidative stress [35,36]. Understanding the exact mechanism behind biochemical alterations associated with oxidative stress offers potential early therapeutic targets to assist developing early diagnosis and treatment of diabetic retinopathy. Metabolic processes consume 95% of the oxygen that enters the mitochondrial electron transport chain through normal physiological conditions and the rest is reduced to reactive oxygen species (ROS). However, there are additional physiological procedures that lead to continuous production and removal of ROS and support the functionality

of the cells. Any imbalance between production and scavenging of ROS can lead to serious complications such as elevated oxidative stress, disturbance in cellular homeostasis, and damages to macromolecules (e.g. DNA, proteins, and carbohydrates).

Diabetes results in elevated oxidative stress, which can modulate cellular functions by stimulating signal transduction pathways, and promotes the progression of neuropathy [37], retinopathy [38], nephropathy [39,40], and myocardial injury [41]. Among major recognized pathophysiological pathways that describe the mechanism underlying diabetic retinopathy, the oxidative stress pathway is known as a unifying mechanism that links the existing pathways. Most of these pathways originate from hyperglycemia, which is mainly induced by activation of oxidative stress; however, the exact mechanism that oxidative stress contributes to development of diabetic retinopathy remains a challenge. Mitochondria are another endogenous source of superoxide and ROS that play a pivotal role in the oxidative damage during diabetes [42-44]. Mitochondrial DNA is very susceptible to oxidative damage and the damage to mitochondria leads to an imbalance of ROS in the electron transport chains and eventually damage to proteins in the membrane [45]. On the other hand, elevated ROS cause mitochondria to release cytochrome c that give rise to apoptosis [46]. Therefore, mitochondria have a dual role in the development of diabetes by contribution to the oxidative damage and susceptibility to the oxidative stress and cell death.

Structural and functional changes in the microvasculature of retina are another consequence of the oxidative damage. Structural changes such as membrane thickening [47-50], microvascular cell loss [51], and capillary closures [52] are examples of the pathways toward diabetes that are impacted by ROS. Basement membrane thickening is an early structural alteration in the retina that results from cross linking of advanced glycated end (AGE) products

99

and collagens. Breakdown of blood-retinal barrier [53] is another functional alteration that plays a critical role in the pathogenesis of diabetic retinopathy, in which the change occurs in the permeability of retinal endothelial cells and the barrier becomes more leaky. Apoptosis of neuroretina that occurs at the early stages of diabetes is gaining interest; however, more studies are needed to determine biochemical alterations in the retinal cells and the role of individual cells and layers in the pathogenesis of diabetic retinopathy.

Although the development of histopathology of diabetic retinopathy takes over 10 years, the damages to neuronal units of retina, especially cells with fragmented DNA occur early. Therefore, apoptosis of cells in the retina during the early phase of diabetes-induced damage, which is followed by late structural consequences, are critical. In conclusion, the path to fully understand the mechanistic insight is expected from studies on animal models that provide some hints as to the effectiveness of clinical outcomes; however, more studies are still in need.

## 4.6. References

1. Mohamed, Q., Gillies, M.C., Wong, T.Y. (2007). Management of diabetic retinopathy: a systematic review. J. Am. Med. Assoc. 298 , 902-916.

2. Marshall, S.M. & Flyvbjerg, A. (2006). Prevention and early detection of vascular complications of diabetes. British Med. J. 333, 475-480.

3. Aiello, L.P., Gardner, T.W., King, G.L., et al. (1998). Diabetic retinopathy. Diabetes Care 21, 143-156.

4. Masland, R.H. (2001). The fundamental plan of the retina. Nat. Neurosci. 4, 877-886.

5. Cuthbertson, R.A., Mandel, T.E. (1986). Anatomy of the mouse retina. Endothelial cellpericyte ratio and capillary distribution. Invest Ophthalmol. Visual Sci. 27, 1659–1664.

6. Carter-Dawson, L.D., Lavail, M.M. (1979). Rods and cones in the mouse retina. I. Structural analysis using light and electron microscopy. J. Comp. Neur. 188, 245–262.

7. Gramage, E., Li, J. and Hitchcock, P. (2014), The expression and function of midkine in the vertebrate retina. Br J Pharmacol, 171: 913–923. doi:10.1111/bph.12495.

8. Suh, M., Wierzbicki, A.A., Clandinin, M.T. (2002). Dietary n-3 FA modulate long and very long chain FA content, rhodopsin content and rhodopsin phosphorylation in rat rod outer segment after light exposure. Lipids 37, 253–260.

9. Baumal, C.R. (1999). Clinical applications of optical coherence tomography. Curr. Opin. Ophthalmol. 10, 182-188.

10. Fujimoto, J. G., Pitris, C., Boppart, S. A., & Brezinski, M. E. (2000). Optical Coherence Tomography: An Emerging Technology for Biomedical Imaging and Optical Biopsy. *Neoplasia (New York, N.Y.)*, *2* (1-2), 9–25.

11. Swanson, E.A., Izatt, J.A., Hee, M.R., Huang, D., Lin, C.P., Schuman, J.S., Puliafito, C.A., Fujimoto, J.G. (1993). In vivo retinal imaging by optical coherence tomography. Opt Lett. 18, 1864–1866.

12. Izatt, J.A., Hee, M.R., Swanson, E.A., Lin, C.P., Huang, D., Schuman, J.S., Puliafito, C.A., Fujimoto, J.G. (1994). Micrometer-scale resolution imaging of the anterior eye in vivo with optical coherence tomography. Arch Ophthalmol. 112, 1584–1589.

13. Hee, M.R., Izatt, J.A., Swanson, E.A., Huang, D., Schuman, J.S., Lin, C.P., Puliafito C.A., Fujimoto, J.G. (1995). Optical coherence tomography of the human retina. Arch Ophthalmol. 113, 325–332.

14. Puliafito, C.A., Hee, M.R., Lin, C.P., Reichel, E., Schuman, J.S., Duker, J.S., Izatt, J.A., Swanson, E.A., Fujimoto, J.G. (1995). Imaging of macular diseases with optical coherence tomography. Ophthalmology. 102, 217–229.

15. Puliafito, C.A., Hee, M.R., Schuman, J.S., Fujimoto, J.G. (1996). Optical Coherence Tomography of Ocular Diseases. Thorofare, NJ: Slack Inc.

16. Fercher, A.F., Mengedoht, K., Werner, W. (1988). Eye-length measurement by interferometry with partially coherent light. Opt Lett. 13, 1867–1869.

17. Huang, D., Wang, J., Lin, C.P., Puliafito, C.A., Fujimoto, J.G. (1991). Micron-resolution ranging of cornea and anterior chamber by optical reflectometry. Lasers Surg Med. 11, 419–425.

18. Bouma, B.E., Tearney, G.J., Bilinsky, I.P., Golubovic, B. (1996). Self phase modulated Kerr-lens mode locked Cr:forsterite laser source for optical coherent tomography. Opt Lett. 21, 1839–1841.

19. Hee, M.R., Puliafito, C.A., Wong, C., Duker, J.S., Reichel, E., Schuman, J.S., Swanson, E.A., Fujimoto, J.G. (1995). Optical coherence tomography of macular holes. Ophthalmology. 102, 748–756.

20. Hee, M.R., Puliafito, C.A., Wong, C., Reichel, E., Duker, J.S., Schuman, J.S., Swanson, E.A., Fujimoto, J.G. (1995). Optical coherence tomography of central serous chorioretinopathy. Am J Ophthalmol. 120:65–74.

21. Hee, M.R., Baumal, C.R., Puliafito, C.A., Duker, J.S., Reichel, E., Wilkins, J.R., Coker, J.G., Schuman, J.S., Swanson, E.A., Fujimoto, J.G. (1996). Optical coherence tomography of age-related macular degeneration and choroidal neovascularization. Ophthalmology. 103, 1260–1270.

22. Krivoy, D., Gentile, R., Liebmann, J.M., Stegman, Z., Walsh, J.B., Ritch, R. (1996). Imaging congenital optic disc pits and associated maculopathy using optical coherence tomography. Arch Ophthalmol. 114, 165–170.

23. Lincoff, H., Kreissig, I. (1998). Optical coherence tomography of pneumatic displacement of optic disc pit aculopathy. Br J Ophthalmol. 82, 367–372.

24. Schaudig, U., Hassenstein, A., Bernd, A., Walter, A., Richard, G. (1998). Limitations of imaging choroidal tumors in vivo by optical coherence tomography. Graefe's Arch Clin Exp Ophthalmol. 236, 588–592.

25. Delori, F., Ben-Sira, I., Trempe, C. (1976). Fluorescein angiography with an optimized filter combination. Am. J. Ophthalmol. 82 , 559-66.

26. Kwan, A.S., Barry, C., McAllister, I.L., Constable, I. (2006). Fluorescein angiography and adverse drug reactions revisited: the Lions Eye experience. Clin. Experiment Ophthalmol. 34, 33- 38.

27. DiBernardo, C.W., Schachat, A.P., Fekrat, S. (1998). Ophthalmic Ultrasound: A Diagnostic Atlas. Thieme 1, 3-45.

28. Kern, T. S. (2007). Contributions of Inflammatory Processes to the Development of the Early Stages of Diabetic Retinopathy. *Experimental Diabetes Research, 2007*, 95103.

29. Wong Li Yun, U. Rajendra Acharya, Y.V. Venkatesh, Caroline Chee, Lim Choo Min, E.Y.K. Ng. (2008). Identification of different stages of diabetic retinopathy using retinal optical images, Information Sciences 178(1,2), 106-121.

30. Wilkinson, C.P. (2002). Achieving consensus on an international clinical classification for diabetic retinopathy. Program and abstracts of the American Academy of Ophthalmology 2002 Annual Meeting, Orlando,FL, 20–23.

31. Davis DM. Proliferative diabetic retinopathy. (1994). In: Ryan SJ (ed). *Retina*. The CV Mosby Company: St Louis, 1319–1360.

32. Wiedemann, P. (1992). Growth factors in retinal diseases: Proliferative vitreoretinopathy, proliferative diabetic retinopathy and retinal degeneration. *Surv Ophthalmol* 36, 373–384.

33. Demircan, N., Safran, B., Soylu, M., Ozcan, A.A., Sizmaz, S. (2006). Determination of vitreous interleukin-1 (IL-1) and tumour necrosis factor (TNF) levels in proliferative diabetic retinopathy. Eye 20, 1366–69.

34. Antonia, M., Joussena, B., Neil S., Carien, N. (2007). Diabetic Retinopathy. Dev. Ophthalmol. 39, 1-12.

35. Baynes, J. W., & Thorpe, S. R. (1999). Role of oxidative stress in diabetic complications - A new perspective on an old paradigm. *Diabetes, 48*(1), 1-9.

36. Kowluru, R. A., & Chan, P.S. (2007). Oxidative Stress and Diabetic Retinopathy. *Experimental Diabetes Research*.

37. Feldman, E. L. (2003). Oxidative stress and diabetic neuropathy: a new understanding of an old problem. *Journal of Clinical Investigation*, *111*(4), 431–433.

38. Kowluru, R.A. (2003). Effect of reinstitution of good glycemic control on retinal oxidative stress and nitrative stress in diabetic rats. *Diabetes* 52: 818–823.

39. Ha, H., and Kim, K.H. (1999). Pathogenesis of diabetic nephropathy: the role of oxidative stress and protein kinase C. Diabetes Research and Clinical Practice, 45 (2,3), 147–151.

40. Hinokio, Y., Suzuki, S., Hirai, M., Suzuki, C., Suzuki, M., Toyota, T. (2002). Urinary excretion of 8-oxo-7, 8-dihydro-2 - deoxyguanosine as a predictor of the development of diabetic nephropathy. Diabetologia, 45 (6), 877–882.

41. Cai, L. and Kang, Y.L. (2001). Oxidative stress and diabetic cardiomyopathy: a brief review," Cardiovascular Toxicology, 1 (3), 181–193.

42. Kanwar, M., Chan, P.S., Kern, T.S., Kowluru, R.A. (2007). Oxidative damage in the retinal mitochondria of diabetic mice: possible protection by superoxide dismutase. Invest. Ophthalmol. Vis. Sci. 48(8), 3805-3811.

43. Kowluru, R.A., Atasi, L., Ho, Y.S. (2006). Role of mitochondrial superoxide dismutase in the development of diabetic retinopathy. Investigative Ophthalmology & Visual Science, 47 (4), 1594–1599.

44. Kowluru, R.A., Kowluru, V., Xiong, Y., Ho, Y.S. (2006). Overexpression of mitochondrial superoxide dismutase in mice protects the retina from diabetes-induced oxidative stress. Free Radical Biology and Medicine, 41(8), 1191–1196.

45. Maassen, J.A., 'T Hart, L.M., Van Essen, E., et al. (2004). Mitochondrial diabetes: molecular mechanisms and clinical presentation," Diabetes 53, supplement 1, S103–S109.

46. Kowluru, R.A., and Abbas, S.N. (2003). Diabetes-induced mitochondrial dysfunction in the retina. Investigative Ophthalmology & Visual Science, 44 (12), 5327–5334.

47. Kern, T.S., & Engerman, R.L. (1996). A mouse model of diabetic retinopathy. Archives of Ophthalmology, 114 (8), 986–990.

48. Joussen, A.M., Poulaki, V., Le, M.L., et al. (2004). A central role for inflammation in the pathogenesis of diabetic retinopathy. FASEB Journal, 18 (12), 1450–1452.

49. Joussen, A.M., Doehmen, S., Le, M.L., et al. (2009). TNF-$\alpha$ mediated apoptosis plays an important role in the development of early diabetic retinopathy and long-term histopathological alterations. Molecular Vision 15, 1418–1428.

50. Ferris, F.L. III. & Patz, A. (1984). Macular edema: a complication of diabetic retinopathy. Surv. Ophthalmol. 28 (suppl.), 452-461.

51. Barber, A. J., Lieth, E., Khin, S. A., Antonetti, D. A., Buchanan, A. G., & Gardner, T. W. (1998). Neural apoptosis in the retina during experimental and human diabetes. Early onset and effect of insulin. *Journal of Clinical Investigation*, *102*(4), 783–791.

52. Schröder, S., Palinski, W., & Schmid-Schönbein, G. W. (1991). Activated monocytes and granulocytes, capillary nonperfusion, and neovascularization in diabetic retinopathy. *The American Journal of Pathology*, *139*(1), 81–100.

53. Murata, T, Nakagawa, K, Khalil, A, Ishibashi, T, Inomata, H, Sueishi, K. (1996) The relation between expression of vascular endothelial growth factor and breakdown of the blood-retinal barrier in diabetic rat retinas *Lab Invest* 74,819-825.

**Chapter 5: Retinal oxidative stress at the onset of diabetes**

Diabetic retinopathy is a microvascular complication of diabetes that can lead to blindness. In the present study, I aimed to determine the nature of diabetes-induced, highly localized biochemical changes in the neuroretina at the onset of diabetes. High-resolution synchrotron Fourier transform infrared (s-FTIR) wide field microscopy coupled with multivariate analysis (PCA-LDA) was employed to identify biomarkers of diabetic retinopathy with spatial resolution at the cellular level. I compared retinal tissue prepared from 6-week-old Ins2$^{Akita/+}$ heterozygous (Akita/+, N=6; a model of diabetes) male mice compared with the wild-type (WT; control, N=6) mice. Male Akita/+ mice become diabetic at 4-weeks of age. Significant differences ($P<0.001$) in the presence of biomarkers associated with diabetes and segregation of spectra was achieved. Differentiating IR bands attributed to nucleic acids (964, 1051, 1087, 1226 and 1710 cm$^{-1}$), proteins (1662, 1608 cm$^{-1}$) and fatty acids (2854, 2923, 2956 and 3012 cm$^{-1}$) were observed between the Akita/+ and WT samples. Comparison between distinct layers of the retina, namely the photoreceptor layer (PRL), outer plexiform layer (OPL), inner nuclear layer (INL) and inner plexiform layer (IPL) suggested that the photoreceptor layer is the most susceptible layer to the oxidative stress in short-term diabetes. Spatially-resolved chemical images indicated heterogeneities and oxidative-stress induced alterations in the diabetic retina morphology compared with WT retina. The spectral biomarkers and the spatial biochemical alterations in the diabetic retina and in specific layers were identified for the first time. I believe that the conclusions drawn from these studies will help to bridge the gap in our understanding of the molecular and cellular mechanisms that contribute to pathobiology of diabetic retinopathy.

## 5.1. Introduction

Diabetic retinopathy (DR), a progressive disease affecting the integrity and function of retinal circulation, is the leading cause of blindness in adults [1]. Development of DR can stimulate the growth of scar tissue and elevate the intraocular pressure. It is well established that neurovascular retinal changes occur during diabetes [2]. However, the biochemical nature of these changes and their consequences on retinal function remain largely unknown. It has been acknowledged that oxidative stress and pro-inflammatory changes make significant contribution to the pathogenesis of DR in animal models [3]. Reactive oxygen species (ROS) are constantly produced during normal oxidative metabolism and are removed by scavenging system. Inefficient removal of ROS leads to excessive ROS and increased oxidative stress. Diabetes results in elevated oxidative stress that mainly damages biological macromolecules [4]. However, mechanisms behind the contribution of oxidative stress to development of diabetes still remains a challenge. Retina is the most susceptible tissue to the oxidative stress due to high content of polyunsaturated fatty acids (PUFAs). Membrane lipid peroxidation and oxidative damage to DNA are known as the consequences of increased level of ROS and superoxide in the diabetic retina [5,6].

Although DR is a slow progressing disease, it has been shown in animal models that in the initial stages (before any histopathological signs appear), the basement membrane of the capillaries thicken [7]. Diabetes affects neuronal cells in the retina, which causes visual dysfunction and degeneration of some neurons. Recently, the impacts of DR on neuronal unit of retina and the biochemical alterations including oxidative stress, apoptosis of neurons, and activation of microglial cells have been reported [8]. During diabetes, apoptosis of neurons occurs earlier than vascular cell apoptosis. It is critical to localize diabetes-induced damage and

108

determine the origin of neurons that experience apoptosis. Therefore, I aimed to determine the underlying biochemical changes in the neuroretina at early stages of diabetes.

Biological and biomedical applications of FTIR spectromicroscopy with the goal of classification, pattern recognition and pathology are highly sought after [9-13]. FTIR spectromicroscopy has been widely used in studying the pathology of various diseases including brain tumors [14], adenocarcinoma [15,16], prostate and breast cancer [17-21], lung cancer [22], lymph node [23], squamous cervical epithelium [24], or the biochemistry of neurons [25-27], antral oocytes [28] and stem cells [29]. Vibrational spectroscopic methods have been used in several studies to understand the diabetes-induced biochemical alterations in the kidney plasma membrane [30], liver microsomal membrane and soleus skeletal muscle [31], myocardia and vessels of the rat heart [32], human lips [33], and human saliva [34]. Thus, the use of appropriate imaging techniques to characterize biomolecular alterations attributed to DR is essential.

The aim of this study was to gain a deeper insight into the biochemical alterations in diabetic retina tissue by means of high-resolution chemically and spatially resolved FTIR images and chemometric tools. Chemical images from retinal tissue (flash-frozen samples) and the biochemistry of distinctive retinal layers have been previously studied [35]. Here, diabetic (Akita/+) and wild-type (WT) retina tissues, which were imaged at the mid-infrared IRENI beamline at the Synchrotron Radiation Center (SRC), were studied to determine short-term diabetes-induced alterations in the retina tissue at subcellular levels for the first time. Principal component analysis followed by linear discriminant analysis (PCA-LDA) was performed to achieve the maximum classification between Akita/+ and WT retina, and reveal the spectral biomarkers attributed to the distinction between these tissues [36]. For the first time, distinctive

109

layers of retina were compared to detect highly localized diabetes-induced biochemical changes in the retina. Comparison between the retinal photoreceptor layer (PRL), outer plexiform layer (OPL), inner nuclear layer (INL) and inner plexiform layer (IPL) in this study suggested that photoreceptors are the primary target for oxidative stress during short-term diabetes.

## 5.2. Materials and Methods

### 5.2.1. Animals

All experiments were carried out in accordance with the Association for Research in Vision and Ophthalmology Statement for the Use of Animals in Ophthalmic and Vision Research and were approved by the Institutional Animal Care and Use Committee of the University of Wisconsin School of Medicine and Public Health. Male Akita/+ mice spontaneously develop diabetes at 4-weeks of age due to a mutation in their insulin gene. The Akita spontaneous mutation (commonly referred to as MODY; Maturity-Onset Diabetes of the Young) is an autosomal dominant mutation in the insulin II gene (Ins2) 22. Ins2 $^{Akita}$-C57BL/6 diabetic mice develop retinal vascular pathology characteristic of the early stages of DR. Eyes were harvested from male WT and Akita/+ (all on C57BL/6 background) mice at 6-weeks of age. Eyes were immediately frozen in isopentane cooled to almost freezing in liquid nitrogen and later stored at -80°C freezer for FTIR microspectroscopy. Freezing must be done quickly in order to preserve the tissue integrity and avoid $H_2O$ crystal formation in the tissue. Each group of samples contained 6 mice.

### 5.2.2. Retinal tissue preparation

Frozen eyes that were preserved at -80° C were transported to the biotechnology facility (University of Wisconsin-Milwaukee) for sectioning using a cryostat machine (Leica Model CM

110

3050S) for rapid sectioning. It was critical to assure that the temperature at which the tissue was cut (inside cryostat) was between -15 °C and -20 °C and the blade was pre-chilled for at least half an hour prior to sectioniong.  Eyes were embedded in optimal cutting medium (O.C.T) compound (Sakura Finetek Inc. USA) and an embedded eye was left inside the cryostat machine (-20°C) for a minute (until the O.C.T will freeze and turn into a solid white color) prior to sectioning. Only small amount of O.C.T was applied to prevent tissue contamination. Eyes were dissected starting from the optic nerve (from back of the eye) and retinas were extracted using a thin paintbrush. The position of the eye was adjusted to be near the blade and the appropriate thickness was chosen (5-8 μm for FTIR measurements). At least, 5 retina tsections were collected from each animal and the tissues were mounted on mid-IR $BaF_2$ window. The $BaF_2$ window was placed in a foil-wrapped cell suspension tube (visible-light exposure is not allowed) and preserved on dried ice for transporting to the laboratory for FTIR measurements. Prior to FTIR imaging, the samples were desiccated in  dark at the room temperature, and low humidity condition [37, 38]. The cryosections are light sensitive, therefore exposure to visible light is only required during instrument setup. Schematic of the methodology is shown in Figure 5.1.
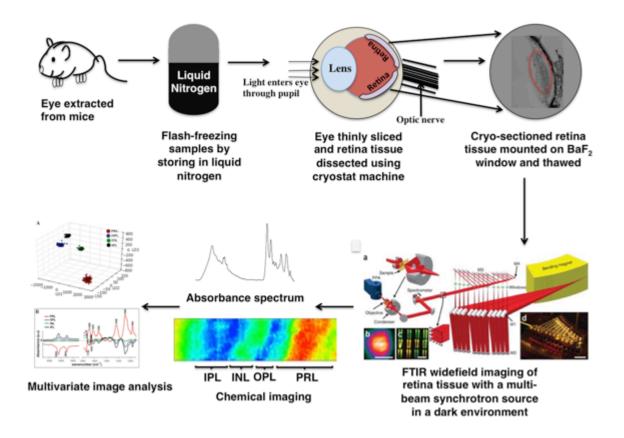
**Figure 5.1:** Schematics of the experimental design (Aboualizadeh et al., 10.1039/C6AN02603F).

### 5.2.3. Synchrotron FTIR wide-field microscopy

Advantages of the synchrotron-based FTIR imaging of the biological tissues have been previously described in several studies [39-45]. Here the samples were evaluated with a Bruker Vertex 70 IR spectrometer and a Bruker Hyperion 3000 IR Microscope equipped with a multi-beam synchrotron source at IRENI beamline [46,47]. The focal plane array (FPA) detector was a multi-element detector (128 × 128 pixels) coupled with an interferometer for collecting hyperspectral data sets (x, y, Abs (λ)). The measurements were performed using a 74× Cassegrain microscope objective (numerical aperture 0.65) and a 15× condenser aperture (N.A. 0.4). With this experimental geometry, the effective geometric pixel size at the sample plane was

112

0.54 × 0.54 μm$^2$ [46]. The data were collected using a 128 co-added scan at 4 cm$^{-1}$ spectral resolution. Data were acquired using OPUS 6.5 software (Bruker). FTIR measurements of retina sections were performed in a transmission mode. Background was measured from no sample area on BaF$_2$ window and the ratio of sample measurement to background was evaluated as an absorption spectrum. The FPA size for the measurements were set to 64×64 pixels, therefore, 4096 individual spectra in the mid-IR wavelength range 3800-900cm$^{-1}$ (every pixel contains an IR spectrum) were collected per single tile measurement. To cover a larger area of the tissue, 9 adjacent tiles were measured by mapping across the section of retina.

### 5.2.4. Data Pre-processing

Resultant spectra from tissues were partially influenced by Mie scattering. It is known that the IR radiation can scatter from particles with diameters in the range of 2-20 μm, and this artefact distorts the absorption bands leading to misinterpretation of the spectra [48-50]. Although the dispersion artefact appears as a derivative shape in the spectral region close to the Amide I band, this phenomenon could influence other peaks in the biochemical-IR region, and leads to misinterpretation of the peaks and pathology. In this study, nearly 192,000 individual pixel spectra (6 animals; each retina tissue measurement ≈32000 spectra) from WT tissues (including all retinal layers) and the same number of spectra from Akita/+ tissues (including all retinal layers) were generated and preprocessed as follows. CO$_2$ peak at 2350 cm$^{-1}$ was removed, and the spectral regions 900-1800 cm$^{-1}$ and 2750-3050 cm$^{-1}$ were used. This resulted in 624 data points for multivariate analysis. Pixel binning (2×2; average of 4 pixels) was applied. This was necessary to increase signal to noise ratio, and S/N in every spectrum was then systematically evaluated using an in-house written code in Matlab. To remove Mie scattering effect and dispersion artefacts, RMieS-EMSC correction was applied to the data. The algorithm used for

scattering correction in this work was implemented using Graphics Processing Units (GPUs) for fast hyperspectral processing, and described elsewhere [51-53]. All spectra were vector-normalized using Matlab prior to computational analysis.

### 5.2.5. Computational and statistical analysis

Multivariate analysis PCA-LDA was performed (in-house written code in Python) to reveal the biomarkers and segregation between diabetic and control groups. Principal component analysis (PCA) is an unsupervised method to decompose a dataset into bilinear latent variables called principal components (PCs). This reduces the dimensionality of the data while retaining most of the information in the data set. PCA is calculated based on the maximum variance contained in the dataset in descending order of importance, and there is a null correlation between components. The advantage of working with scores and loading representations is the reduced size of the big data and the efficacy to highlight and visualize the variations and heterogeneities in biological tissues. Linear discriminant analysis (LDA) is a supervised method to improve the segregation level and reveal clusters that are maximized based on the separation between multiple classes rather than variations within each group. Here PCA was used in the first stage and the optimum numbers of PCs were retained for subsequent LDA analysis (PCA-LDA), and cross-validated scores [54] were shown. The second piece of information originated from PCA-LDA analysis is the "cluster vector plot" that can be used for biomarker extraction. The cluster vector plots are used to infer the components and the strength of components that correspond to the observed biomarkers of the disease. The largest peaks or troughs in vector plots were associated with the most contributing feature to separation between classes [30]. Multivariate analysis was performed using "R" package (version 3.1.2), Matlab_R2016a and Python_2.6 version.

One-way-ANOVA statistical analysis was employed to determine whether there is any significant difference in the bands that are highlighted in both the WT and the Akita/+ samples. Results were studied as means ± standard deviations (S.D.) and P values, equal or less than 0.05, were accepted as a significant level of difference between the groups. The statistical analysis was performed using SAS 8.0. software.

## 5.3. Results

The central premise of this study was to identify chemical signatures of retinal damage, and to gain a deeper insight into retinal biochemical changes associated with early stages of diabetes. This study was motivated by two specific aims: *i)* identifying and characterizing the biomarkers of mitochondrial oxidative damage and cellular lipids; and *ii)* understanding diabetes-induced alterations in biochemistry of distinctive retinal layers by means of spatially-resolved chemical images.

### 5.3.1. IR spectra and chemical images of retinas from WT and diabetic (Akita/+) mice

Absorption spectra of retina from Akita/+ mice compared with retinas from WT mice are demonstrated in the mid-IR spectral range (3600-900cm$^{-1}$) in Figure 5.2. There are subtle differences in the biochemical-fingerprint spectral region (1800-900 cm$^{-1}$) and unsaturated and saturated fatty acid regions (3050-2800cm$^{-1}$). Second derivative absorption spectra (Savitzky-Golay algorithm, 9 smoothing points) are shown in the spectral region 3050-2800 cm$^{-1}$ associated with $\delta_{sym,asym}$(CH$_2$, CH$_3$) and polyunsaturated fatty acids (PUFA) content, 1800-1470 cm$^{-1}$ attributed to the secondary structure of proteins and 1470-900cm$^{-1}$ mostly attributed to DNA/RNA bands. Absorption bands in the spectral region 1160-950 cm$^{-1}$ are highly dominated by vibrations from C-O functional groups in carbohydrates, although $\nu_{symm}$ PO$^{2-}$ modes also contribute at 1085 ($\pm$2) cm$^{-1}$. Figure 5.2, B-D demonstrates the peak wavenumber values for

important macromolecules of retinas from WT and Akita/+ mice, respectively. The band assignments are summarized in Table 5.1.
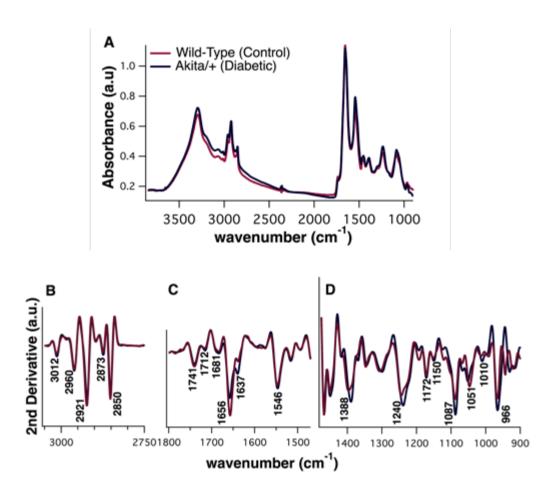


**Figure 5.2:** FTIR absorption spectrum analysis. A) Average spectra from the wild-type (WT) and Akita/+ retina tissues in the spectral range 3600-900cm$^{-1}$ are shown. Second derivative absorption spectra of the WT *vs*. Akita/+ tissue is shown B) in the lipid region 3050-2750cm$^{-1}$, C) protein region 1800-1500cm$^{-1}$ and D) DNA/RNA region 1425-900cm$^{-1}$. Spectra were generated from the whole retina tissue (including all retinal layers) and an average of 32,000 individual pixel spectra is demonstrated. (Aboualizadeh et al., 10.1039/C6AN02603F).

| Peak Frequency ($cm^{-1}$) | Assignments |
|---|---|
| **966** | Symmetric $PO_4^-$ stretching (DNA) and deoxyribose- phosphate skeletal motions |
| **1010** | C-O stretching; C-C stretching; DNA ribose |
| **1051** | C–O stretching: deoxyribose/ribose DNA, RNA/ glycogen |
| **1087** | Symmetric stretching of $PO_2^-$ :phospholipids and nucleic acids |
| **1150** | C-O, C-C stretching, C-O-H, C-O-C deformation of carbohydrates/ glycogen |
| **1172** | CO-O-C asymmetric stretching: ester bonds in cholesterol esters |
| **1240** | Asymmetric stretching of $PO_2^-$ :phospholipids and nucleic acids |
| **1388** | Symmetric $CH_3$ bending lipids, proteins, and nucleic acids |
| **1546** | Amide II- α helical structure of proteins (mainly N-H bending and C-N stretching) |
| **1637** | Amide I- β sheets |
| **1656** | Amide I- α helical or unordered structure of proteins (proteins C-O stretching, C-N stretch, CCN deformation) |
| **1681** | Amide I- β sheets, antiparallel/random coil (mainly C-O stretching) |
| **1712** | Base pair carbonyl (C=O), nucleic acids, DNA, RNA, oxidation of cellular lipids, short chain aldehyde |
| **1741** | C=O stretching: ester in phospholipids |
| **2850** | Symmetric stretching of $CH_2$; lipids |

117

| | |
|---|---|
| **2873** | Symmetric stretching of $CH_3$; lipids |
| **2921** | Asymmetric stretching of $CH_2$; lipids |
| **2960** | Asymmetric stretching of $CH_3$; lipids |
| **3012** | Olefinic=C-H stretching; unsaturated fatty acids |

Table 5.1. Band assignments for the retina spectra [55-59]

Chemical images demonstrated features of the mouse retina and its individual layers at subcellular level. Figure 5.3 depicts retina sections from WT and the Akita/+ mice. Figure 5.3A shows the photomicrograph of the retina oriented vertically from the choroid layer (the outermost layer of retina) to the ganglion cell layer, and the FTIR images are overlaid to visualize retinal layers with respect to the visible images. Figures 5.3B,C show the chemical images of the retina from WT and Akita/+ mice integrated underneath 1712 cm$^{-1}$ peak (baselined region: 1725-1700 cm$^{-1}$), and reveals the photoreceptor layer (PRL), outer plexiform layer (OPL), inner nuclear layer (INL) and inner plexiform layer (IPL) within the retina.

Chemical image of the retina from Akita/+ mice (Fig. 5.3C) is overlaid with the sketch of photoreceptor system including rod cells, mitochondria, and nucleus. Processed images of the retina at different frequencies and absorption spectra for the retina layers are discussed elsewhere [35]. In Figure 5.3 (red-blue color scale), regions of the highest absorption strength e.g. photoreceptor nucleus layer appeared red and the retinal layers with the lowest absorption strength were blue/purple. The same color scale was used for demonstration of both mosaics in each tissue. The H&E stained (after FTIR measurements) section of retina that highlights the nucleus segment of the photoreceptor layer has been shown elsewhere [35]. The outer segment

of photoreceptors are mostly comprised of rod cells and are rich in PUFA content, while the rod inner segments are rich in mitochondria and Golgi apparatus. Comparison between photoreceptor nucleus layers in both tissues revealed decreased concentration of DNA and more heterogeneity in retinas from Akita/+ mice compared with WT mice. As discussed previously [35], the outer and inner plexiform layers are rich in symmetric and asymmetric stretching of $CH_2$ and $CH_3$ functional groups, and the nucleus segment in photoreceptors (ONL) has very similar spectrum to INL. Chemical images in Figure 5.3 demonstrate the area of $128 \times 270$ μm$^2$ of the retinas from the Akita/+ and WT mice.

119
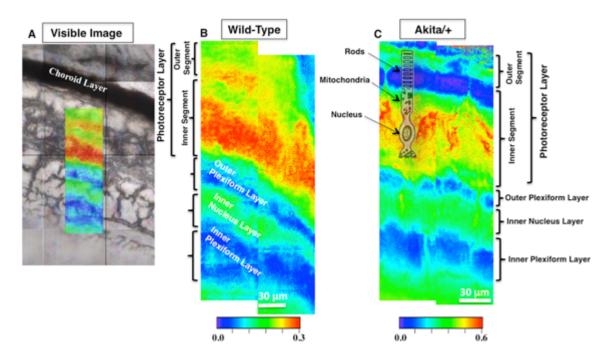
**Figure 5.3:** A) Photomicrograph of retina tissue with an overlaid FTIR image with localization of retinal layers. B, C) Chemical images of the WT and Akita/+ retina highlighting distinctive layers of retina. Each tissue covers the area of ≈128×270 μm² (2 mosaics, 2 × 8 tiles (each tile = 64×64 pixels)), and integrated over the nucleic acid band at 1712 cm⁻¹ (the linear baseline is set at 1700-1725 cm⁻¹) to highlight the absorption strength of this band in retinal layers. The inner, outer and nucleus segments of the photoreceptor system, OPL, INL and IPL, are shown. Panel C has been overlaid with the sketch of the photoreceptor system of retina including rods, mitochondria, and nucleus. Scale bar is 30 μm and the color scale is from blue (the lowest absorption strength) to red (the highest absorption strength). The colorscales 0-0.3 (WT tissue) and 0-0.6 (Akita/+ tissue) was used for this plot and the same colorscale was used for both mosaics in each tissue. (Aboualizadeh et al., 10.1039/C6AN02603F).

### 5.3.2. Wild-type *vs.* Akita/+ retinal tissue

Retinal tissues prepared from WT and Akita/+ mice were compared. IR absorption spectra generated from each pixel within hyperspectral image in the biochemical spectral region (1800-900 cm⁻¹) and the spectral region primarily attributed to lipids (3050-2750cm⁻¹) were pre-processed for loading into "PCA-LDA" analysis. Spectra from the whole retinal tissue covering

the PRL, the OPL, the INL and the IPL were used for comparison. PC "scores" and "loadings" were generated principally from PCA analysis to identify the class segregation and wavenumbers responsible for the segregation of clusters. LDA was then performed to maximize the variance between groups rather than variations within each group. Figure 5.4A shows 1-dimensional cross-validated scores plot of the retina from WT *vs*. Akita/+ mice after PCA-LDA analysis and the classification. Figure 5.4B depicts the "cluster vector plot" generated from the loadings and discriminating wavenumbers responsible for the separation between the retinas from diabetic and non-diabetic mice. Major differentiating bands that lie in the biochemical spectral region were 1739 cm$^{-1}$, 1710 cm$^{-1}$, 1662 cm$^{-1}$, 1608 cm$^{-1}$, 1550 cm$^{-1}$, 1226 cm$^{-1}$ and 1151 cm$^{-1}$, while other important bands were observed at 964 cm$^{-1}$, 987 cm$^{-1}$, 1051 cm$^{-1}$, 1085 cm$^{-1}$ and 1488 cm$^{-1}$ (lipids). Discriminative bands in the spectral region, associated with saturated and unsaturated fatty acids region, were 2854 cm$^{-1}$, 2923 cm$^{-1}$, 2956 cm$^{-1}$, and an olefinic band at 3012 cm$^{-1}$. The list of differentiating bands between WT and Akita/+ tissues, and their biomolecular assignments are summarized in Table 5.2.
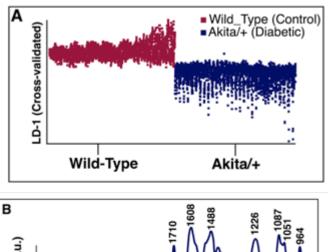
Table 5.2: Major wavenumbers responsibel for classification between retinal tissues from WT and Akita/+ mice (including all retinal layers). [55-59]

| Peak Frequency (cm$^{-1}$) | Assignments |
| --- | --- |
| **3012** | Olefinic=C-H stretching; unsaturated fatty acids |
| **2956** | Asymmetric stretching of CH$_3$; lipids |
| **2923** | Asymmetric stretching of CH$_2$; lipids |
| **2854** | Symmetric stretching of CH$_2$; lipids |
| **1739** | C=O stretching: ester in phospholipids |
| **1710** | Base pair carbonyl (C=O), nucleic acids, DNA, |

| | |
|---|---|
| | RNA, oxidation of cellular lipids, fatty acids |
| **1662** | Amide I- turns $3_{10}$ helical structure of proteins (mainly C-O stretching; contribution from C-N stretching) |
| **1550** | Amide II (N-H bending; C-N stretching) |
| **1488** | Deformation C-H |
| **1226** | Asymmetric stretching of $PO_2^-$ :phospholipids and nucleic acids |
| **1151** | C-O, C-C stretching, C-O-H, C-O-C deformation of carbohydrates/ glycogen |
| **1085** | Symmetric stretching of $PO_2^-$ :phospholipids and nucleic acids |
| **1051** | C–O stretching: deoxyribose/ribose DNA, RNA/ nucleic acids |
| **987** | Nucleic acids and proteins; protein phosphorylation |
| **964** | Nucleic acids, Symmetric $PO_4^-$ stretching (DNA) and deoxyribose; phosphate skeletal motions |

**Figure 5.4:** Comparison of the WT *vs.* Akita/+ retina tissue generated from PCA-LDA analysis. A) 1-dimensional (1D) cross-validated scores plot of the spectra that revealed classification. B) Corresponding Cluster vector plot showing differentiating bands in the biomedical-IR spectral region (1800-900cm$^{-1}$) and lipid region (3050-2750cm$^{-1}$). Spectra are generated from the whole tissue (all retinal layers) and 3600 spectra from each group of samples are used for comparison. (Aboualizadeh et al., 10.1039/C6AN02603F).

### 5.3.3. Photoreceptor layer *vs.* Inner and Outer plexiform layers *vs.* Inner nuclear layer

To gain a better understanding of the impact of oxidative stress on distinctive retinal layers, a separate comparison was made between the PRL, OPL, INL and IPL in the retinal tissue from Akita/+ mice. Individual pixel IR spectra were derived from characteristic layers and compared by using PCA-LDA analysis. Figure 5.5A shows three-dimensional score plots where there was a separation between the PRL and the rest of the retinal layers along LD1. Along LD2, the IPL separated from OPL and INL, while there is some overlap between PRL and IPL. LD3 separated

the OPL from IPL and INL with higher degrees of overlap compared with LD2, and still overlaps with PRL. Three-dimensional score plots revealed the separation of PRL compared with other retinal layers, and there was more variation within the PRL scores compared with the tightly clustered scores in the other layers. Figure 5.5B demonstrates the cluster vector plot for all retinal layers, and when the PRL scores were compared to the scores of OPL, INL and IPL (Fig. 5.5A), the most notable contributing peaks in the loading plot between 1800 and 900 cm$^{-1}$ were 1739 cm$^{-1}$, 1685 cm$^{-1}$, 1654 cm$^{-1}$, 1623 cm$^{-1}$, 1529 cm$^{-1}$, 1236 cm$^{-1}$, 1085 cm$^{-1}$, and 964 cm$^{-1}$, respectively. The major contributing bands between the PRL and rest of the layers in the lipid region were 2850 cm$^{-1}$ and 2921 cm$^{-1}$. The largest peaks in biochemical-IR region, responsible for segregating between the PRL and the other layers, were attributed to nucleic acids. The list of differentiating wavenumbers between the PRL and the other layers with their biomolecular assignments are summarized in Table 5.3.

Table 5.3. Major wavenumbers responsible for the discrimination between distinctive diabetic retinal layers (PRL, OPL, INL, and IPL) [55-59].

| Peak Frequency (cm$^{-1}$) | Assignments |
| --- | --- |
| 2921 | Asymmetric stretching of $CH_2$; lipids |
| 2850 | Symmetric stretching of $CH_2$; lipids |
| 1739 | C=O stretching: ester in phospholipids |
| 1685 | Amide I- β sheets, antiparallel/random coil (mainly C-O stretching, contribution from C-N stretching) |
| 1654 | Amide I- α helical or unordered structure of proteins (proteins C-O stretching, C-N stretch, CCN deformation) |
| 1623 | Amide I of aggregated strand structures (mainly C-O stretching, contribution from |

124

|  | C-N stretching) |
|---|---|
| **1529** | Amide II- β sheets (mainly N-H bending and C-N stretching) |
| **1236** | Asymmetric stretching of $PO_2^-$ :phospholipids and nucleic acids |
| **1085** | Symmetric stretching of $PO_2^-$ :phospholipids and nucleic acids |
| **964** | Nucleic acids, Symmetric $PO_4^-$ stretching (DNA) and deoxyribose; phosphate skeletal motions |
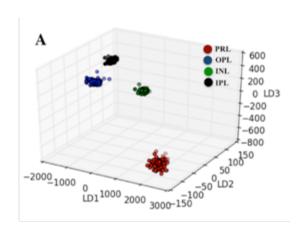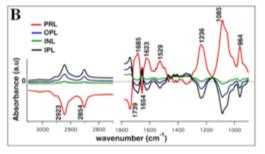


**Figure 5.5:** Comparison of the PRL (red dots), OPL (blue dots), INL (green dots) and IPL (black dots) of Akita/+ retina tissue by means of PCA-LDA is shown. A) 3-dimensional (3D) scores plot of the spectra showing the separation of the PRL from other layers along LD1. B) Cluster vector plot of A; highlighting the discriminating wavenumbers responsible for the separation. Nearly 1500 spectra from each layer of the retina were generated and compared. (Aboualizadeh et al., 10.1039/C6AN02603F).
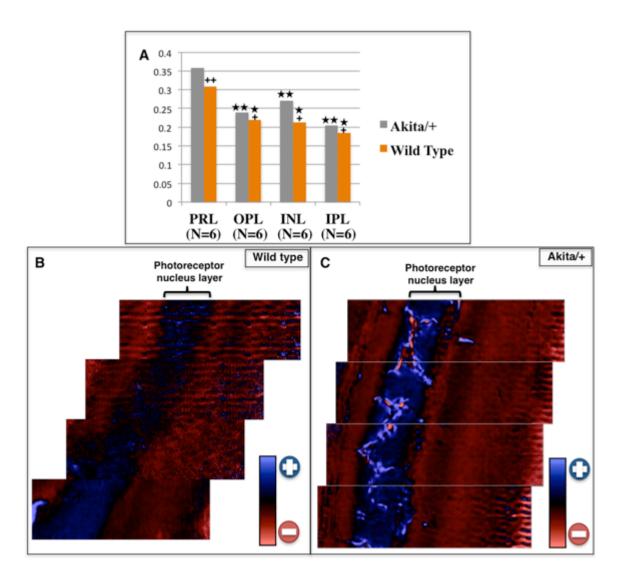
**Figure 5.6:** The ratio of $\nu_{asym}$ $PO^{2-}$ band to protein band for the WT and Akita/+ retina tissues. A) Comparison of the $\nu_{asym}$ $PO^{2-}$ /protein (1230cm$^{-1}$/Amide II (1546 cm$^{-1}$)), and among the PRL, OPL, INL and IPL within each tissue. + was used for the comparison of the WT and the Akita/+ and ★ was used for the comparison of the PRL with the rest of the layers. P< 0.05 is the level of significance. B,C) Spectral maps of the $\nu_{asym}$ $PO^{2-}$ /protein ratio in WT (B) and Akita/+ (C) tissues, showing the absorption strength of the PRL among layers. The representative images are on a three-color coded color scale, where the blue/red color is associated with the highest/lowest absorption. The spectral regions 1180-1280 cm$^{-1}$ (for the phosphate band) and 1500-1750 cm$^{-1}$ (for protein band Amide II) were used as a baseline. (Aboualizadeh et al., 10.1039/C6AN02603F).

### 5.3.4. Nucleic acid to protein ratio in the retinal tissue

To reinforce the rationality of our findings and obtain a better knowledge of diabetes-induced alterations in the composition and concentration of molecules, the band area ratios for some functional groups of retinal tissues from WT and Akita/+ mice were evaluated. In tissue studies, the differences in the thickness of tissues can influence cellular alterations and spectral interpretation. Thus, to avoid such errors the ratio of integral intensities was employed. $\nu_{asym} PO^{2-}$ to protein ratio was calculated by dividing the baseline-corrected area under the functional group attributed to asymmetric stretching of phosphates at 1230 cm$^{-1}$ and one of the main FTIR markers of DNA [60, 61] by Amide II absorption band (1544 cm$^{-1}$). The ratio was calculated for the PRL, OPL, INL and IPL of the retina in both types of mice, and a comparison was made of the layers per tissue type (WT $vs.$ Akita/+) and per layer for each tissue. The spectral regions 1180-1280 cm$^{-1}$ (for the phosphate band) and 1500-1750 cm$^{-1}$ (for Amide II band) were used as a baseline. The PRL demonstrated the highest amount of $\nu_{asym} PO^{2-}$/protein (in both tissues) compared to OPL, INL and IPL.

The sample from Akita/+ mice had a higher amount of this ratio in all layers compared to WT group. Both tissues follow the same trend of having either increasing or decreasing $\nu_{asym} PO^{2-}$/protein between layers. P-values were calculated and $P< 0.05$ was considered to be significantly different among groups of samples and retina layers. Results from the statistical analysis for both tissues are demonstrated in Figure 5.6A. A spectral map of $\nu_{asym} PO^{2-}$ to protein ratio of retinas from WT and Akita/+ mice are shown in Figures 5.6B, C. These ratio images were used to visually discern the strength of the relative concentration of phosphates, and alterations in tissue morphology associated with diabetes-induced damage between the layers. The area of nearly 270 × 270 μm$^2$ of the retina tissues are shown in Figures 5.6B, C, where the

127

blue color shows the highest value of ratio and the red color indicates the lowest value. This Figure demonstrates the strength of PRL, and in particular the nuclear segment of the photoreceptor layer compared to the other layers. The ratio image for the retina from WT mice shows a homogenous morphology within the retina layers, while the retina from Akita/+ mice is more heterogeneous in the nuclear segment of photoreceptors. The $v_{asym}$ $PO^{2-}$ to protein ratio images (Fig. 5.6) enabled us to resolve in detail the subtle heterogeneities observed in the inner segment of photoreceptors within chemical images of diabetic retina (Fig. 5.3C).
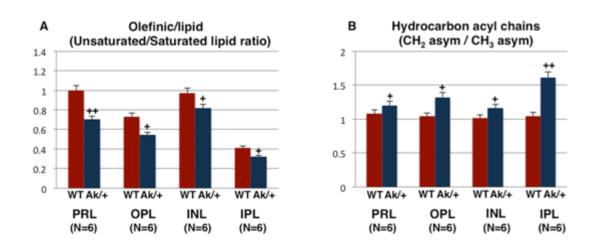


**Figure 5.7:** Bar graphs of the olefinic/lipid ratio and qualitative hydrocarbon acyl chains in lipids are shown. A) The unsaturated/saturated lipid ratio and B) The $CH_2/CH_3$ asym ratio of the WT and Akita/+ retina tissues were compared. + was used for comparison of WT and Akita/+ tissues. (Aboualizadeh et al., 10.1039/C6AN02603F).

### 5.3.5. Unsaturation level and hydrocarbon acyl chains in lipids

The olefinic to lipid ratio, also known as unsaturation index, is used to find the relative amount of unsaturated lipids in retinal tissue. This ratio is calculated by dividing the area of the $v=(CH)$ peak at 3012 $cm^{-1}$, attributed mainly to unsaturated lipids, by area of the C-H region

attributed to symmetric and asymmetric stretching of $CH_2$ and $CH_3$ in 2830-2980 cm$^{-1}$ (lipids). The spectral region 2800-3050 cm$^{-1}$ was used as a baseline region. A remarkable decrease in the ratio was observed in retinal layers from Akita/+ mice compared with WT mice, while the PRL demonstrated the largest decrease amongst the layers (Fig. 5.7.A).

To determine the diabetes-induced changes in hydrocarbon acyl chain length of lipids, the ratio of $\nu_{as}\,CH_2/\nu_{as}\,CH_3$ was calculated. There was an increase in retinal layers from Akita/+ mice compared with WT mice (Figure 5.7B). As shown in Table 5.1., the areas under 2960 cm$^{-1}$ and 2921 cm$^{-1}$ bands were calculated and there was an increase in the band area in Akita/+ groups (for all retinal layers) compared with WT groups. The variation of ratio between WT layers was negligibly smaller. The results of statistical analysis are shown in Figure 5.7B.

## 5.4. Discussion

Understanding biophysical and biochemical features of retinal tissue at subcellular level plays a major role in the pathogenesis of diabetes and particularly, in revealing the mechanism underlying the oxidative stress damage in the retina. Identifying biomarkers with spatial resolution at the cellular and molecular level is critical for early detection and a better understanding of the disease pathogenesis. The first goal of this study, which was the determination of biomarkers of diabetes-induced oxidative damage in the retina, was achieved by employing PCA-LDA. I demonstrated the efficacy of s-FTIR imaging and multivariate image analysis in classification of control and diabetic tissues (Fig. 5.4.) and the series of IR bands (Table 5.2.) in proteins, nucleic acids, and lipids attributed to this separation were found. FTIR images of retinas that were imaged at the most advanced infrared beamline (IRENI) revealed all distinctive layers of the retina. High resolution spatially resolved chemical images integrated

over the IR band at 1712 cm$^{-1}$ from Akita/+ tissue demonstrated heterogeneous morphology within the nucleus segment of photoreceptors, while the WT retina tissue looked more homogenous within the same layer (Fig. 5.3.C). However, the OPL, INL, and IPL revealed a homogenous structure in both WT and Akita/+ tissues. Notably, the band at 1712 cm$^{-1}$ has been only observed in the spectra from the nucleus segment of photoreceptors [35]. The 1712 cm$^{-1}$ band has also been reported as a marker for determination of free fatty acids [62], and carbonyl group products that are produced by deposition of glycation products [63]. This band was found as one of the major differentiating wavenumbers between the WT and Akita/+ tissues, which suggests the significance of the photoreceptor cell's nucleus in the observed classification.

The second goal of this study was to determine the diabetes-induced alterations in the biochemistry of distinctive layers of the retina. Three-dimensional score plots from PCA-LDA analysis exclusively on Akita/+ tissue (Fig. 5.5A) revealed clear separation among the retinal layers. Along LD1, there was a separation between PRL and the rest of the layers, and the IR bands that were responsible for the classification are reported (Table 5.3.). This finding recommended that at the initial stage of DR, PRL was the most vulnerable retinal layer in comparison with the other layers. There were three major differentiating bands in the DNA/RNA region (1425-900 cm$^{-1}$) of the cluster vector plot at 964cm$^{-1}$ (symmetric PO$_4^-$ stretching (DNA)/deoxyribose/backbone (C-C)), 1085cm$^{-1}$ ($\nu_{sym}$ PO$^{2-}$), and 1236 cm$^{-1}$ ($\nu_{asym}$ PO$^{2-}$) (Fig. 6.5B). Peak characteristic for symmetric and asymmetric phosphate bands at 1080 and 1236 cm$^{-1}$, for the inner and outer segments of photoreceptor has been shown [35]. The peaks of symmetric and asymmetric stretching vibrations of phosphates have been reported in the double stranded DNA spectra in several studies [60,61].

The ratio of $\nu_{asym}PO^{2-}$ to protein was also found (Fig. 5.6) to provide information about the changes in nucleic acid content in comparison to protein content. The higher level of $\nu_{asym}PO^{2-}$/protein in the PRL in our findings could be indicative of localization of DNA damage in PRL, due to the proximity of nuclei to sites of superoxide generation in photoreceptors. Heterogeneities in the ratio images of retinas from Akita/+ mice that appeared within nucleus segment of PRL (Fig. 5.6C) suggest morphological changes as a result of diabetes-induced oxidative stress. The morphological variations in the thickness of retinal layers at different stages of diabetes, and the role of early phase photoreceptor loss during diabetes have been studied [64]. I believe that the segregation between PRL (which is a dense layer in nuclei) and the other layers, and the presence of differentiating bands attributed to nucleic acids, indicates the oxidative DNA damage in the retina, and in particular in the PRL.

It is well established that the oxidative damage to DNA is elevated in the retina at early stages of diabetes mellitus [65-67]. The significance of photoreceptor changes in the pathogenesis of DR is evaluated in several studies [68-70]. Photoreceptors are the major source of superoxide and reactive oxygen species (ROS) compared with INL or ganglion cell layer (GCL) and contribute to the greater extent to the oxidative stress during diabetes [71]. Most of the mitochondria are located in the photoreceptor layer (where I observe the most variations between diabetic and WT tissues) and mitochondrial DNA (mtDNA) is the most vulnerable target for ROS and oxidative damage [72]. The contribution of mitochondria in diabetes-induced oxidative damage is well-established [73,74].

Our results also identified differentiating spectral features between WT and Akita/+ retina in saturated and unsaturated fatty acids (Fig. 5.4). Differentiating peak at 3012 cm$^{-1}$ could be

attributed to the richness of PUFA disks in the inner segment of photoreceptors. The olefinic to lipid ratio, used as the level of unsaturation in lipids, decreased in Akita/+ mice compared with WT mice. Notably, the diabetic PRL showed the largest decrease among the retinal layers (Fig. 5.7A). The decrease in this ratio in diabetic retinal layers, suggests the loss of unsaturation in acyl chains of lipids due to an elevated lipid peroxidation in diabetic retina. 4-Hydroxyalkenals are the most toxic products in lipid peroxidation and were found in the retina as early as 6 weeks of diabetes [75].

Our results was found to be in agreement with several studies on diabetes-induced changes in retinal fatty acid metabolism [76,77] that revealed a significant decrease in unsaturation level in diabetic retina. Lipid peroxidation serves as an indicator of the oxidative stress in diabetes mellitus [52], and it occurs due to the abundance of unsaturated fatty acids in biological membranes that are mainly attacked by free radicals. The oxidation of unsaturated fatty acids is well established and poly-unsaturated fatty acids are more susceptible to peroxidation due to the number of double bonds [78]. The changes in unsaturated fatty acids can affect the structure and functionality of the membranes and signal propagation; however, these changes can adversely affect the integrity of membrane [79].

$CH_2$/$CH_3$ antisymmetric stretching ratio (FTIR-based hydrocarbon acyl chain in lipids) was larger for Akita/+ mice compared with WT mice, and it was significantly larger for OPL and IPL due to the richness of the plexiform layers in lipids associated with the network of axons and synapses (Fig. 5.7B). The IPL and OPL demonstrated comparable biochemistry in the chemical images integrated at peaks 2850 cm$^{-1}$ and 1738 cm$^{-1}$, shown in ref [35]. Qualitative longer chains of hydrocarbon acyl of lipids in diabetic groups suggest changes in the membrane and lipid

132

metabolism [80] at the early stages of diabetes, and the significance of plexiform layers in these alterations compared to the outer and inner nucleus segments of the retina.

## 5.5. Concluding remarks

DR causes progressive damage to the retina tissue that can lead to serious complications including retinal detachment, vitreous hemorrhage, glaucoma, and blindness. Here I demonstrated the efficacy of high-resolution synchrotron-based FTIR wide field imaging and PCA-LDA to differentiate between diabetic and non-diabetic retina tissues with robust classification, and determine the highly localized early diabetes-induced biochemical alterations in the retina. Spectral biomarkers of diabetes-induced changes in distinctive retinal layers attributed to nucleic acids, proteins, and lipids, were delineated. This is the first study to report the nature of molecular changes in the biochemistry of distinctive layers of retina during diabetes. One important finding of this study is that super resolution FTIR images providing information about the significance of PRL at the onset of DR and the heterogeneities associated with diabetes-induced changes in the nucleus segment of photoreceptors. Findings from ratios of several IR bands, including an increase in nucleic acid/protein, a decrease in olefinic/lipid, and an increase in hydrocarbon acyl chains in lipids, in the diabetic retina, is reported. Comparison between distinctive layers of retina in the diabetic and WT mice indicated that the PRL experienced the most obvious impact at the onset of diabetes. The current study provides substantial mechanistic understanding of the oxidative damage in the retina, which may shed import insight into the pathogenesis and diagnosis of DR. Future work will focus on temporal and persistence of these changes and their contribution to retinal complications associated with diabetes.

## 5.6. References

1. Prasad, S., Kamath, G. G., Jones, K., Clearkin, L. G., & Phillips, R. P. (2001). Prevalence of blindness and visual impairment in a population of people with diabetes. Eye 15, 640-643.

2. Ly, A., Yee, P., Vessey, K. A., Phipps, J. A., Jobling, A. I., & Fletcher, E. L. (2011). Early Inner Retinal Astrocyte Dysfunction during Diabetes and Development of Hypoxia, Retinal Stress, and Neuronal Functional Loss. Investigative Ophthalmology & Visual Science 52(13), 9316-9326.

3. Kowluru, R. A., & Chan, P.-S. (2007). Oxidative Stress and Diabetic Retinopathy. *Experimental Diabetes Research*.

4. Maritim, A. C., Sanders, R. A., & Watkins, J. B. (2003). Diabetes, oxidative stress, and antioxidants: A review. *Journal of Biochemical and Molecular Toxicology, 17*(1), 24-38.

5. Kowluru, R. A. (2001). Diabetes-induced elevations in retinal oxidative stress, protein kinase C and nitric oxide are interrelated. *Acta Diabetologica, 38*(4), 179-185.

6. Kowluru, R. A., & Abbas, S. N. (2003). Diabetes-induced mitochondrial dysfunction in the retina. *Investigative Ophthalmology & Visual Science, 44*(12), 5327-5334.

7. Roy, S., Ha, J., Trudeau, K., & Beglova, E. (2010). Vascular Basement Membrane Thickening in Diabetic Retinopathy. *Current Eye Research, 35*(12), 1045-1056.

8. Stem, M. S., & Gardner, T. W. (2013). Neurodegeneration in the Pathogenesis of Diabetic Retinopathy: Molecular Mechanisms and Therapeutic Implications. *Current Medicinal Chemistry, 20*(26), 3241-3250.

9. Mattson, E. C., Unger, M., Sedlmair, J., Nasse, M., Aboualizadeh, E., Alavi, Z., & Hirschmugl, C. J. (2014). Widefield FT-IR 2D and 3D Imaging at the Microscale Using Synchrotron Radiation. Infrared and Raman Spectroscopic Imaging: Second, Completely Revised and Updated Edition, 585-618.

10. Chan, K. L. A., & Kazarian, S. G. (2016). Attenuated total reflection Fourier-transform infrared

(ATR-FTIR) imaging of tissues and live cells. *Chemical Society Reviews, 45*(7), 1850-1864.

11. Walsh, M. J., Reddy, R. K., & Bhargava, R. (2012). Label-Free Biomedical Imaging With Mid-IR Spectroscopy. *Ieee Journal of Selected Topics in Quantum Electronics, 18*(4), 1502-1513.

12. Kazarian, S. G., & Chan, K. L. A. (2006). Applications of ATR-FTIR spectroscopic imaging to biomedical samples. *Biochimica Et Biophysica Acta-Biomembranes, 1758*(7), 858-867.

13. Bellisola, G., & Sorio, C. (2012). Infrared spectroscopy and microscopy in cancer research and diagnosis. [Review]. *American Journal of Cancer Research, 2*(1), 1-21.

14. Bambery, K. R., Schultke, E., Wood, B. R., MacDonald, S. T. R., Ataelmannan, K., Griebel, R. W., et al. (2006). A Fourier transform infrared micro spectroscopic imaging investigation into an animal model exhibiting glioblastoma multiforme. *Biochimica Et Biophysica Acta-Biomembranes, 1758*(7), 900-907.

15. Lasch, P., Haensch, W., Naumann, D., & Diem, M. (2004). Imaging of colorectal adenocarcinoma using FT-IR microspectroscopy and cluster analysis. *Biochimica Et Biophysica Acta-Molecular Basis of Disease, 1688*(2), 176-186.

16. Quaroni, L., & Casson, A. G. (2009). Characterization of Barrett esophagus and esophageal adenocarcinoma by Fourier-transform infrared microscopy. *Analyst, 134*(6), 1240-1246.

17. Gazi, E., Dwyer, J., Gardner, P., Ghanbari-Siahkali, A., Wade, A. P., Miyan, J., et al. (2003). Applications of Fourier transform infrared microspectroscopy in studies of benign prostate and prostate cancer. A pilot study. *Journal of Pathology, 201*(1), 99-108.

18. Levin, I. W., & Bhargava, R. (2005). Fourier transform infrared vibrational spectroscopic imaging: Integrating microscopy and molecular recognition. *Annual Review of Physical Chemistry, 56*, 429-474.

19. Fernandez, D. C., Bhargava, R., Hewitt, S. M., & Levin, I. W. (2005). Infrared spectroscopic imaging for histopathologic recognition. *Nature Biotechnology, 23*(4), 469-474.

20. Gasper, R., Mijatovic, T., Benard, A., Derenne, A., Kiss, R., & Goormaghtigh, E. (2010). FTIR

spectral signature of the effect of cardiotonic steroids with antitumoral properties on a prostate cancer cell line. *Biochimica Et Biophysica Acta-Molecular Basis of Disease, 1802*(11), 1087-1094.

21. Malins, D. C., Johnson, P. M., Barker, E. A., Polissar, N. L., Wheeler, T. M., & Anderson, K. M. (2003). Cancer-related changes in prostate DNA as men age and early identification of metastasis in primary prostate tumors. *Proceedings of the National Academy of Sciences of the United States of America, 100*(9), 5401-5406.

22. Yano, K., Ohoshima, S., Gotou, Y., Kumaido, K., Moriguchi, T., & Katayama, H. (2000). Direct measurement of human lung cancerous and noncancerous tissues by Fourier transform infrared microscopy: Can an infrared microscope be used as a clinical tool? *Analytical Biochemistry, 287*(2), 218-225.

23. Bird, B., Miljković, M., Romeo, M.J., Smith, J., Stone, N., George, M.W., Diem, M. (2008). Infrared Micro-Spectral Imaging: Automatic Distinction of Tissue Types in Axillary Lymph Node Histology". BMC Clinical Pathology 8, 8.

24. Wood, B. R., Chiriboga, L., Yee, H., Quinn, M. A., McNaughton, D., & Diem, M. (2004). Fourier transform infrared (FTIR) spectral mapping of the cervical transformation zone, and dysplastic squamous epithelium. *Gynecologic Oncology, 93*(1), 59-68.

25. Barabas, M. E., Mattson, E. C., Aboualizadeh, E., Hirschmugl, C. J., & Stucky, C. L. (2014). Chemical Structure and Morphology of Dorsal Root Ganglion Neurons from Naive and Inflamed Mice. *Journal of Biological Chemistry, 289*(49), 34241-34249.

26. Hackett, M. J., Caine, S., Liu, X., May, T. E., & Borondics, F. (2015). Development of single-beam wide-field infrared imaging to study sub-cellular neuron biochemistry. *Vibrational Spectroscopy, 77*, 51-59.

27. Hackett, M. J., Borondics, F., Brown, D., Hirschmugl, C., Smith, S. E., Paterson, P. G., et al. (2013). Subcellular Biochemical Investigation of Purkinje Neurons Using Synchrotron Radiation Fourier Transform Infrared Spectroscopic Imaging with a Focal Plane Array Detector. *Acs Chemical Neuroscience, 4*(7), 1071-1080.

28. Ami, D., Mereghetti, P., Natalello, A., Doglia, S. M., Zanoni, M., Redi, C. A., et al. (2011). FTIR

spectral signatures of mouse antral oocytes: Molecular markers of oocyte maturation and developmental competence. *Biochimica Et Biophysica Acta-Molecular Cell Research, 1813*(6), 1220-1229.

29. Kelly, J. G., Nakamura, T., Kinoshita, S., Fullwood, N. J., & Martin, F. L. (2010). Evidence for a stem-cell lineage in corneal squamous cell carcinoma using synchrotron-based Fourier-transform infrared microspectroscopy and multivariate analysis. *Analyst, 135*(12), 3120-3125.

30. Bozkurt, O., Severcan, M., & Severcan, F. (2010). Diabetes induces compositional, structural and functional alterations on rat skeletal soleus muscle revealed by FTIR spectroscopy: a comparative study with EDL muscle. *Analyst, 135*(12), 3110-3119.

31. Severcan, F., Bozkurt, O., Gurbanov, R., & Gorgulu, G. (2010). FT-IR spectroscopy in diagnosis of diabetes in rat animal model. *Journal of Biophotonics, 3*(8-9), 621-631.

32. Toyran, N., Lasch, P., Naumann, D., Turan, B., & Severcan, F. (2006). Early alterations in myocardia and vessels of the diabetic rat heart: an FTIR microspectroscopic study. *Biochemical Journal, 397*, 427-436.

33. Yoshida, S., Yoshida, M., Yamamoto, M., & Takeda, J. (2013). Optical screening of diabetes mellitus using non-invasive Fourier-transform infrared spectroscopy technique for human lip. *Journal of Pharmaceutical and Biomedical Analysis, 76*, 169-176.

34. Scott, D. A., Renaud, D. E., Krishnasamy, S., Meric, P., Buduneli, N., Cetinkalp, S., et al. (2010). Diabetes-related molecular signatures in infrared spectra of human saliva. *Diabetology & Metabolic Syndrome, 2*.

35. Kastyak-Ibrahim, M. Z., Nasse, M. J., Rak, M., Hirschmugl, C., Del Bigio, M. R., Albensi, B. C., et al. (2012). Biochemical label-free tissue imaging with subcellular-resolution synchrotron FTIR with focal plane array detector. *Neuroimage, 60*(1), 376-383.

36. Martin, F. L., German, M. J., Wit, E., Fearn, T., Ragavan, N., & Pollock, H. M. (2007). Identifying variables responsible for clustering in discriminant analysis of data from infrared microspectroscopy of a biological sample. *Journal of Computational Biology, 14*(9), 1176-1184.

37. Baker, M. J., Trevisan, J., Bassan, P., Bhargava, R., Butler, H. J., Dorling, K. M., et al. (2014).

Using Fourier transform IR spectroscopy to analyze biological materials. *Nature Protocols, 9*(8), 1771-1791.

38. Stitt, D. M., Kastyak-Ibrahim, M. Z., Liao, C. R., Morrison, J., Albensi, B. C., & Gough, K. M. (2012). Tissue acquisition and storage associated oxidation considerations for FTIR microspectroscopic imaging of polyunsaturated fatty acids. *Vibrational Spectroscopy, 60*, 16-22.

39. Miller, L. M., & Dumas, P. (2006). Chemical imaging of biological tissue with synchrotron infrared light. *Biochimica Et Biophysica Acta-Biomembranes, 1758*(7), 846-857.

40. Marcelli, A., Cricenti, A., Kwiatek, W. M., & Petibois, C. (2012). Biological applications of synchrotron radiation infrared spectromicroscopy. *Biotechnology Advances, 30*(6), 1390-1404.

41. Dumas P., Sockalingum G.D., Sule-Suso J. (2007). Adding Synchrotron Radiation to Infrared Microspectroscopy: What's New in Biomedical Applications?. Trends Biotechnol. 25(1), 40–44.

42. Miller, L., Tobin, M.J., Srichan, S., Dumas, P. (2008). In Biomedical Applications of FTIR Spectroscopy, ed. A. Barth, P. Haris, IOS Press, Netherlands, 2$^{nd}$ edition, Ch. 14, 403-428.

43. Mattson, E. C., Unger, M., Clede, S., Lambert, F., Policar, C., Imtiaz, A., et al. (2013). Toward optimal spatial and spectral quality in widefield infrared spectromicroscopy of IR labelled single cells. *Analyst, 138*(19), 5610-5618.

44. Holman, H. Y. N., Bechtel, H. A., Hao, Z., & Martin, M. C. (2010). Synchrotron IR Spectromicroscopy: Chemistry of Living Cells. *Analytical Chemistry, 82*(21), 8757-8765.

45. Holman, H. Y. N., Bjornstad, K. A., McNamara, M. P., Martin, M. C., McKinney, W. R., & Blakely, E. A. (2002). Synchrotron infrared spectromicroscopy as a novel bioanalytical microprobe for individual living cells: cytotoxicity considerations. *Journal of Biomedical Optics, 7*(3), 417-424.

46. Nasse, M. J., Walsh, M. J., Mattson, E. C., Reininger, R., Kajdacsy-Balla, A., Macias, V., et al. (2011). High-resolution Fourier-transform infrared chemical imaging with multiple synchrotron beams.

*Nature Methods, 8*(5), 413-U458.

47. Hirschmugl, C. J., & Gough, K. M. (2012). Fourier Transform Infrared Spectrochemical Imaging: Review of Design and Applications with a Focal Plane Array and Multiple Beam Synchrotron Radiation Source. *Applied Spectroscopy, 66*(5), 475-491.

48. Davis, B. J., Carney, P. S., & Bhargava, R. (2010a). Theory of Mid-infrared Absorption Microspectroscopy: II. Heterogeneous Samples. *Analytical Chemistry, 82*(9), 3487-3499.

49. Davis, B. J., Carney, P. S., & Bhargava, R. (2010b). Theory of Midinfrared Absorption Microspectroscopy: I. Homogeneous Samples. *Analytical Chemistry, 82*(9), 3474-3486.

50. Bassan, P., Kohler, A., Martens, H., Lee, J., Byrne, H. J., Dumas, P., et al. (2010). Resonant Mie Scattering (RMieS) correction of infrared spectra from highly scattering biological samples. Analyst, 135(2), 268-277.

51. Bassan, P., Kohler, A., Martens, H., Lee, J., Jackson, E., Lockyer, N., Dumas, P., Brown, M., Clarke, N. and Gardner, P. (2010), RMieS-EMSC correction for infrared spectra of biological cells: Extension using full Mie theory and GPU computing. J. Biophoton., 3, 609–620.

52. Mattson, E. C., Unger, M., Clede, S., Lambert, F., Policar, C., Imtiaz, A., et al. (2013). Toward optimal spatial and spectral quality in widefield infrared spectromicroscopy of IR labelled single cells. Analyst, 138(19), 5610-5618.

53. Imtiaz, A. (2015). Scattering Correction Methods of Infrared Spectra Using Graphics Processing Units, Master of Science thesis, University of Wisconsin-Milwaukee.

54. Baker, M. J., Gazi, E., Brown, M. D., Shanks, J. H., Gardner, P., & Clarke, N. W. (2008). FTIR-based spectroscopic analysis in the identification of clinically aggressive prostate cancer. British Journal of Cancer, 99(11), 1859-1866.

55. Barth, A., & Zscherp, C. (2002). What vibrations tell us about proteins. Quarterly Reviews of Biophysics, 35(4), 369-430.

56. Meade, A. D., Lyng, F. M., Knief, P., & Byrne, H. J. (2007). Growth substrate induced functional changes elucidated by FTIR and Raman spectroscopy in in-vitro cultured human keratinocytes. Analytical and Bioanalytical Chemistry, 387(5), 1717-1728.

57. Movasaghi, Z., Rehman, S., & Rehman, I. U. (2008). Fourier transform infrared (FTIR) spectroscopy of biological tissues. Applied Spectroscopy Reviews, 43(2), 134-179.

58. Naumann, D. (2001). FT-infrared and FT-Raman spectroscopy in biomedical research. Applied Spectroscopy Reviews, 36(2-3), 239-298.

59. Liu, K. Z., Jackson, M., Sowa, M. G., Ju, H. S., Dixon, I. M. C., & Mantsch, H. H. (1996). Modification of the extracellular matrix following myocardial infarction monitored by FTIR spectroscopy. Biochimica Et Biophysica Acta-Molecular Basis of Disease, 1315(2), 73-77.

60. Banyay, M., Sarkar, M., & Graslund, A. (2003). A library of IR bands of nucleic acids in solution. Biophysical Chemistry, 104(2), 477-488.

61. Whelan, D. R., Bambery, K. R., Heraud, P., Tobin, M. J., Diem, M., McNaughton, D., et al. (2011). Monitoring the reversible B to A-like transition of DNA in eukaryotic cells using Fourier transform infrared spectroscopy. Nucleic Acids Research, 39(13), 5439-5448.

62. Lam, H. S., Proctor, A., & Meullenet, J. F. (2001). Free fatty acid formation and lipid oxidation on milled rice. *Journal of the American Oil Chemists Society, 78*(12), 1271-1275.

63. Huang, Y. T., Liao, H. F., Wang, S. L., & Lin, S. Y. (2016). Glycation and secondary conformational changes of human serum albumin: study of the FTIR spectroscopic curve-fitting technique. *Aims Biophysics, 3*(2), 247-260.

64. Park, S. H., Park, J. W., Park, S. J., Kim, K. Y., Chung, J. W., Chun, M. H., et al. (2003). Apoptotic death of photoreceptors in the streptozotocin-induced diabetic rat retina. *Diabetologia, 46*(9), 1260-1268.

65. Finkel, T., & Holbrook, N. J. (2000). Oxidants, oxidative stress and the biology of ageing. *Nature, 408*(6809), 239-247.

66. Baynes, J. W., & Thorpe, S. R. (1999). Role of oxidative stress in diabetic complications - A new perspective on an old paradigm. *Diabetes, 48*(1), 1-9.

67. Kowluru, R. A., & Chan, P.S. (2007). Oxidative Stress and Diabetic Retinopathy. *Experimental Diabetes Research*.

68. Greenstein, V., Sarter, B., Hood, D., Noble, K., Carr, R. (1990). Hue discrimination and S cone pathway sensitivity in early diabetic retinopathy. Invest Ophthalmol Vis Sci. 31, 1008–1014.

69. Holopigian, K., Greenstein, V.C., Seiple, W., Hood, D.C., Carr, R.E. (1997). Evidence for photoreceptor changes in patients with diabetic retinopathy. Invest Ophthalmol Vis Sci. 38, 2355–2365.

70. Kern, T. S., & Berkowitz, B. A. (2015). Photoreceptors in diabetic retinopathy. *Journal of Diabetes Investigation, 6*(4), 371-380.

71. Du, Y. P., Miller, C. M., & Kern, T. S. (2003). Hyperglycemia increases mitochondrial superoxide in retina and retinal cells. *Free Radical Biology and Medicine, 35*(11), 1491-1499.

72. Ames, B. N., Shigenaga, M. K., & Hagen, T. M. (1993). OXIDANTS, ANTIOXIDANTS, AND THE DEGENERATIVE DISEASES OF AGING. *Proceedings of the National Academy of Sciences of the United States of America, 90*(17), 7915-7922.

73. Du, Y. P., Miller, C. M., & Kern, T. S. (2003). Hyperglycemia increases mitochondrial superoxide in retina and retinal cells. *Free Radical Biology and Medicine, 35*(11), 1491-1499.

74. Nishikawa, T., Edelstein, D., Du, X. L., Yamagishi, S., Matsumura, T., Kaneda, Y., et al. (2000). Normalizing mitochondrial superoxide production blocks three pathways of hyperglycaemic damage. *Nature, 404*(6779), 787-790.

75. Baydas, G., Tuzcu, M., Yasar, A., & Baydas, B. (2004). Early changes in glial reactivity and lipid peroxidation in diabetic rat retina: effects of melatonin. *Acta Diabetologica, 41*(3), 123-128.

76. Tikhonenko, M., Lydic, T. A., Wang, Y., Chen, W. Q., Opreanu, M., Sochacki, A., et al. (2010). Remodeling of Retinal Fatty Acids in an Animal Model of Diabetes A Decrease in Long-Chain Polyunsaturated Fatty Acids Is Associated With a Decrease in Fatty Acid Elongases Elovl2 and Elovl4. *Diabetes, 59*(1), 219-227.

77. Koehrer, P., Saab, S., Berdeaux, O., Isaico, R., Gregoire, S., Cabaret, S., et al. (2014). Erythrocyte Phospholipid and Polyunsaturated Fatty Acid Composition in Diabetic Retinopathy. *Plos One, 9*(9).

78. Halliwell, B., & Chirico, S. (1993). LIPID-PEROXIDATION - ITS MECHANISM, MEASUREMENT, AND SIGNIFICANCE. *American Journal of Clinical Nutrition, 57*(5), 715-725.

79. Ruthven N.A.H., L. & McElhaney, R.N. (2013). Membrane lipid phase transitions and phase organization studied by Fourier transform infrared spectroscopy, Biochimica et Biophysica Acta (BBA) - Biomembranes, 1828 (10), 2347-2358.

80. Pamplona, R. (2008). Membrane phospholipids, lipoxidative damage and molecular integrity: A causal role in aging and longevity. *Biochimica Et Biophysica Acta-Bioenergetics, 1777*(10), 1249-126.

**Chapter 6: Temporal diabetes-induced biochemical changes in distinctive layers of mouse retina**

To discover the mechanisms underlying the development and progression of diabetes changes in the retina, a more comprehensive understanding of the bio-molecular processes in individual retinal cells subjected to hyperglycemia is required. Animal models provide a suitable model for detecting the underlying pathophysiological mechanisms of DR, which is not fully attainable in human studies. In the present chapter, I discuss the nature of diabetes-induced, highly localized biochemical changes in the retinal tissue from Ins2$^{Akita/+}$ (Akita/+; a model of Type I diabetes) male mice with different duration of diabetes. Employing label-free spatially resolved Fourier transform infrared (FT-IR) imaging engaged with chemometric tools enabled us to identify temporal-dependent reproducible biomarkers of the diabetic retinal tissue from mice with 6 or 12 weeks, and 6 or 10 months of diabetes. I report, for the first time, the origin of molecular changes in the biochemistry of individual retinal layers with different duration of diabetes. A robust classification between distinctive retinal layers namely photoreceptor layer (PRL), outer plexiform layer (OPL), inner nuclear layer (INL), and inner plexiform layer (IPL), and associated temporal-dependent spectral biomarkers were delineated. Spatially-resolved super resolution chemical images revealed oxidative stress-induced structural and morphological alterations within the nucleus of the photoreceptors. Comparison among the PRL, OPL, INL, and IPL suggested that the photoreceptor layer is the most susceptible layer to the oxidative stress with short-duration of diabetes. Moreover, for the first time, I present the temporal-dependent biomolecular alterations for the PRL, OPL, INL, and IPL from Akita/+ mice, as diabetes progresses. These findings are potentially important that may be of particular benefit in understanding the molecular and biological activity of retinal cells during oxidative stress in diabetes, which is still unclear. My integrating paradigm provides a new conceptual framework

and a significant rationale for a better understanding of the molecular and cellular mechanisms underlying the development and progression of DR. This approach may yield alternative and potentially complementary methods for the assessment of diabetes changes.

## 6.1. Introduction

Diabetic retinopathy (DR) is a retinal microvascular dysfunction that affects retinal vascular homeostasis and can ultimately lead to blindness [1]. Accumulation of fluids in the eye causes a change in the curvature of the lens; therefore, exacerbate the focusing and eventually leads to blurred vision over time. There are two major stages of DR, namely non-proliferative diabetic retinopathy (NPDR) and proliferative diabetic retinopathy (PDR). The classification is based on morphological changes observed in the retinal vasculature, retinal abnormalities, blurred vision, and progressive visual loss [2]. The various cellular components of the retina, especially the vascular cells, may be susceptible to the hyperglycemic environment that triggers unique biochemical alterations. These cellular changes occur through a number of pathways including, elevated oxidative stress [3], PKC activation [4,5], and advanced glycation end (AGE) product formation [6]. Oxidative stress is considered as a unifying mechanism that links the existing pathophysiological pathways [7]. Structural changes such as membrane thickening [8], microvascular cell loss [9], and capillary closures [10] are another contributors to the oxidative damage that are regulated by reactive oxygen species.

Information on apoptosis of neuronal cells of the retina that may occur at the early stages of diabetes has been gaining interest as primary target of diabetes changes. This is further supported by the damage to the neuronal units of retina, especially cells with fragmented DNA, which occurs within few hours [11,12]. Understanding the underlying mechanisms behind these

144

biochemical alterations associated with oxidative stress, especially at specific cellular levels, offers potential therapeutic targets that will assist in developing early diagnosis and effective treatment for DR. Thus, more studies are needed to determine the nature of these biochemical alterations in various retinal cells including the vascular cells, and their contribution to the development and progression of DR. Animal models provide a suitable model for detecting the underlying pathophysiological mechanisms of DR, which is not fully attainable by human studies [13]. Although rodent models have been proven useful for characterizing the early-stages of DR, detecting the late-stage complications of DR still remains a challenge in these models.

Fourier transform infrared (FTIR) spectrochemical imaging is a label-free and non-destructive technique that permits detecting the inherent vibrational properties of the biochemical constituents of the cells [14-16]. Spatially resolved chemical images from this technique allow the characterization of localized biochemical changes in the tissue. FTIR imaging allows rapid monitoring of early tissue alterations and can quantify the molecular changes in the tissue. Its key advantages over competing methods are its ability to measure these changes without applying exogenous labels. IR spectrochemical imaging offers unlabeled biomolecular information from sub-cellular regions of cells and tissues that can help to better understand a disease pathology and diagnosis [17-19]. FTIR imaging has been used to investigate various tissue types including prostate [20], breast [21,22], kidney [23], brain [24,25], thyroid lobectomies [26], mesothelioma [27], and colon [28].

Here I aim to determine the highly localized temporal biomolecular changes in the mouse retina induced by different duration of diabetes using IR spectroscopic imaging and chemometric tools. For this purpose, retinal tissues from Wild-Type (WT; non-diabetic) and Ins2$^{Akita/+}$ mice (Akita/+, a model of type I diabetes) at 6-week, 12-week, 6-month, and 10-month of age were

used. Individual layers of the retina, including photoreceptor layer (PRL), outer plexiform layer (OPL), inner nucleus layer (INL), and inner plexiform layer (IPL) were evaluated using a high-magnification imaging setup. Recently, I studied the oxidative stress damages to the retinal tissue in short-term diabetes (6 weeks old) and the comparison between individual retinal layers revealed that photoreceptors are the primary target for oxidative stress at the onset [29]. In this study, for the first time, I report the biochemical changes in the PRL, OPL, INL, and IPL from Akita/+ mice with different duration of diabetes, which provided novel insight into cellular specific biochemical changes associated with the development and progression of DR.

## 6.2. Materials and Methods

### 6.2.1 Sample preparation

The procedure for sample preparation has been described explicitly elsewhere [29]. Briefly, Male C57BL6 mice (Jackson Laboratories) were given a standard and housed in standard caging with 12:12 light: dark cycle and food and water provided *ad libitum*. Akita/+ mice spontaneously develop diabetes at 4-weeks of age due to a mutation in their insulin gene. The Akita spontaneous mutation (commonly referred to as MODY; Maturity-Onset Diabetes of the Young) is an autosomal dominant mutation in the insulin II gene (Ins2). Ins2 $^{Akita/+}$-C57BL/6 diabetic mice develop retinal vascular pathology characteristic of the early stages of DR. Once sacrificed, eyes were enucleated from male WT and Akita/+ mice at 6-week (n=6), 12-week (n=8), 6-month (n=6), and 10-month (n=6) of age. Eyes were rapidly frozen in isopentane cooled to almost freezing in liquid nitrogen and later stored at -80°C freezer for FTIR microspectroscopy.

Eyes were embedded in optimal cutting medium (O.C.T) compound and carefully cut into 8 μm thin sections using a cryomicrotome. Sectioning started from the optic nerve (from the back

146

of the eye) and the retinas were extracted using a thin paintbrush. The temperature inside the cryomicrotome was maintained (between -15 °C and -20 °C) and the blade was pre-chilled for at least half an hour prior to sectioning. From each eye, at least 5 retina sections were collected and mounted on the mid-IR BaF$_2$ substrate. All sections were stored in darkness and kept frozen at −80°C until FTIR measurements. Before the experiment, the sample was removed from the freezer and desiccated. The experiment was performed in dark and low humidity condition. Schematic of the methodology has been shown in the previous chapter in Figure 5.1.

### 6.2.2. FTIR wide field imaging

The FPA-FTIR chemical images were recorded with the use of a Bruker vertex 70 IR spectrometer coupled with a Bruker Hyperion 3000 IR microscope. Hyperspectral images (x, y, Abs (λ)) were acquired by means of the focal plane array (FPA) detector, which is a multielement detector and it is coupled with the interferometer. The measurements were performed using a 36× Cassegrain microscope objective and a 15× condenser aperture. This experimental geometry allows us for high magnification imaging capabilities with a $1.1 \times 1.1$ μm$^2$ pixel size and a $70 \times 70$ μm$^2$ FOV. I used 2048 scans co-added at a spectral resolution of 4 cm$^{-1}$ with a zero filling factor 2 for background and for sample acquisitions, respectively. To cover a larger area of the tissue, 4 adjacent tiles were measured by mapping across the section of the retina. The FPA size for the measurements was set to 64×64 pixels; therefore, 4096 individual spectra in the mid-IR wavelength range 3800-900cm$^{-1}$ (every pixel contains an IR spectrum) were collected per single tile measurement.

### 6.2.3. Spectral pre-processing

Resultant spectra from tissues revealed Mie scattering distortions. This distortion originates from the scattering of IR light from particles with diameters in the range of 2-20 μm [30,31]. Although the dispersion artefact appears as a derivative shape in the spectral region close to the protein band (Amide I band), this phenomenon could influence spectrum in several spectral regions, and leads to misinterpretation of the chemistry and pathology. In this study, nearly 82,000 individual pixel spectra from each animal were generated and were subjected to the RMies-EMSC scattering correction algorithm to alleviate the contribution of the scattering effect. High-throughput computations of hundreds of thousands of spectra were supported by Graphics Processing Units (GPUs) for fast hyperspectral processing [32]. Once corrected, the spectra were quality tested and preprocessed as follows. The spectra were truncated to 900-1800 cm$^{-1}$ range (finger print region) that resulted in 485 data points. Pixel binning (2×2; average of 4 pixels) was applied, which was necessary to increase the signal to noise ratio, and S/N in every spectrum was then systematically evaluated using an in-house written code in Matlab. All spectra were vector-normalized and baseline corrected (a linear baseline correction) using Matlab_R2016a prior to computational analysis.

### 6.2.4. Multivariate and statistical analysis

Multivariate analysis with principal component analysis (PCA) followed by Linear discriminant analysis (LDA) was performed using in-house written code in Python to extract maximum chemical information attributed to the variance in the spectra. PCA is an unsupervised method to decompose a dataset into bilinear latent variables called principal components (PCs) and every absorbance spectrum is replaced by a single score value for each derived PC. This

reduces the dimensionality of the data while retaining most of the information in the data set. Here, PCA was used for dimensionality reduction and then the output was loaded into LDA. LDA is a supervised method that allows labeling the classes or cell types distinguished by PCA. Assigning data to multiple classes enables an algorithm to determine the sources of within-class and between-class variances in the dataset. The outcome of PCA-LDA is an improved classification between spectra by maximizing between-class variances (mostly attributed to disease) and minimizing within-class variances (mostly attributed to tissue heterogeneity). Two sets of information were generated from PCA-LDA. Scores scatter plot that shows the separation of scores along each axis and cluster vector plot that demonstrates the coefficients of linear combinations as a function of wavenumbers. The details of PCA-LDA construction and the interpretation of results are described elsewhere [33]. The spectral region 1800-900 cm$^{-1}$ (biochemical region) was used for the analysis of spectra. Multivariate analysis was performed using "R" package (version 3.1.2), Matlab_R2016a and Python_2.6 version.

One-way ANOVA with Tukey's test as a post hoc test was employed for two-group comparisons, to determine whether there is a significant difference in the means of the groups. Quantitative results were studied as means ± standard error of means (SEM) and P values equal or less than 0.05 were accepted as a significant level of difference between WT and the Akita/+ samples. The statistical analysis was performed in SAS software.

Support Vector Machine (SVM) classifier is a machine-learning algorithm for two-class problems that is based on non-linear transformation to provide classification. SVM separates the dataset into classes by building a high-dimensional hyperplane and the accuracy of classification highly depends on the parameters that describe hyperplane. SVM uses a kernel function for mapping the data into a new dimension. The SVM was performed in " R" using package

149

"e1071" and sensitivity and specificity values, positive predictive value (PPV), negative predictive value (NPV), and classification accuracy rate were obtained. The number of spectra for each tissue type, and the parameters from SVM were reported in Figure 6.1.

### 6.2.5. Molecular factors

The ratio of the integrated area of the spectral region attributed to C-O, C-C, and C-O-C stretches (1180-950 cm$^{-1}$) to the integrated area of the amide II band (1540 cm$^{-1}$) of proteins was calculated. The former spectral region entails significant vibrational modes of sugar moieties, phosphates, and glycation products. This ratio indicates the degree of glycation in the retinal layers [34,35]. The relative alteration in the structure of amide groups of proteins was calculated as a ratio of the integrated area of amide I band (1600-1700 cm$^{-1}$) normalized to the total amide I and amide II profile (1500-1700 cm$^{-1}$). The changes in this ratio provide information about the modifications in the secondary structure of proteins [36]. The degree of unsaturation in the lipid chains was assessed by calculating the ratio of the area of the olefinic band (2992-3020 cm$^{-1}$) to the C-H region (2830-2980 cm$^{-1}$), mainly dominated by saturated lipids. This ratio indicates the relative content of unsaturated lipids and double bonds in the lipid structure of the tissue [37]. The spectral regions 1500-1750 cm$^{-1}$ (for amide I and II bands), 950-1180 cm$^{-1}$ (for C-O, C-C, and C-O-C bands), and 2800-3050 cm$^{-1}$ (for olefinic and C-H bands) were used as a baseline region.

### 6.3. Results

### 6.3.1. Classification between retinal tissues from WT and Akita/+ mice

A section of retinal tissue stained with hematoxylin and eosin (H&E) was used to show the microstructural organization of the retinal tissue [14] (Fig. 6.1A). Bright-field image (Fig. 6.1B)

and chemical image (Fig. 6.1C) of the retinal tissue from an Akita/+ mouse oriented vertically from the choroid to the ganglion cell layer are shown. As demonstrated (Fig. 6.1C), a mosaic image covers the area of $\approx 70 \times 280$ μm$^2$ (1 mosaic, $1 \times 4$ tiles (each tile = $64 \times 64$ pixels), pixel resolution: 1.1μm), and integrated over the lipid band at 2850 cm$^{-1}$ to highlight the individual retinal layers. Chemical image (Fig. 6.1C) is overlaid with the sketch of photoreceptor system including rod cells, mitochondria, and nucleus. Processed images of the retinal tissue at different wavenumbers and absorption spectra from multiple layers of the retinal tissue are unequivocally discussed elsewhere [14].

Average of nearly 16,000 individual pixel spectra generated from the whole tissue and the corresponding second derivative spectra (Savitzky-Golay algorithm, 9 smoothing points) in the biochemical mid-IR spectral region (1800-900cm$^{-1}$) are shown (Fig. 6.1.D). The biomolecular assignment of the bands for the retinal tissue has been shown in our previous study [29]. Next, retinal tissues prepared from WT and Akita/+ mice were compared (Fig. 6.1E).
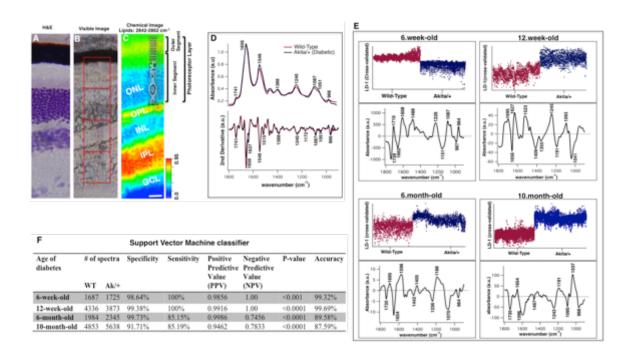
Figure 6.1: H&E stained [reprinted with permission from [14]] (A), Bright-field (B), and FTIR chemical image (C) of retinal tissue from Akita/+ mouse highlighting the microstructure of retina. FTIR image covers the area of ≈ 70 × 270 μm$^2$ (1 mosaic, 4 tiles (each tile = 64 × 64 pixels)), integrated over the lipid band at 2850 cm$^{-1}$ (baseline: 2842–2862 cm$^{-1}$) to show lipid distribution. Panel C has been overlaid with the sketch of the photoreceptor system of the retina including rods, mitochondria, and the nucleus. The scale bar is 20 μm and the color scale is from blue (low) to red (high). D) Average spectra and the corresponding second derivative spectra of retinal tissues from wild-type and Akita/+ mice in the spectral range 1800–900 cm$^{-1}$ are shown. An average of ≈16000 individual pixel spectra is demonstrated. E) Comparison of WT and Akita/+ retinal tissue at 6.week, 12.week, 6.month, and 10.month of diabetes, generated from PCA–LDA. One-dimensional cross-validated scores plot and the corresponding cluster vector plot highlighting differentiating bands are demonstrated for each stage of diabetes. F) Comparison of WT and Akita/+ retinal tissue at different ages of diabetes from support vector machine classifier. (Aboualizadeh et al., submitted for publication.)

| 6-week-old (cm$^{-1}$) | 12-week-old (cm$^{-1}$) | 6-month-old (cm$^{-1}$) | 10-month-old (cm$^{-1}$) | Assignment |
|---|---|---|---|---|
| 1739 | | 1735 | 1735 | Lipids: C=O ester in phospholipids |
| 1710 | | | | Nucleic acids: Base pair carbonyl (C=O), nucleic acids, DNA, RNA, oxidation of cellular lipids, fatty |

| | | | | |
|---|---|---|---|---|
| | | | | acids |
| | 1695 | 1695 | | Proteins: Amide I- Antiparallel $\beta$-sheet |
| 1662 | | | | Proteins: Amide I- turns $3_{10}$ helical structure of proteins (mainly C-O stretching; contribution from C-N stretching) |
| | 1656 | 1654 | 1654 | Proteins: Amide I- α-helical structure |
| | 1627 | | | Proteins: Amide I- β-sheet structure |
| 1608 | | | | Proteins: Amide I- aggregated strands |
| | | | 1596 | Proteins: Amide II- mainly N-H bending |
| 1550 | | | | Proteins: Amide II (N-H bending; C-N stretching) |
| | 1523 | | | Proteins: Amide II- β-sheet structure |
| | | 1442 | | Lipids: $CH_2$ bending |
| | 1409 | 1405 | | Lipids: C-H deformation |
| | 1355 | | | Stretching C-O, deformation C-H, deformation N-H |
| 1226 | 1245 | 1236 | 1243 | Nucleic acids: Phosphates: $\nu_{asym}$ $PO^{2-}$ |
| | 1191 | | 1195 | Phosphate (P=O) band; collagen |

| | | | | |
|---|---|---|---|---|
| | | 1188 | | Deoxyribose |
| 1151 | | | | C-O, C-C stretching, C-O-H, C-O-C deformation of carbohydrates |
| 1087 | 1093 | | 1095 | Nucleic acids: phosphates: $\nu_{sym}$ $PO^{2-}$ |
| | | 1070 | | C-O stretching, deoxyribose/ribose, DNA, RNA |
| 1051 | | | | C–O stretching, deoxyribose/ribose DNA, RNA |
| | 1041 | | 1037 | C–O stretching, ribose |
| 987 | | | | Nucleic acids and proteins, protein phosphorylation, $OCH_3$ (polysaccharides-cellulose) |
| 964 | | 964 | 968 | Nucleic acids, symmetric $PO^{4-}$ stretching (DNA) and deoxyribose; phosphate skeletal motions |

**Table 6.1.** Distinguishing wavenumbers (cm$^{-1}$) from PCA-LDA and associated biomolecular assignments when the entire retinal tissue (including all retinal layers) from WT and Akita/+ mice was compared at 6.week, 12.week, 6.month, and 10.month of diabetes.[36-39]

Individual pixel IR spectra from the whole retinal tissue covering the PRL, OPL, INL and IPL were used for comparison. Fig. 6.1E shows the PCA-LDA score plots indicating a clear separation between the two groups of interest, namely WT and Akita/+ at 6-week, 12-week, 6-month, and 10-months of diabetes. The PCA-LDA cluster vector plots (Fig. 6.1E) revealed the

154

major discriminating wavenumbers responsible for the classification between the tissues at each stage of diabetes.

The list of differentiating bands in the carbohydrates, lipids, and protein regions, between WT and Akita/+ tissues and their biomolecular assignments are summarized in Table 6.1. Fig. 6.2F displays the results from support vector machine (SVM) classifier that was performed on the spectra from WT and Akita/+ retina with different duration of diabetes. Using a SVM classifier for IR spectra from retinal tissues, an accuracy of 87.59% (10-month), 89.58% (6-month), 99.69% (12-week) and 99.32% (6-week) was achieved. The number of spectra used for the comparison and the classification parameters are listed in Fig. 6.1F.
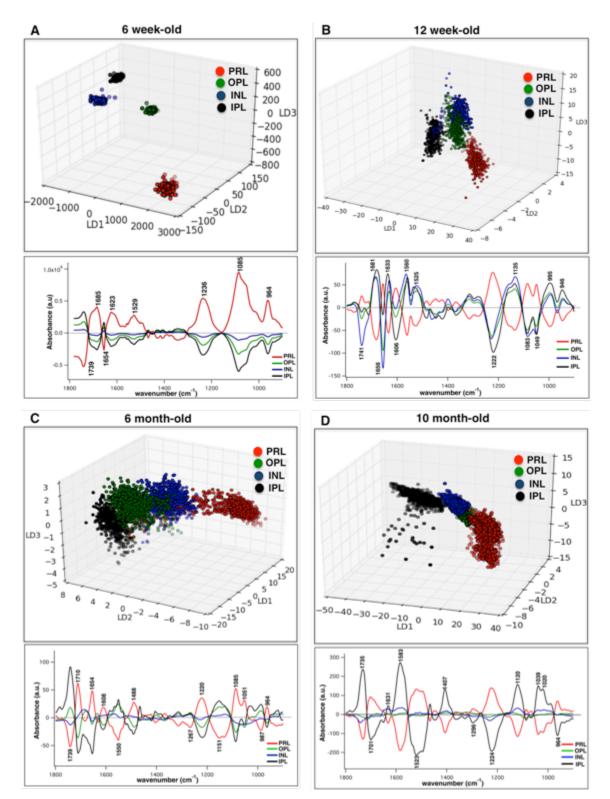
**Figure 6.2**: Comparison of distinctive diabetic retinal layers, namely PRL, OPL, INL, and IPL at 6.week (A), 12.week (B), 6.month (C), and 10.month (D) of diabetes derived from PCA-LDA. Three-dimensional rotated scores plot and cluster vector plot highlighting discriminatory wavenumbers are demonstrated for each case study. Nearly 1500 spectra from each layer of the retina, and for each stage of diabetes, were generated and compared. (Aboualizadeh et al., submitted for publication.)

156

| 6-week-old ($cm^{-1}$) | 12-week-old ($cm^{-1}$) | 6-month-old ($cm^{-1}$) | 10-month-old ($cm^{-1}$) | Assignment |
|---|---|---|---|---|
| 1739 | 1741 | 1739 | 1735 | Lipids: C=O ester in phospholipids |
|  |  | 1710 |  | Base pair carbonyl (C=O), nucleic acids, DNA, RNA, oxidation of cellular lipids, fatty acids |
|  |  |  | 1701 | Lipids: C=O ester |
| 1685 | 1681 |  |  | Proteins: Amide I- turns or antiparallel $\beta$-sheet structure (mainly C-O stretching) |
|  | 1656 | 1654 |  | Proteins: Amide I- α-helical structure |
|  | 1633 |  | 1631 | Proteins: Amide I: β-sheet structure |
| 1623 |  |  |  | Proteins: Amide I- aggregated strand structures (mainly C-O stretching) |
|  |  | 1608 |  | Proteins: Amide I-aggregated strands |
|  |  |  | 1583 | Proteins: Amide II- mainly N=H bending, ring C-C stretch of phenyl |
|  | 1560 | 1550 |  | Proteins: Amide II- mainly N-H bending |
| 1529 | 1525 |  | 1523 | Proteins: Amide II- mainly C=N, C=C stretching |
|  | 1488 |  |  | Lipids: C-H deformation |
|  |  |  | 1407 | Lipids: C-H deformation |
|  |  |  | 1296 | Proteins: Amide III, mainly N-H bending |
|  |  | 1267 |  | Proteins: Amide III, mainly N-H bending |
| 1236 | 1222 | 1220 | 1224 | Nucleic acids: phosphates: $\nu_{asym} PO^{2-}$ |
|  |  | 1151 |  | C-O, C-C stretching, C-O-H, C-O-C deformation of carbohydrates/ glycogen |
|  | 1135 | 1135 |  | C-O, C-C stretching, RNA ribose |

157

| | | | | |
|---|---|---|---|---|
| | | | 1120 | C-O stretching, RNA ribose |
| 1085 | 1083 | 1085 | | Nucleic acids: phosphates: $\nu_{sym}\ PO_2^-$ |
| | 1049 | 1051 | | C–O stretching, deoxyribose/ribose DNA, RNA |
| | | | 1039 | C–O stretching, ribose |
| | | | 1020 | C-O, C-C stretching, DNA, glycogen, |
| | 995 | | | C-O ribose, C-C, RNA |
| | | 987 | | Nucleic acids and proteins, protein phosphorylation, OCH$_3$ (polysaccharides-cellulose) |
| 964 | 964 | 964 | 964 | Nucleic acids, symmetric $PO_4^-$ stretching (DNA) and deoxyribose; phosphate skeletal motions |

**Table 6.2.** Distinguishing wavenumbers (cm$^{-1}$) from PCA-LDA and associated biomolecular assignments for the comparison of distinctive diabetic retinal layers (PRL, OPL, INL, and IPL) at 6.week, 12.week, 6.month, and 10.month of diabetes. [36-39]


### 6.3.2. Intra-retinal layer classification at each stage of diabetes

To gain a better understanding of the diabetes-induced impacts on distinctive retinal layers, a comparison was made between the diabetic PRL, OPL, INL and IPL with different duration of diabetes. IR spectra were derived from characteristic layers of diabetic tissues and compared using PCA-LDA. Figure 6.2 shows three-dimensional rotated score plots comparing diabetic retinal layers at 6-weeks (6.2.A), 12-weeks (6.3.B), 6-months (6.2.C), and 10-months (6.2.D) of diabetes after PCA-LDA of IR spectra from retinal layers and the corresponding loading plots that exhibit the major discriminating frequencies responsible for classification. Segregation with an excellent degree between the diabetic retinal layers was achieved; however, the best

classification between the retinal layers was achieved at 6 weeks of diabetes (Fig. 6.2A). Table 6.2 lists the major wavenumbers with their tentative biomolecular assignments associated with the classification.
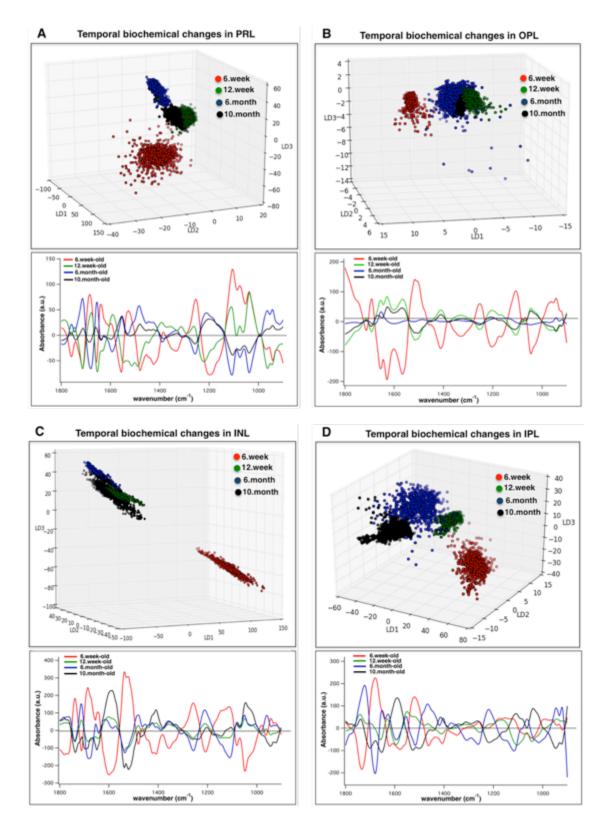
159

**Figure 6.3:** Temporal diabetes-induced biochemical alterations in individual retinal layers generated from PCA-LDA. Biochemical changes in the PRL (A), OPL (B), INL (C), and IPL (D) as diabetes progresses are shown. Three-dimensional rotated scores plot and cluster vector plot for each case are demonstrated. (Aboualizadeh et al., submitted for publication.)

160

### 6.3.3. Temporal biochemical changes for each retinal layer

To ascertain the molecular and cellular alterations in individual retinal layers as diabetes progresses, I investigated biochemical changes from multiple duration of diabetes, for each layer of the retina from Akita/+ mice, using PCA-LDA. IR spectra were compared from each retinal layer at 6-week, 12-week, 6-month, and 10-month of diabetes. Temporal-dependent three-dimensional rotated score plots and attributed loading plots from the comparison of the PRL (Fig. 6.3A), the OPL (Fig. 6.3B), the INL (Fig. 6.3C), and the IPL (Fig. 6.3D) are displayed. As shown in Fig. 6.3, spectra from short-term diabetes (6 week-old) present a clear segregation from the other stages of diabetes, for all retinal layers studied here. Table 6.3 lists the main wavenumbers with their biomolecular assignments associated with the classifications.

| PRL (cm$^{-1}$) | OPL (cm$^{-1}$) | INL (cm$^{-1}$) | IPL (cm$^{-1}$) | Assignment |
|---|---|---|---|---|
| 1758 | | | | Lipids: C=C stretching |
| 1741 | | 1739 | 1741 | Lipids: C=O ester in phospholipids |
| 1712 | | 1710 | | Base pair carbonyl (C=O), nucleic acids, DNA, RNA, oxidation of cellular lipids, fatty acids |
| | 1693 | 1691 | | Proteins: Amide I- Antiparallel $\beta$-sheet |
| 1681 | | 1683 | | Proteins: Amide I- turns or antiparallel β-sheet structure (mainly C-O stretching) |
| 1677 | | | 1679 | Proteins: Amide I- turns structure (mainly C-O stretching) |
| 1656 | 1654 | 1654 | 1654 | Proteins: Amide I- α-helical structure |
| 1637 | 1629 | | | Proteins: Amide I: β-sheet structure |

| | | | | |
|---|---|---|---|---|
| 1593 | | | 1594 | Proteins: Amide II- mainly N-H bending |
| | 1566 | | | Proteins: ring base, phenyl, aromatics |
| 1556 | | | 1550 | Proteins: Amide II- mainly N-H bending |
| | | 1537 | | Proteins: Amide II- $\alpha$-helical structure |
| | | | 1521 | Proteins: Amide II- $\beta$-sheet structure |
| | 1510 | | | Proteins: Amide II, chain $\beta$-sheet structure C=C stretching, aromatics |
| 1481 | | 1483 | | Lipids: C-H deformation |
| | 1401 | | | Bending mode of $CH_3$ |
| 1255 | 1250 | 1255 | | Proteins: Amide III- mainly N-H bending, C-N stretching |
| 1222 | | | 1220 | Phosphates: $\nu_{asym} PO^{2-}$ |
| | 1204 | 1207 | | Collagen, C-C stretching, C-H bending, $\nu_{asym} PO^{2-}$ |
| 1191 | | | | Vibrational modes of collagen, phosphate band |
| 1103 | 1105 | 1110 | 1107 | Carbohydrates, C-O, C-C stretching, $\nu_{sym} PO^{2-}$ |
| 1072 | | | | Phosphates: $\nu_{sym} PO^{2-}$ |
| | 1045 | 1047 | 1043 | Carbohydrates, C-O stretching, glycogen, DNA, RNA |
| 1037 | | | | Carbohydrates, C–O stretching |
| | | 983 | | Nucleic acids and proteins, protein phosphorylation, $OCH_3$ (polysaccharides-cellulose) |
| 964 | | | | Nucleic acids, symmetric $PO^{4-}$ stretching (DNA) and deoxyribose; phosphate skeletal motions |
| | 943 | | 946 | Deoxyribose |

**Table 6.3.** Temporal-dependent distinguishing wavenumbers (cm$^{-1}$) from PCA-LDA and associated biomolecular assignments for each diabetic retinal layer (PRL, OPL, INL, and IPL) at different duration of diabetes. The biochemistry of each retinal layer is delineated as diabetes develops. [36-39]

### 6.3.4. Molecular factors

As shown (Fig. 6.4 A-F), we computed the spectral metrics (see methods for details) for each retinal layer as a function of diabetes duration to determine the significant relative variations in the macromolecular functional groups between non-diabetic and diabetic mice. The first metric was the ratio of integrated absorbance between 950 and 1180 cm$^{-1}$ (C-O, C-C, C-O-C stretches) to the integrated absorbance between 1510 and 1570 cm$^{-1}$ (amide II). This metric was used to show the degree of glycation in retinal layers. For all retinal layers and all diabetes durations, this ratio was greater in diabetic groups compared with WT groups (Fig. 6.4 A), although some of the differences were not significantly different. The second metric was the ratio of integrated absorbance between 1600 and 1700 cm$^{-1}$ (amide I-proteins) to the integrated absorbance of total amide I and amide II groups between 1500 and 1700 cm$^{-1}$. This metric was used to show the relative variations in the amide groups of proteins in retinal layers. Statistical analysis revealed that this ratio at 6 and 12 weeks of diabetes was significantly greater for the non-diabetic PRL, OPL, and INL compared to the corresponding layers in Akita/+ group (Fig. 6.4 C). This ratio was significantly larger in the diabetic IPL at 6 weeks in comparison with WT group. This metric was not significantly different between the layers of WT and Akita/+ mice at 6 months of age.

The last metric was the ratio of integrated absorbance between 2992 and 3020 cm$^{-1}$ (CH=CH) to the integrated absorbance between 2830 and 2980 cm$^{-1}$ (mainly C-H stretches of lipids). This metric was used to show the relative variations in the double bonds in lipid chains within retinal layers. This metric revealed a decrease in all diabetic layers compared to the WT group at the

age of 6 weeks (Fig. 6.4 E). At 12 weeks, this metric was greater in the diabetic OPL and IPL; however, there was no significant difference between the WT and diabetic PRL and INL at this age. At the ages of 6, and 10 months, diabetic PRL was the only layer with the greater level of this metric in comparison with WT layers.

The time-lapse trends were shown for all three metrics (Fig. 6.4 B,D,F), calculated for individual diabetic and non-diabetic retinal layers, as a function of diabetes duration. The trends facilitate an understanding of the temporal-dependent variations in molecular parameters of retinal layers.
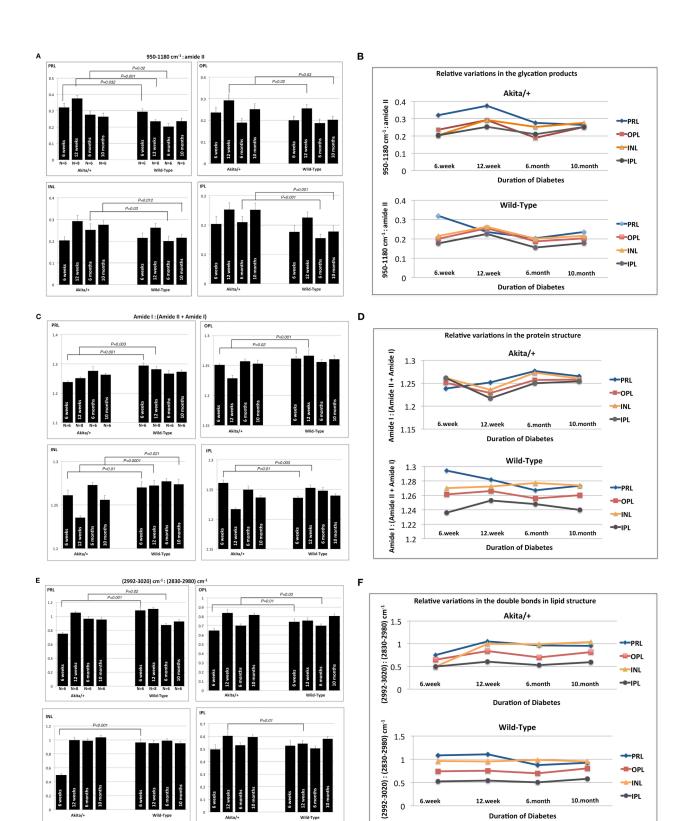
**Figure 6.4**: Bar graphs of the ratio of several IR band areas including glycation level (A), protein content (C), and unsaturation level (E) at 6.week, 12.week, 6.month, and 10.month of diabetes, are demonstrated. A comparison was made between the WT and Akita/+ mice for each retinal layer at different duration of diabetes. All graphs show the average of at least six replicates with error bars indicating SEM. * was used to show the level of significance (P < 0.05). Time-dependent trends for the PRL, OPL, INL, and IPL, highlighting the variations in the glycation level (B), protein content (D), and unsaturation level (F) during diabetes, are displayed. (Aboualizadeh et al., submitted for publication.)

## 6.4. Discussion

In the present work, I highlighted the bio-molecular changes of retinal layers, and their potential contribution to pathogenesis of DR, with different duration of diabetes. Precise temporal biomarkers of oxidative stress in the retina with sub-cellular spatial resolution level were obtained and the specific macromolecular functional groups associated with the damage were delineated. Our approach integrates spatially resolved chemical imaging and multivariate analysis to determine the intra-retinal layer bio-molecular changes from the onset to late diabetes (Fig. 6.2). With short duration of diabetes (6 and 12 weeks), the PRL showed a conspicuous segregation from the rest of the layers (Fig. 6.2 A, B), while the separation between layers looked more clustered with longer duration of diabetes (6 and 10 months) (Fig. 6.2 C, D).

The data presented here clearly show that the FTIR-based methods can identify and distinguish between WT and diabetic tissues at early and later stages of diabetes, which has not been previously achieved. In a recent paper [29], I resolved short-term diabetes-induced heterogeneous morphology in the size range of 10-20 μm within the nucleus segment of photoreceptors by means of high-resolution (74× objective; NA 0.65) synchrotron-based chemical imaging with oversampling [43]. One of the limitations with this study was employing the conventional globar source, which does not provide sufficient brightness to resolve subtle

166

morphological heterogeneities in the diabetic tissue. However, the specific spectral biomarkers were achieved in a precise manner. Future studies will concentrate on the employment of synchrotron source in detecting temporal morphological alterations in diabetic retinal tissue in the anticipation that this approach may yield alternative and potentially complementary methods for the assessment of diabetes changes.

Our novel approach integrates spatially resolved chemical images and multivariate analysis for studying individual layers of retina in order to determine diabetes-induced biochemical alterations in the retinal layers from the onset to the late stage of diabetes (Fig. 6.2). PCA-LDA revealed a robust classification between the retinal layers at different duration of diabetes and an attributed biomolecular change at each stage, were reported (Table 6.2). At earlier stages of diabetes (6-week and 12-week), the PRL showed a conspicuous segregation from the rest of the layers (Fig. 6.2 A,B), while the separation between retinal layers looked more entangled at the later stages (6-month and 10-month) (Fig. 6.2 C,D).

The significance of photoreceptor changes in the pathogenesis of early DR [44,45] and the contribution of mitochondria in diabetes-induced oxidative damage is well studied [46]. One of the promising features of these results is the capacity to ascertain the macromolecules that promote retinal changes. Important biomarkers at 6 weeks were associated with the stretches and skeletal motions of phosphates, the main spectral markers of ds-DNA. However, the discriminatory features between retinal layers at 12 weeks were mostly attributable to the amide I and amide II of α-helical and β-sheet structure of proteins (Table 6.2). Intra-retinal layer biomolecular changes at 6 and 10 months of diabetes were mostly attributed to C-O, C-C, and C-O-C stretches of carbohydrates, DNA, RNA ribose, and glycogen as well as several biomarkers in the secondary structure of proteins. Here biochemical changes in the protein structures with

longer duration of diabetes may resonate with the extracellular and intracellular changes induced by glycation reactions via chemical rearrangement. The glycation products built on amino groups of proteins, and in DNA can lead to molecular cross-links.

Here for the first time, I studied the biochemical changes of each layer of retina from mice with different duration of diabetes to better assess the development and progression of DR (Fig. 6.3). This is a potentially important finding that may be of particular benefit to understand the molecular and biological activity of retinal cells in response to oxidative stress during diabetes, which still remains unclear. When the diabetic retinal layers were studied, the spectra from 12 weeks, 6 months, and 10 months were adjacent clusters in the scores plot; however, the spectra from 6 weeks revealed a clear separation (Fig. 6.3). This finding implies the uniqueness of damage and the highest impact at 6 weeks within the layers of retina from diabetic mice. Classification between the spectra from IPL at different durations of diabetes (Fig. 6.3D) revealed major biomarkers attributable to α-helical and β-sheet structures of proteins that suggest the significance of protein changes in this layer with progression of diabetes. These bio-molecular changes may have significant impact on retinal neuronal function early in diabetes.

The ratio between the areas of bands associated with C-O, C-C, and C-O-C to amide II group in proteins provides information on the molecular modifications in the glycation products. I found that this ratio was significantly greater for the PRL in retinas from 6 weeks, 12 weeks, and 6 months diabetic mice. However, this ratio was significantly larger for the OPL at 12 weeks and 10 months of diabetes (Fig. 6.4A). For the INL and IPL, this metric was significantly greater at 6 and 10 months of diabetes, which suggests the impacts of the glycation products within these layers late in diabetes. Time-lapse variations in this ratio, for all diabetic layers, revealed an increase from 6 to 12 weeks, and then a decrease at 6 months followed by another increase at 10

months of diabetes (Fig. 6.4 B). Excessive production of ROS during diabetes leads to an imbalance in these byproducts of metabolism, and increased oxidative stress. One of the major tasks of the cell's compensatory mechanisms is the repair of the oxidatively damaged or degraded macromolecules. Molecular ROS-scavengers, enzymatic antioxidants, and proteins that help the repair machinery are the known defense mechanisms. Temporal trend of variations in the glycation level at different durations of diabetes in our data may correlate with the antioxidative mechanisms of retinal cells in response to progression of diabetic changes.

The area ratio between amide I and (amide I + amide II) bands sheds light on structural variations in proteins within retinal layers. In the plexiform layers of diabetic retina, this ratio did not exhibit any significant change from 6 to 10 months of diabetes; however, the nuclear bodies of diabetic retina revealed a decrease from 6 to 10 months (Fig.6.4 C,D). For diabetic retinal layers, I found that this metric reached a low at 12 weeks and a peak at 6 months; however, the PRL reached a minimum at 6 weeks of diabetes. One possible biological source of these alterations is the AGEs that are found in the extracellular matrix and that potentially modify the matrix proteins impairing matrix-matrix and matrix-cell interactions [48]. Another source of damage are the intracellular proteins, where the formation of AGE has direct impact on their function. Specific binding of the AGE modified proteins to the receptor of AGE has the potential to damage [49,50]. The most interesting result to emerge from the relative changes in glycation products and the variations in the amide groups of proteins, is that these ratios exhibit nearly the same value for all diabetic retinal layers at 10 months, which states the uniformity of the damage to all the layers with longer duration of diabetes.

The modifications in the unsaturated bonds in lipids was evaluated from the area ratio between C=H (double bonds) and C-H stretching region. Investigation of this ratio in the diabetic

169

PRL, OPL, INL, and IPL (Fig. 6.4 E,F) suggests the significance of hydrocarbon chain unsaturation in short duration of diabetes (6 and 12 weeks). The decrease in this ratio in diabetic retinal layers, suggests the loss of unsaturated acyl chains of lipids due to an elevated lipid peroxidation in diabetic retina. The oxidation of unsaturated fatty acids is well established and poly-unsaturated fatty acids are more susceptible to peroxidation due to the number of double bonds [51]. Our results are in agreement with several studies with short-duration of diabetes-mediated changes in retinal fatty acid metabolism [52,53], which revealed a significant decrease in unsaturation of lipids in diabetic retina.

## 6.5. Concluding remarks

In summary, this is the first study to report the nature of diabetes-mediated molecular changes in the biochemistry of distinctive layers of mouse retina. The function of cell types in the retina and their role in the pathogenesis of DR has not been yet clearly delineated. Our results demonstrate the susceptibility of the neuro-retina as an early potential target of changes brought about by hyperglycemic environment associated with diabetes. The persistence of these changes during chronic diabetes leads to progression of the disease and ultimately loss of vision. These findings provide a significant rationale for the development of further studies of the role of retinal neuronal cells in the pathogenesis of DR. Findings from this work offer substantial mechanistic insight into the diabetes-induced changes in the neuro-retina, which may shed light into the early diagnosis, prognostication and treatment of DR.

## 6.5. References

1. Prasad, S., Kamath, G. G., Jones, K., Clearkin, L. G., & Phillips, R. P. (2001). Prevalence of blindness and visual impairment in a population of people with diabetes. Eye, 15, 640-643.

2. Yun, W. L., Acharya, U. R., Venkatesh, Y. V., Chee, C., Min, L. C., & Ng, E. Y. K. (2008). Identification of different stages of diabetic retinopathy using retinal optical images. Information Sciences, 178(1), 106-121.

3. Kowluru, R. A. (2001). Diabetes-induced elevations in retinal oxidative stress, protein kinase C and nitric oxide are interrelated. Acta Diabetologica, 38(4), 179-185.

4. Stauble, B., Boscoboinik, D., Tasinato, A., & Azzi, A. (1994). MODULATION OF ACTIVATOR PROTEIN-1 (AP-1) TRANSCRIPTION FACTOR AND PROTEIN-KINASE-C BY HYDROGEN-PEROXIDE AND D-ALPHA-TOCOPHEROL IN VASCULAR SMOOTH-MUSCLE CELLS. European Journal of Biochemistry, 226(2), 393-402.

5. Ishii, H., Koya, D., & King, G. L. (1998). Protein kinase C activation and its role in the development of vascular complications in diabetes mellitus. Journal of Molecular Medicine-Jmm, 76(1), 21-31.

6. Beisswenger, P. J., Howell, S. K., Smith, K., & Szwergold, B. S. (2003). Glyceraldehyde-3-phosphate dehydrogenase activity as an independent modifier of methylglyoxal levels in diabetes. Biochimica Et Biophysica Acta-Molecular Basis of Disease, 1637(1), 98-106.

7. Baynes, J. W. (1991). ROLE OF OXIDATIVE STRESS IN DEVELOPMENT OF COMPLICATIONS IN DIABETES. Diabetes, 40(4), 405-412.

8. Stitt, A. W., Anderson, H. R., Gardiner, T. A., & Archer, D. B. (1994). DIABETIC-RETINOPATHY - QUANTITATIVE VARIATION IN CAPILLARY BASEMENT-MEMBRANE THICKENING IN ARTERIAL OR VENOUS ENVIRONMENTS. British Journal of Ophthalmology, 78(2), 133-137.

9. Barot, M., Gokulgandhi, M. R., Patel, S., & Mitra, A. K. (2013). Microvascular complications and diabetic retinopathy: recent advances and future implications. Future Medicinal Chemistry, 5(3), 301-314.

10. Madsen-Bouterse, S. A., & Kowluru, R. A. (2008). Oxidative stress and diabetic retinopathy: Pathophysiological mechanisms and treatment perspectives. Reviews in Endocrine & Metabolic Disorders, 9(4), 315-327.

11. Zeng, X. X., Ng, Y. K., & Ling, E. A. (2000). Neuronal and microglial response in the retina of streptozotocin-induced diabetic rats. Visual Neuroscience, 17(3), 463-471.

12. Asnaghi, V., Gerhardinger, C., Hoehn, T., Adeboje, A., & Lorenzi, M. (2003). A role for the polyol pathway in the early neuroretinal apoptosis and glial changes induced by diabetes in the rat. Diabetes, 52(2), 506-511.

13. Lai, A. K. W. & Lo, A. C. Y. (2013). Animal Models of Diabetic Retinopathy: Summary and Comparison. *Journal of Diabetes Research*.

14. Kastyak-Ibrahim, M. Z., Nasse, M. J., Rak, M., Hirschmugl, C., Del Bigio, M. R., Albensi, B. C., et al. (2012). Biochemical label-free tissue imaging with subcellular-resolution synchrotron FTIR with focal plane array detector. Neuroimage, 60(1), 376-383.15. Baker, M. J. *et al.* Using Fourier transform IR spectroscopy to analyze biological materials. *Nature Protocols* **9**, 1771-1791(2014).

16. Levin, I. W., & Bhargava, R. (2005). Fourier transform infrared vibrational spectroscopic imaging: Integrating microscopy and molecular recognition. Annual Review of Physical Chemistry, 56, 429-474.

17. Diem, M., Boydston-White, S. & Chiriboga, L. (1999). Infrared spectroscopy of cells and tissues: Shining light onto a novel subject. *Applied Spectroscopy* **53**, 148A-161A.

18. Mattson, E. C., Aboualizadeh, E., Barabas, M. E., Stucky, C. L., & Hirschmugl, C. J. (2013). Opportunities for Live Cell FT-Infrared Imaging: Macromolecule Identification with 2D and 3D Localization. International Journal of Molecular Sciences, 14(11), 22753-22781.

172

19. Barabas, M. E., Mattson, E. C., Aboualizadeh, E., Hirschmugl, C. J., & Stucky, C. L. (2014). Chemical Structure and Morphology of Dorsal Root Ganglion Neurons from Naive and Inflamed Mice. Journal of Biological Chemistry, 289(49), 34241-34249.

20. Gazi, E., Dwyer, J., Gardner, P., Ghanbari-Siahkali, A., Wade, A. P., Miyan, J., et al. (2003). Applications of Fourier transform infrared microspectroscopy in studies of benign prostate and prostate cancer. A pilot study. Journal of Pathology, 201(1), 99-108.

21. Kumar, S., Desmedt, C., Larsimont, D., Sotiriou, C., & Goormaghtigh, E. (2013). Change in the microenvironment of breast cancer studied by FTIR imaging. Analyst, 138(14), 4058-4065.

22. Zawlik, I., Kaznowska, E., Cebulski, J., Kolodziej, M., Depciuch, J., Vongsvivut, J., et al. (2016). FPA-FTIR Microspectroscopy for Monitoring Chemotherapy Efficacy in Triple-Negative Breast Cancer. Scientific Reports, 6.

23. Gulley-Stahl, H. J., Bledsoe, S. B., Evan, A. P., & Sommer, A. J. (2010). The Advantages of an Attenuated Total Internal Reflection Infrared Microspectroscopic Imaging Approach for Kidney Biopsy Analysis. Applied Spectroscopy, 64(1), 15-22.

24. Hackett, M. J., McQuillan, J. A., El-Assaad, F., Aitken, J. B., Levina, A., Cohen, D. D., et al. (2011). Chemical alterations to murine brain tissue induced by formalin fixation: implications for biospectroscopic imaging and mapping studies of disease pathogenesis. Analyst, 136(14), 2941-2952.

25. Bergner, N., Romeike, B. F. M., Reichart, R., Kalff, R., Krafft, C., & Popp, J. U. (2013). Tumor margin identification and prediction of the primary tumor from brain metastases using FTIR imaging and support vector machines. Analyst, 138(14), 3983-3990.

26. Martinez-Marin, D., Sreedhar, H., Varma, V.K., Eloy, C., Sobrinho-Simões, M., Kajdacsy-Balla, A., Walsh, M.J. (2016). Accounting for tissue heterogeneity in infrared spectroscopic imaging for accurate diagnosis of thyroid carcinoma subtypes, Vibrational Spectroscopy.

27. Großerueschkamp, F. et al. (2017). Spatial and molecular resolution of diffuse malignant mesothelioma heterogeneity by integrating label-free FTIR imaging, laser capture microdissection and proteomics. *Sci. Rep.* **7**, 44829.

28. Nallala, J., Lloyd, G. R., Shepherd, N., & Stone, N. (2016). High-resolution FTIR imaging of colon tissues for elucidation of individual cellular and histopathological features. Analyst, 141(2), 630-639.

29. Aboualizadeh, E. et al. (2017). Retinal oxidative stress at the onset of diabetes determined by synchrotron FTIR widefield imaging: towards diabetes pathogenesis. Analyst 142, 1061-1072.

30. Davis, B. J., Carney, P. S., & Bhargava, R. (2010a). Theory of Mid-infrared Absorption Microspectroscopy: II. Heterogeneous Samples. Analytical Chemistry, 82(9), 3487-3499.

31. Davis, B. J., Carney, P. S., & Bhargava, R. (2010b). Theory of Midinfrared Absorption Microspectroscopy: I. Homogeneous Samples. Analytical Chemistry, 82(9), 3474-3486.

32. Mattson, E. C., Unger, M., Clede, S., Lambert, F., Policar, C., Imtiaz, A., et al. (2013). Toward optimal spatial and spectral quality in widefield infrared spectromicroscopy of IR labelled single cells. Analyst, 138(19), 5610-5618.

33. Martin, F. L., Kelly, J. G., Llabjani, V., Martin-Hirsch, P. L., Patel, II, Trevisan, J., et al. (2010). Distinguishing cell types or populations based on the computational analysis of their infrared spectra. *Nature Protocols, 5*(11), 1748-1760.

34. Scott, D. A., Renaud, D. E., Krishnasamy, S., Meric, P., Buduneli, N., Cetinkalp, S., et al. (2010). Diabetes-related molecular signatures in infrared spectra of human saliva. Diabetology & Metabolic Syndrome, 2.

35. Potter, K., Kidder, L. H., Levin, I. W., Lewis, E. N., & Spencer, R. G. S. (2001). Imaging of collagen and proteoglycan in cartilage sections using Fourier transform infrared spectral imaging. Arthritis and Rheumatism, 44(4), 846-855.

36. Meade, A. D., Lyng, F. M., Knief, P., & Byrne, H. J. (2007). Growth substrate induced functional changes elucidated by FTIR and Raman spectroscopy in in-vitro cultured human keratinocytes. Analytical and Bioanalytical Chemistry, 387(5), 1717-1728.

37. Movasaghi, Z., Rehman, S., & Rehman, I. U. (2008). Fourier transform infrared (FTIR) spectroscopy of biological tissues. Applied Spectroscopy Reviews, 43(2), 134-179.

38. Barth, A., & Zscherp, C. (2002). What vibrations tell us about proteins. Quarterly Reviews of Biophysics, 35(4), 369-430.

39. Naumann, D. (2001). FT-infrared and FT-Raman spectroscopy in biomedical research. Applied Spectroscopy Reviews, 36(2-3), 239-298.

40. Birarda, Giovanni et al. (2013). Synchrotron Infrared Imaging of Advanced Glycation Endproducts (AGEs) in Cardiac Tissue from Mice Fed High Glycemic Diets. Biomedical spectroscopy and imaging 2, 301–315.

41. Kong, J., & Yu, S. (2007). Fourier transform infrared spectroscopic analysis of protein secondary structures. Acta Biochimica Et Biophysica Sinica, 39(8), 549-559.

42. Sills, R. H., Moore, D. J., & Mendelsohn, R. (1994). ERYTHROCYTE PEROXIDATION - QUANTITATION BY FOURIER-TRANSFORM INFRARED-SPECTROSCOPY. Analytical Biochemistry, 218(1), 118-123.

43. Nasse, M. J., Walsh, M. J., Mattson, E. C., Reininger, R., Kajdacsy-Balla, A., Macias, V., et al. (2011). High-resolution Fourier-transform infrared chemical imaging with multiple synchrotron beams. *Nature Methods, 8*(5), 413-U458.

44. Greenstein, V., Sarter, B., Hood, D., Noble, K., Carr, R. (1991). Hue discrimination and S cone pathway sensitivity in early diabetic retinopathy. *Invest Ophthalmol Vis Sci* 31, 1008-1014.

45. Du, Y., Veenstra, A., Palczewski, K., & Kern, T. S. (2013). Photoreceptor cells are major contributors to diabetes-induced oxidative stress and local inflammation in the retina. Proceedings of the National Academy of Sciences of the United States of America, 110(41), 16586-16591.

46. Nishikawa, T., Edelstein, D., Du, X. L., Yamagishi, S., Matsumura, T., Kaneda, Y., et al. (2000). Normalizing mitochondrial superoxide production blocks three pathways of hyperglycaemic damage. Nature, 404(6779), 787-790.

47. Gastinger, M.J., Singh, R. S. J. & Barber, A. J. (2006). Loss of cholinergic and dopaminergic amacrine cells in streptozotocindiabetic rat and Ins2$^{Akita}$-diabetic mouse retinas. Investigative Ophthalmology & Visual Science, 47, 3143–3150.

48. Glomb, M. A., & Monnier, V. M. (1995). MECHANISM OF PROTEIN MODIFICATION BY GLYOXAL AND GLYCOLALDEHYDE, REACTIVE INTERMEDIATES OF THE MAILLARD REACTION. Journal of Biological Chemistry, 270(17), 10017-10026.

49. Stitt, A. W. (2003). The role of advanced glycation in the pathogenesis of diabetic retinopathy. Experimental and Molecular Pathology, 75(1), 95-108.

50. Baynes, J.W. (1991). ROLE OF OXIDATIVE STRESS IN DEVELOPMENT OF COMPLICATIONS IN DIABETES. Diabetes, 40(4), 405-412.

51. Halliwell, B., & Chirico, S. (1993). LIPID-PEROXIDATION - ITS MECHANISM, MEASUREMENT, AND SIGNIFICANCE. American Journal of Clinical Nutrition, 57(5), 715-725.

52. Tikhonenko, M., Lydic, T. A., Wang, Y., Chen, W. Q., Opreanu, M., Sochacki, A., et al. (2010). Remodeling of Retinal Fatty Acids in an Animal Model of Diabetes A Decrease in Long-Chain Polyunsaturated Fatty Acids Is Associated With a Decrease in Fatty Acid Elongases Elovl2 and Elovl4. Diabetes, 59(1), 219-227.

53. Koehrer, P., Saab, S., Berdeaux, O., Isaico, R., Gregoire, S., Cabaret, S., et al. (2014). Erythrocyte Phospholipid and Polyunsaturated Fatty Acid Composition in Diabetic Retinopathy. Plos One, 9(9).

**Chapter 7: Concluding Remarks**

In the present dissertation, I aimed to provide a more comprehensive understanding of the diabetes-mediated biomolecular processes in individual retinal cells subjected to hyperglycemia. Despite extensive studies, the changes in the biochemistry of retinal layers during the development of diabetic retinopathy (DR) are not well known. Lateral and axial resolutions, depth of penetration in the eye, contrast from the imaging modalities, optical sectioning, and the incapability of early intervention, are some restraints that hindered an in-depth understanding of the pathogenesis of DR in the microscopic realm.

Spatially resolved infrared chemical imaging allows simultaneous visualization of multiple retinal layers and characterization of localized biochemical changes in the tissue without applying exogenous stains or dyes. The study of the bio-molecular alterations in the biochemistry of retinal layers at different duration of diabetes would be greatly facilitated by spectroscopic techniques without any need for isolating the cell compartments. The spectral differences between diabetic and non-diabetic retinal tissues are very subtle. In this dissertation, I have focused on developing multivariate data analysis that enables me to identify the spectral biomarkers associated with the histology.

In this study, for the first time, I demonstrate that FT-IR widefield imaging engaged with multivariate analysis is a promising approach to quantifying temporal-dependent biomolecular changes attributed to DR in distinctive layers of mouse retina. Intra-layer comparison between photoreceptor layer (PRL), outer plexiform layer (OPL), inner nuclear layer (INL), and inner plexiform layer (IPL), at different duration of diabetes was performed and the associated biomarkers were determined. Here, I also report the biochemical changes over time in the

www.manaraa.com

individual layers of retina from Akita/+ mice related to different duration of diabetes. These results provide novel insight into the cellular specific retinal changes during the development and progression of DR.

The function of cell types in the retina and their role in the pathogenesis of DR has not been yet clearly delineated. My results demonstrate the susceptibility of the neuro-retina as an early potential target of changes brought about by hyperglycemic environment associated with diabetes. The persistence of these changes during chronic diabetes leads to progression of the disease, vascular changes, and ultimately loss of vision. These findings provide a significant rationale for the development of further studies of the role of retinal neuronal cells in the pathogenesis of DR. Findings from my work offer substantial mechanistic insight into the diabetes-induced early changes in the neuro-retina, which may shed light into early diagnosis, prognostication and treatment of DR.

The mid-infrared spectroscopy thus far, combined with statistical analysis, has revealed the spectral differences between several malignant and benign tissues. However, due to the limitation with the conventional globar source in the bench top systems, there is no report on the morphological variations in the tissue caused by the disease. In this dissertation, for the first time, I reported the morphological alterations in the nucleus segment of photoreceptors occurred at the onset of diabetes by employing high-resolution synchrotron-based chemical imaging. This approach may yield alternative and potentially complementary methods for the assessment of diabetes changes.

Future directions can be focused on the MALDI imaging mass spectrometry of the retinal tissue to determine the role of proteins in individual retinal layers and the proteomic profiling of the photoreceptors. Retinal tissue is a suitable candidate for mass spectrometric studies due to it's layered structure, which enables us to study the layer of interest. Modifying the ion potentials and light-responsive proteins in the individual retinal neurons via optogenetic, and then measuring the infrared signals from those cells, can be another potential experiment that may provide a deep level of biomolecular alterations in the biochemistry of retinal neurons.

179

<div align="center">

**Curriculum Vitae**

**Ebrahim Aboualizadeh**

</div>

**Education**

**Spring 2012–August 2017:** Physics Ph.D., University of Wisconsin–Milwaukee

**Advisor:** Prof. Carol J. Hirschmugl

**Dissertation**: Biomedical applications of mid-infrared spectroscopic imaging and multivariate data analysis: contribution to the understanding of diabetes pathogenesis

**2007–2009:** M.S. Physics, Quantum Field Theory, Razi University, Kermanshah, Iran

**Advisor:** Prof. Mohammad Vahid Takook

**Thesis Title:** Revisiting the conformal invariance of the scalar field from Minkowski space to de Sitter space

**2003–2007**: B.S. Physics, Solid State Physics, Shahid Chamran University, Ahwaz, Iran

**Qualification Highlights**

- Experienced in mid-infrared spectrochemical imaging, and 3D imaging with IR spectro-microtomography
- Expert in optical diagnosis, mechanism of disease, pattern recognition, spectroscopy and microscopy on various biological tissues and cells
- Develops machine learning algorithms for multivariate data analysis
- Expert in chemometric tools
- Skilled in sectioning biological samples using cryostat machine (e.g., eye, kidney, adipose tissues)
- Strong record of publications and conference presentations
- Experienced in mentoring junior research staff and lab mates
- Thorough knowledge of principles and practices of spectroscopy and imaging
- Experience of working at the IRENI beamline (Synchrotron Radiation Center) in Madison, WI
- Works well both independently and in collaborative settings
- Committed to achieving goals and objectives
- Exhibits strong attention to detail and organizational skills
- Flexible and quickly adapts to changing circumstances and priorities
- Maintains high ethical standards

- Competently handles documents, public complaints, conflict resolution, and decision-making
- Strong oral and written communication skills
- Skilled negotiator that leverages strong interpersonal and analytical skills

**Awards and Distinctions**

**2017**    Winner of the **TOMAS A. HIRSCHFELD AWARD** sponsored by the Federation of Analytical Chemistry & Spectroscopy Societies (FACSS) for the most inventive research. SCIX 2017, Reno, NV. This competitive award is given to the most outstanding abstract submitted to the conference.

**2016**    Winner of the **Best Poster Presentation Award** sponsored by the Society for Applied spectroscopy (SAS), SCIX 2016, Minneapolis, MN.

**2016**    Department of Physics **Research Excellence Award** for distinction in research among all graduate students in Physics at the University of Wisconsin-Milwaukee.

**2016**    Selected for the **Distinguished Dissertation Fellowship (DSF)** program among all graduate students at the University of Wisconsin–Milwaukee **(15 students out of 4475 Graduate students are selected)**.

**2015**    Selected for the **Distinguished Graduate Student Fellowship** (**DGSF**) program among all graduate students at the University of Wisconsin–Milwaukee **(Less than 1% of the students are selected)**.

**2015**    **Physics Research Excellence Award** recipient, University of Wisconsin–Milwaukee.

**2014**    Recipient of the **David Lichtman Scholarship for "outstanding performance in experimental physics"**, University of Wisconsin–Milwaukee. This award is given to one student each year.

**2013**    Winner of the **Best Poster Presentation Award** sponsored by the NIH/NIBIB/NCBI grant as part of the "X-Ray Fluorescence Microscopy in Biology" workshop (August 2013), Midwest microscopy and microanalysis society, Chicago, IL.

**2013**    Winner of the **Travel Award** sponsored by "Midwest microscopy and microanalysis society", (August 2013), Chicago, IL.

**2012**    **Chancellors Graduate Student Award,** Physics Department, University of Wisconsin–Milwaukee. This award is given to one student each year.

**2010**    **Elite University Student Award** selected by Iran National Elites Foundation, Tehran, Iran.

**2009**    **Distinguished Student Award** for the highest GPA in master's program (October 2009), Kermanshah, Iran.

**Peer-Reviewed Journal Publications**

**E. Aboualizadeh**, G. Azarfar, M. Unger, M. Giordano, C.J. Hirschmugl, "In vivo time-resolved FTIR imaging to determine the carbon fixation across a *Thalassiosira weissflogii* cell," in preparation (2017).

**E. Aboualizadeh**, V.V. Bumah, D.S. Masson-Meyers, J.T. Eells, C.J. Hirschmugl, C.S. Enwemeka, "Infrared microspectroscopy study: antimicrobial activity of selected disinfectants against methicillin-resistant Staphylococcus aureus (MRSA)", under review in PLOS ONE (2017).

**E. Aboualizadeh**, O.T. Carmichael, P. He, D.C. Albarado, C.D. Morrison and C.J. Hirschmugl, "Characterizing rodent adipose tissue activation level with infrared microspectroscopy, *Frontiers in Endocrinology*, 8, 121 (2017).

**E. Aboualizadeh**, M. Ranji, C.M. Sorenson, R. Sepehr, N. Sheibani, C.J. Hirschmugl, "Retinal oxidative stress at the onset of diabetes determined by synchrotron FTIR widefield imaging: Towards diabetes pathogenesis", *Analyst*, 142, 1061-1072 (2017). **(This paper is the front cover of Analyst)**.

V.V. Bumah, **E. Aboualizadeh**★, D.S. Masson-Meyers, J. Eells, C.S. Enwemeka, and C.J. Hirschmugl, "Spectrally resolved infrared microscopy and chemometric tools to reveal the interaction between blue light (470nm) and methicillin-resistant Staphylococcus aureus" *Journal of Photochemistry and Photobiology, B: Biology, 167, 150-157* (2017). ★**(Joint-First author-Contributed equally to this work)**.

**E. Aboualizadeh**, E.C. Mattson, C.L. O'Hara, A.K. Smith, C.L. Stucky, and C.J. Hirschmugl, "Cold Shock Induces Apoptosis of Dorsal Root Ganglion Neurons Plated on Infrared Windows," 140, *Analyst* 4046–4056 (2015).

M.E. Barabas, E.C. Mattson, **E. Aboualizadeh**, C.J. Hirschmugl, and C.L. Stucky, "Chemical Structure and Morphology of Dorsal Root Ganglion Neurons from Naïve and Inflamed Mice", *Journal of Biological Chemistry*, 289(49): 34241-9 (2014).

E. Mattson, M. Unger, J. Sedlmair, M.J. Nasse, **E. Aboualizadeh**, Z. Alavi, and C. Hirschmugl, "Widefield FT-IR 2D and 3D Imaging at the Microscale Using Synchrotron Radiation" (book chapter); in **"***Infrared and Raman Spectroscopic Imaging***"**, edited by R. Salzer and W.S. Heinz; pp. 585–618, *Wiley-VCH Verlag GmbH & Co. KGaA*, 10.1002/9783527678136 (2014).

E.C. Mattson, **E. Aboualizadeh**, M.E. Barabas, C.L. Stucky and C.J. Hirschmugl, "Opportunities for Live Cell FT-Infrared Imaging: Macromolecule Identification with 2D and 3D Localization," *Int. J. Mol. Sci.* 14, 22753–22781 (2013).

S. Moradi and **E. Aboualizadeh**, "Hydrogen atom and its energy level shifts in de Sitter universe", *General Relativity and Gravitation*, 42, 2, 435–42 (2009).

## Conference Presentations

Invited talk: **E. Aboualizadeh** "temporal diabetes-mediated biochemical alteration in the mouse retina", Center for vision research, (June 2017), Institute of Optics, University of Rochester, NY.

Invited talk: **E. Aboualizadeh** "Oxidative stress in diabetic retinopathy: Imaging reveals histology", McPherson Eye Research institute, (May 2017), University of Wisconsin-Madison, WI.

Invited talk: **E. Aboualizadeh** "Label-free Fourier transform infrared hyperspectral imaging of biological tissues and cells", Beckman Institute, UIUC, (May 2017), Urbana-Champagne, IL.

**E. Aboualizadeh**, O.T. Carmichael, P. He, D.C. Albarado, C.D. Morrison and C.J. Hirschmugl, "Characterizing brown and subcutaneous white adipose tissue activity level with Fourier Transform Infrared (FTIR) Imaging", Obesity week, (October 2016), New Orleans, LA (Oral presentation).

**E. Aboualizadeh**, V.V. Bumah, D.S. Masson-Meyers, J. Eells, C.S. Enwemeka, and C.J. Hirschmugl, "The potential of FTIR spectroscopy and computational analysis in characterizing the mechanism of action of blue-light against Methicillin-resistant Staphylococcus aureus", The great SCIentific eXchange (SCIX) (September 2016), Minneapolis, MN (Poster presentation).

C.J. Hirschmugl**, E. Aboualizadeh**, "Characterizing treated methicillin-resistant Staphylococcus aureus using infrared spectromicroscopy", SPEC meeting, (June 2016), Montreal, CA (Oral presentation).

**E. Aboualizadeh**, C.M. Sorenson, R. Sepehr, M. Ranji, N. Sheibani, C.J. Hirschmugl "Synchrotron widefield FTIR imaging of diabetic retina tissue", 8th International Workshop on Infrared Microscopy and Spectroscopy using Accelerator Based Sources (October 2015), Brookhaven National Lab, Long Island, NY (Oral presentation).

**E. Aboualizadeh**, C.M. Sorenson, R. Sepehr, M. Ranji, N. Sheibani, C.J. Hirschmugl, "Multivariate analysis as a tool to extract characteristic bands associated with diabetic retina tissue using synchrotron infrared spectromicroscopy," annual meeting of the Federation of Analytical Chemistry and Spectroscopy, The great SCIentific eXchange (SCIX) (September 2015), Providence, RI (Oral presentation).

**Ebrahim Aboualizadeh**, C.M. Sorenson, R. Sepehr, M. Ranji, N. Sheibani, and C.J. Hirschmugl, "Detection of Biomarkers for Diabetes from Retina Tissue Using FTIR Chemical Imaging," *International Gordon Research Conferences on Vibrational Spectroscopy*, (August

2014), University of New England, Biddeford, ME (Poster presentation).

**E. Aboualizadeh**, M. Unger, M.J. Nasse, S. Ratti, C. Olivieri, M. Giordano, and C.J. Hirschmugl, "Time-resolved infrared microspectroscopy used as a tool to understand biochemical changes in *Thalassiosira weissflogii* cell", Synchrotron Radiation Center Meeting (September 2013), Stoughton, WI (Poster presentation).

**E. Aboualizadeh**, M. Unger, M.J. Nasse, S. Ratti, C. Olivieri, M. Giordano, and C.J. Hirschmugl "The Application of FTIR Spectromicroscopy to the study of Carbon Fixation over time across a *Thalassiosira weissflogii* cell", X-Ray Fluorescence Microscopy in Biology Workshop, Northwestern University (August 2013), Chicago, IL (Oral presentation).

**E. Aboualizadeh**, M. Unger, M.J. Nasse, S. Ratti, C. Olivieri, M. Giordano, and C.J. Hirschmugl "Fourier Transform Infrared Spectrochemical Imaging for Algal Cells in Aqueous Environment", Synchrotron Radiation Center Meeting (September 2012), Stoughton, WI (Poster presentation).

### Scholarly Peer-Review

Invited to review several journal articles in "**Analytical Methods**" (Royal Society of Chemistry).

### Professional Experience and Memberships

**Infrared Beamline (IRENI) Member of Staff**, Synchrotron Radiation Center, Madison, WI (2012–2014)

**Cryo-microtome Expert**, Biotechnology facility, Biological Sciences, University of Wisconsin–Milwaukee (2013–2016)

**Member** of the Society for applied spectroscopy

**Member** of the American Association for the Advancement of Science (AAAS)

**Member** of the International Society for Clinical Spectroscopy

### Teaching Experiences

**University of Wisconsin–Milwaukee**: **Jan. 2012 – May 2012:** Physics I (Calculus treatment)

**University of Wisconsin–Milwaukee**: **Jan. 2012 – May 2012:** Physics II (Calculus treatment)

**Razi University: Jan. 2008 – May 2008:** Undergraduate Quantum Mechanics

**Razi University: June 2008 – Aug. 2008:** General Physics Lab

### Software Skills

- R, Matlab, Igor Pro, OPUS, SAS, Stat Plus, Mathematica, Maple, Basic Knowledge of Python, Microsoft office

- Expert in Principal Component Analysis (PCA), Hierarchical Clustering Analysis (HCA), Linear Discriminant Analysis (LDA), Machine Learning algorithms, Regression models and Bio-statistical analysis
- Comfortable with Linux, Mac, and Windows